TABLE OF CONTENTS

LIST OF TABLES

LIST OF FIGURES

Page

LIST OF ABREVIATIONS

AV	Accelerating voltage
BC	Beam current
BF	Beam focus
BM	Base metal
BOP	Bead-on-plate
CCD	Charge-coupled device
DBTT	Ductile-to-brittle transition temperature
DIC	Digital image correlation
EB	Electron beam
%El.	Total percent elongation
EBW	Electron beam welding
EBZHT	Electron beam zonal heat treatment
EDM	Electro-discharge machining
EDS	Energy dispersive spectroscopy
FCAW	Flux-cored arc welding
FE	Finite element
fps	Frames per second
FZ	Fusion zone
G	Gage length
GMAW	Gas metal arc welding
GTAW	Gas tungsten arc welding
h	Hours
HAZ	Heat affected zone
HLAW	Hybrid-laser arc welding
LSM	Laser scanning microscope
OM	Optical microscope
PMZ	Partial melted zone
PWHT	Post-weld heat treatment
s	Seconds

S	Welding speed
SEI	Secondary electron imaging
SEM	Scanning electron microscopy
SMSS	Supermartensitic stainless steel
T	Temperature
TTT	Time-temperature-transformations
UTS	Ultimate tensile strength
XRD	X-ray diffraction
YS	Yield strength
ZHT	Zonal heat treatment
2D	Two-dimensional
3D	Three-dimensional

LIST OF SYMBOLS AND UNITS OF MEASUREMENTS

Symbol	Unit	Description
a_b	-	Beam active parameter
Ac_1	°C	Start temperature of austenite formation on heating
Ac_3	°C	Finish temperature of austenite formation on heating
Ac_4	°C	Start temperature of delta ferrite formation on heating
Ac_5	°C	Finish temperature of delta ferrite formation on heating
D	m	Beam diameter
D_o	m	Object distance
D_F	m	Focal length
HV	Vickers	Hardness
K	mm^2/s	Thermal diffusivity
k	W/(mK)	Thermal conductivity
M_S	°C	Martensite start temperature
M_f	°C	Martensite finish temperature
T_m	°C	Melting point
t	m	Thickness
TTT	-	Time-temperature-transformations
α	-	Alpha-ferrite
δ	-	Delta-ferrite
γ	-	Austenite

INTRODUCTION

Hydropower is a source of renewable energy that currently represents the 16% global electricity generation by the end of 2008 (Kumar, 2011). Although hydropower is an established technology for electricity generation, research and development is required for improving industrial knowledge, environmental performance and reducing the operational costs. To answer to the necessity of research and development in electricity generation, the CREFARRE (Consortium de recherche en fabrication et réparation des roues d'eau) program was conceived in January 2011. Two universities (École de technologie supérieure and École Polytechnique de Montréal), two research centers (IREQ – Institut de recherche d'Hydro-Québec and NRC-CNRC–National Research Council of Canada) as well as two industrial leaders (Hydro-Québec and Alstom) were involved in this project. This dissertation is a part of the larger program on manufacturing and repair of turbine runners (Hydro-Québec, 2011). The priority in this research and development is improving technologies for the design, manufacturing and demonstration of next generation cost-effective turbines runners, the core element of the hydropower system, which is engineered to operate for decades in a hydro-abrasive environment (erosion, corrosion, cavitation).

Considering the geometric dimensions of Francis turbines runner in hydropower system, the main challenges in turbine manufacturing are shaping and assembly of components. As each Francis turbine is made of different parts with different geometries and curvatures, a reliable joining process for their assembly is required. The different components of the present day turbines including blades, band and crown, as shown in Figure 1-1a-d, are assembled together by T-joint geometry with a conventional joining processes such as gas tungsten arc welding (GTAW) or techniques with solid wires or flux-cored wires. The inherent and intensified stresses of the joint areas of the circular-shaped transition between the blades and the band or crown of the Francis turbine runner, cause high stresses concentrations and are thus the most critical locations for initiating cracks at any weld defect that may be present. Therefore, development and replacement of conventional welding processes with advanced welding processes to manufacture sound joints is vital for having a reliable runner.
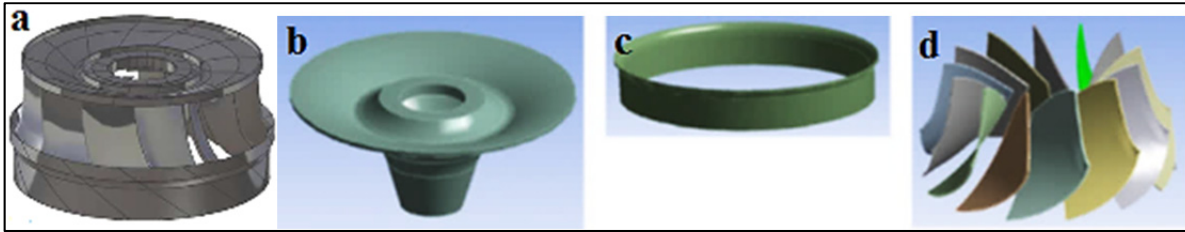
Figure 1-1 (a) Francis turbine runner (Boudreault et al., 2014) and components (b) crown, (c) band, and (d) blades, respectively from left to right (Saeed, Galybin et Popov, 2010)

Up to now, the application of a high energy density joining technology, electron beam welding (EBW), was not considered for the assembly of Francis turbine runners due to the site welding requirements and size-related complexities of the parts to be assembled or repaired. However, with the recent advancements in high energy density joining technologies in combination with advanced computer aided design, the manufacturing requirements for the assembly of hydropower turbine elements may be addressable through weldability research and development. Moreover, utilizing EBW without filler addition and joint gap preparation can result in less inhomogeneity in the mechanical and microstructural properties in the electron beam (EB) weld due to the single pass process, whilst saving raw materials, production time, energy and costs.

Deliberating on the hydro-abrasive conditions (head or vertical drop, flow rate, sand/silt content) of hydropower turbines, materials used for this application must have long-term fatigue life performance as well as good wear and corrosion resistance. Thus, cast or wrought forms of martensitic stainless steels containing 13%Cr-4%Ni are the typical materials selected for the manufacture of Francis turbine runners due to a combination of characteristics (e.g. relatively high strength, corrosion resistance, good weldability) that overall render a superior performance of the assembly over a prolonged life.

In this manuscript-based thesis, a pioneer research for the feasibility of autogenous EBW (no filler addition) for joining thick gage section (up to 90 mm) of two martensitic stainless steels, CA6NM (cast) and UNS S41500 (wrought), containing 13%Cr-4%Ni, with only a single pass without filler metal addition has been studied. The evaluation of the

microstructure, microhardness, tensile properties and residual stresses of the EB welded martensitic stainless steels at the fusion zone (FZ) and heat affected zones (HAZs) were addressed in both as-welded and post-weld heat treated (PWHTed) conditions. In addition, a procedure for electron beam zonal heat treatment (EBZHT) was successfully developed and demonstrated for the first time with a defocused beam for preheating martensitic stainless steels inside the vacuum chamber. Another state-of-the-art procedure was using digital image correlation (DIC) system to characterize the local tensile properties in the FZ and HAZs and distortion measurement in the thick gage sections of martensitic stainless steels welded by EBW. In addition, for the first time, the longitudinal residual stresses in 90 mm thick EB welded martensitic stainless steels were measured by the contour method.

Specifically, in Chapter 1, a description of the challenges and objectives are given to provide a context to the present research work. Then in Chapter 2, a literature survey was conducted to review the state-of-the-art knowledge on martensitic and supermartensitic stainless steels, their joining processes and procedures, DIC systems for characterizing the mechanical properties and distortion, and the contour method for determining the residual stresses with an emphasis on EBW of thick gage sections. In Chapter 3, published in the International Journal of Advanced Manufacturing Technology, 2015, vol. 78, no 9-12, p. 1523-1535, the feasibility of EBW 60 mm thick CA6NM with a single pass without filler metal addition and using an EBZHT for preheating was validated. In addition, a detailed characterization of the microstructure and microhardness in different distinct regions of the EB weld in both the as-welded and PWHTed conditions were reported. In Chapter 4, submitted to the journal of Materials Science and Engineering A, in August 2015, the feasibility of EBW 88 mm thick UNS S41500 martensitic stainless steel welded without preheating was ascertained. The global and local mechanical properties, including microhardness and tensile properties (by using DIC) in the different regions of the weldment, were explained. In Chapter 5 accepted for publication in the journal of Science and Technology of Welding and Joining, in December 2015, the distortion and longitudinal residual stresses in 90 mm thick gage sections of UNS S41500 and CA6NM materials assembled by EBW were evaluated in the as-welded and/or PWHTed conditions. Finally, the

conclusions, recommendations for future work and a section on the statement of originality and contributions to knowledge are provided.

CHAPITRE 1

CHALLENGES AND OBJECTIVES

The main challenges in hydroelectric turbine manufacturing considering the size and geometry of components are the forming and welding processes required for production. Specifically, each hydroelectric turbine has a runner that is the heart of the turbine and is made of many parts with various geometries and shapes. Therefore a reliable joining process for their assembly is required, especially considering that the joint area comprises high stresses and is the most critical location for initiating cracks. Presently, the different turbine runner components continue to be assembled and repaired by conventional joining processes. Considering the size and thickness of the components, assembly via conventional arc welding processes such as flux-cored arc welding (FCAW) process requires multiple passes to fill the joint gap. The application of a multi-pass process imparts a high heat input that leads to high residual stresses and distortions, microstructural inhomogeneity and performance variability across the weldment. By contrast, EBW, as a high-energy density welding process, can join a thick gage section using a single pass without filler addition or groove-machining. In spite of being an advanced process, EBW has several challenges for joining thick gauge sections of martensitic stainless steel grades employed for hydroelectric turbine manufacture, such as (1) large temperature gradients, (2) high cooling rates, (3) pre-existing defects and cracking susceptibility of the base material, (4) pre-weld preparation and clamping and (5) gap tolerance between the abutting interfaces.

The purpose of this project was thus to develop an automated/advanced assembly method, as an alternative to conventional arc welding for hydraulic runner manufacturing, by (1) improving and extending the existing knowledge on EBW of thick gage sections, (2) investigating the weldability of two important hydroelectric turbine materials CA6NM and UNS S41500 that are low carbon martensitic stainless steels grades, (3) studying the process parameters, weld integrity and penetration depth, (4) understanding the different phase constituents of the microstructures in the different regions of the EB weldments, (5) relating the evolution in the mechanical properties across the weldment to the local microstructural

features and (6) quantifying the distortion and resulting residual stress. Through this feasibility study, the next generation of engineers can become familiar with the potential of a single pass electron beam welding process for assembly of hydroelectric turbine materials and understand the related design for manufacturing criteria for industrial application.

Thus, in this project, process development with EBW was studied for joining thick sections of UNS S41500 (wrought grade) and CA6NM (cast grade), two martensitic stainless steels that have a similar nominal composition of 13%Cr and 4%Ni. The weldabilities of UNS S41500 and CA6NM were studied by varying the process parameters such as the power, beam focal position, welding speed, gap size, preheating temperature, and PWHT. The resulting weld bead geometry, weld integrity (voids, cracking, penetration depth), phase constituents in the FZ and HAZs, and microhardness were characterized using different techniques, including optical microscope (OM), laser scanning microscope (LSM), scanning electron microscope (SEM), x-ray diffraction (XRD) and microindentation hardness testing. The global and local tensile mechanical properties of the welds were measured through uniaxial tensile testing using DIC. In addition, an automated optical measuring system was used to determine the angular distortion of the welded assemblies. The longitudinal residual stress distribution was also determined by the contour method. In general, the design of experiments for welding (including preheating and PWHT) as well as characterization of the weldments was performed according to recommended guidelines stipulated in various standards such as ASTM-E8, ASME Section VIII & IX.

CHAPITRE 2

LITERATURE REVIEW

This Chapter provides a brief description of the EBW process including principles, mechanism and parameters of EBW. The next section describes martensitic stainless steels namely 13%Cr- 4%Ni, which are widely used in the hydropower turbine runners and using DIC method to measure the tensile properties. Then, work related to welding-induced distortion is considered. Finally, research related to analysis of the residual stresses during welding measured by the contour method is described.

2.1   Electron beam welding (EBW)

2.1.1   Principles of EBW

EBW is a mature manufacturing technology that has a demonstrated capability of joining thick gauge section materials in a single pass with considerably lower heat input than conventional arc welding processes. The weldment is typified by a high depth to width ratio, narrow FZ and HAZ, low residual stresses and distortion, and high mechanical performance (Meleka, 1971). The schematic of different geometries of a butt joint in different arc welding processes is compared with EBW in Figure 2-1. The EBW is a fusion welding process for joining a broad range of similar and dissimilar materials (Sun et Karppi, 1996) by bombardment of the material surface with high energy electrons. Electrons emitted from a filament or a cathode (usually tungsten) with a low current (e.g. 50–1000 mA), which is attached to a high voltage supply (30–150 kV), are accelerated and focused on the work piece (Meleka, 1971; Pitrou, 1975).
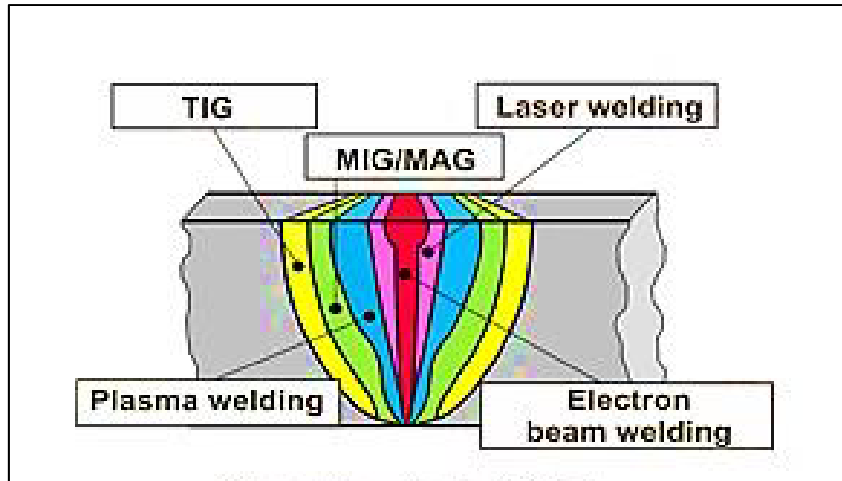
Figure 2-1 Schematic of butt joint geometry in different arc
welding processes (Pilarczyk et Węglowski, 2014)

The combination of a filament or an anode, and a bias cup is called the EB gun that is a main part of the EBW system as shown schematically in Figure 2-2 (Handbook, 2004; Mladenov et al., 1998). Due to scattering of the electrons at atmospheric environment, the EBW is usually carried out in a vacuum chamber under pressure of 10^{-5} torr for deep penetration in thick gage sections, however it is possible to use the EBW in medium vacuum (Dugdale, 1975) or non-vacuum systems (Radtke, 1964) when less penetration depth is desired. The application of EBW in a vacuum environment prevents contamination of the molten weld pool from atmospheric elements, as well minimizes diffusion/divergence of the focused EB from scattering and ionisation under atmospheric pressure. In comparison, non-vacuum EBW utilizes essentially similar equipment but beam delivery must be guided from the vacuum environment of the beam generator through a series of separately pumped pressure stages and a plasma window/shield. This then allows projection of the beam onto the work-piece under atmospheric conditions without generating appreciable pressure leakage into the EB generator. However, though the concerns related to the work-piece size are mitigated with the employment of a non-vacuum EBW system, these must be weighed against processing shortfalls such as lower penetration depth and shielding gas protection of the molten weld pool. Hence, once the viability of high energy density welding for hydropower turbine materials is ascertained through an understanding of the influence of the processing conditions on the weld performance, the EB system requirements (e.g. power, and

welding speed) can be reliably configured with concurrent considerations of workplace health and safety (e.g. radiation and fumes for non-vacuum conditions) (Handbook, 1993; Meleka, 1971; Schultz, 1993). For understanding the effect of different parameters of the EBW for joining thick gage section, the mechanism of EBW shall be explained first.
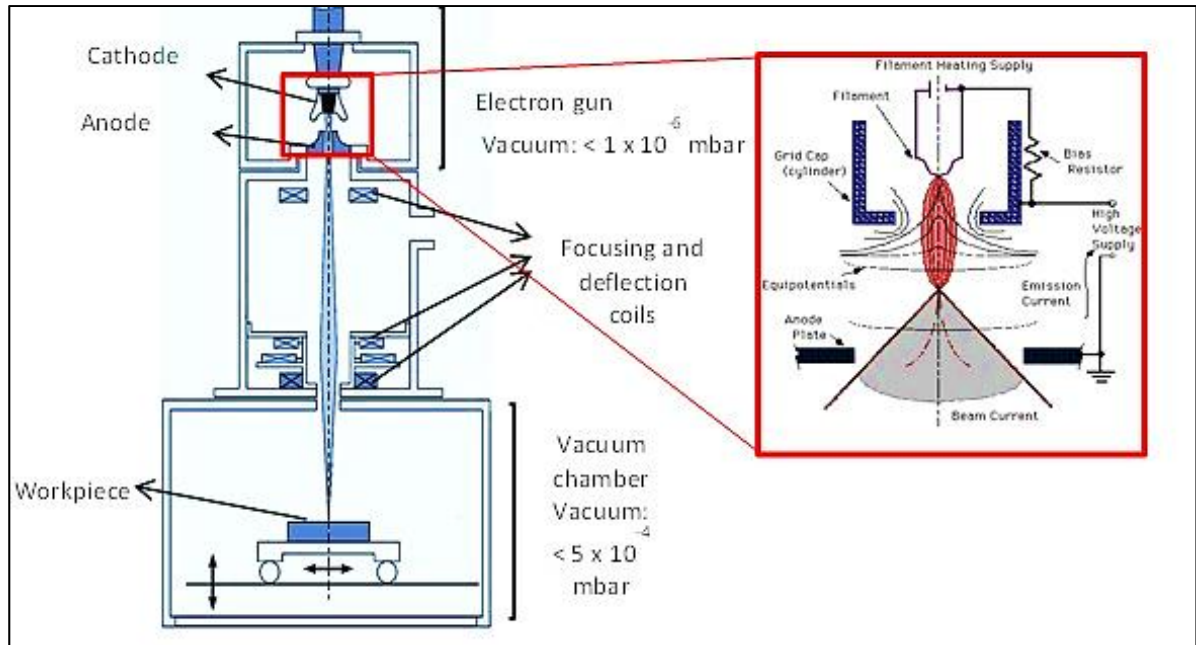
Figure 2-2 Schematic of EBW and its gun (Handbook, 1993)

2.1.2   Deep penetration welding by EBW

EBW is usually used for penetrating thick sections of material and the magnitude of penetration is usually hundreds times more than the penetration of the electron. For instance, electron penetration in solid metal at 150 kV is only 0.06 mm. Therefore, by using a defocused beam, mitigated current and low power density, deep penetration is not possible. To have a deep penetration weld, high power density is required in order to rapidly convert the kinetic energy of the electron to the heat at the impingement location of the EB. After impingement of the EB, the metal surface is melted without considerable conduction of the heat to neighboring regions. By additional heating, the metal vaporizes and the metal vapors release upwards. The reaction forces of the vapor push the molten metal downwards. This process from the EB impingement at metal surface to pushing the molten metal downwards

continues up to complete formation of the keyhole. The schematic of the different steps during EBW in order to have deep penetration is shown in Figure 2-3. To fully penetrate through the complete thickness of the joint, the power density must be high enough to form the keyhole through the entire thickness. Thus, the mechanism of deep penetration in EBW is formation of the keyhole including vapors and molten metal (Schultz, 1993).
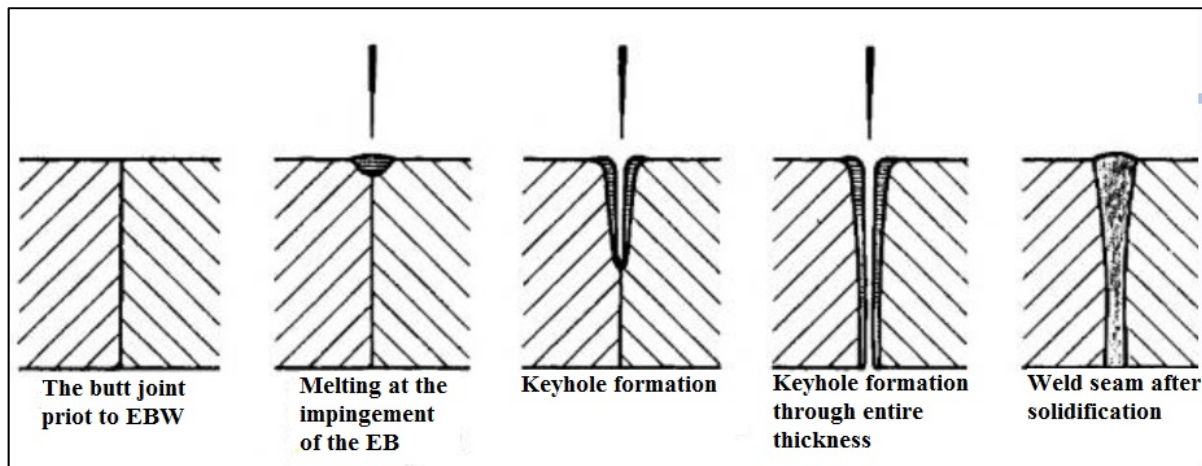
Figure 2-3 Different steps of EB deep penetration (Schultz, 1993)

In order for the keyhole to stay open and let the weld pool flow through the joint, various forces act together including surface tension and vapour pressure (Metzbower, 1993). The effect of the forces and their interaction is a physical process that is explained briefly here. At first, vapours exist at the center of the keyhole; then, if the pressure of the vapour is high enough, the keyhole goes through the material (Lee et al., 2002; Metzbower, 1993; Petrov et al., 1998). The surface tension force is responsible for keeping the keyhole opened and closed which is dependent on the thickness of material and the keyhole diameter. If the thickness of the material is greater than the keyhole diameter, the surface tension will act inwards thus closing the hole. The vapor pressure acts opposite to the surface tension force and goes upwards and towards the wall of the keyhole. When all forces in the keyhole reach stability, the keyhole is closed and the joint is made. In spite of the importance of these forces on the weld soundness, the welding parameters also have a fundamental role for the weld quality and performance as described below (Meleka, 1971).

2.1.3   Electron beam welding parameters

Weld quality, penetration depth and FZ shapes of the EB weld depends on the combination of EB parameters including (1) accelerating voltage (AV), (2) beam current (BC), (3) welding speed (WS), (4) beam focal position (BF), and (5) beam deflection. Besides the aforementioned EBW parameters, there are other parameters including environment of the EBW, and material properties such as thermal conductivity and melting point which can change the penetration depth (Hablanian, 1963); but in this section the emphasis will be on the five main EBW parameters.

Originally, the voltage of accelerated electrons has the main effect on the power density. As the maximum accelerating voltage for low voltage EBW systems are 60 kV and relatively low for thick penetration, thus to achieve the required power, usually this parameter is kept at the maximum and the desired power density is compensated by changing the beam current that is easy to control. Generally, for a given beam current with increasing the accelerating voltage, and for a given accelerating voltage, by increasing the beam current, the penetration depth will increase (Handbook, 1993; Meleka, 1971; Schultz, 1993).

The other main parameter in EBW is welding speed or travel speed which determines the heating and cooling rates as well as FZ shape, weld quality and penetration depth. For a given beam current and accelerating voltage, a higher welding speed forms narrower weld bead and lower penetration depth (Hemmer, 1999; Mladenov et al., 1998). The other effective parameter on the penetration depth and weld quality is the focus current that determines the focus distance or focal point of the electrons by applying current through the coils which generate the magnetic fields. By changing the focus current, the focal position can be above the surface (overfocusing), inside the part (sharp focus) or below the bottom surface (underfocusing). Among these different focus current conditions, the sharp focus whereby the focal point is inside the weldment will form a narrow and parallel-sided weld. There are many researches about the effect of the beam focus on the EBW characteristics including Elmer, Giedt (Elmer et al, 1990; Giedt et Tallerico, 1988) and Ho (Ho, 2005). Firstly, Adams (Adams, 1968) found that by varying the beam focus location, the depth of penetration changed. He showed that with an accelerating voltage of 130 kV, a beam current

of 10 mA, a welding speed of 25.4 mm.s^{-1} and a working distance of 152.4 mm, the maximum depth of penetration was obtained with a beam focus position of 25.4 mm under the top surface of the workpiece.

Afterwards, Konkol (Konkol et al., 1971) showed that the deepest penetration in a 50 mm thick HY-130 EB weld can be achieved in a sharp focus condition where the beam focal position is inside the workpiece or by decreasing the work distance. In their experiments, the working distance, accelerating voltage, beam current, and travel speed of 152.4 mm, 150 kV, 100 mA, and 10.58 mm.s^{-1} respectively were used. With the mentioned parameters, the deepest penetration was obtained at a focal location of 38.1 mm below the plate surface.

Kohyama (Kohyama et al., 1984) studied EBW of pure Ti, Ti-6Al-4V, stainless steel grade 304 and Al with a maximum plate thickness up to 56 mm using a 100 KW EBW facility. They investigated the effect of different parameters including beam focus and welding speed on the penetration depth in bead-on-plate (BOP) and two passes butt welds. For easier understanding of the effect of beam focus on penetration depth, Arata (Arata et al., 1973) defined a beam active parameter, a_b, which is calculated by the "object distance"/ "focal length" as illustrated in Figure 2-4a. The a_b values were chosen from 0.7 to 1.2 by changing the beam focus position from overfocusing to underfocusing as shown in Figure 2-4b. The results showed that the maximum penetration occurred with the a_b value about 0.9 for all materials used. In their study indicated that at a low welding speed, the keyhole becomes unstable and generates lower penetration depth, more spatter, undercut and spiking (Kohyama et al., 1984). In 2007, Chi (Chi et al., 2007) successfully welded 11 mm thick plates of AZ31B-F with EBW by adjusting the variable parameters of EBW including beam current, accelerating voltage, welding speed, and beam focus position (Chi et al., 2007).

In addition to different focusing conditions, defocused beam will increase the beam diameter and reduce the power density (Meleka, 1971). The defocusing beam is achievable by passing current through the coils of deflection system inside the electron column, as shown in Figure 2-2. By periodically varying the current of the deflection coils, the EB can oscillate with a desired shape and frequency. The EB oscillation can control the shape of the the FZ and keyhole, the closing of the keyhole and also porosity formation in FZ (Schultz,

1993). Recently, oscillation and defocused beam were utilized for zonal heat treatment (ZHT) such as preheat (Sarafan et al., 2015) and post-weld heat treatment (Chen et al., 2002) of the weldment inside the vacuum chamber of the EBW system. The beam in ZHT is rasterized several times with a given speed over the entire workpiece until sufficient heat is created inside the part. Melting of the workpiece surface does not occur since the intensity of the beam is reduced by defocusing during ZHT. The setting of the correct ZHT (preheat or PWHT) temperature is guaranteed by the application of thermocouples. ZHT has been effectively used for improving the microstructure and properties of the EB welded joints of steel (Chen et al., 2002; Hu et Liu, 2009).
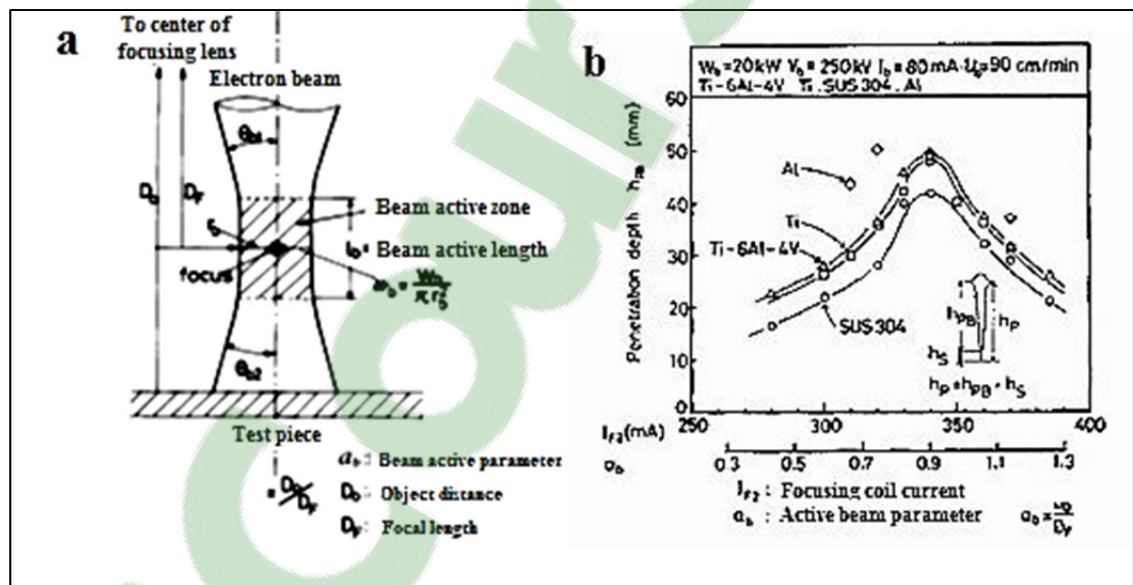
Figure 2-4 (a) Definition of beam active parameter (Arata, 1973), (b) effect of beam focusing on the penetration (Kohyama et al., 1984)

Researchers who worked on ZHT noted that the scanning velocity of beam in ZHT played an important role on the weld properties and residual stresses. In 2009 (Hu et Liu, 2009), ZHT was applied for a 14.5 mm thick TC4 alloy plates and the effects of the ZHT on the residual stresses, microstructures and mechanical properties of the EB welded joints was investigated. A few experiments on ZHT have been conducted in situ in the EBW chamber; and to the best knowledge of the author, there is no published study of ZHT in martensitic stainless steels used in this study. Therefore, applying ZHT for martensitic stainless steel

14

which is a material of interest in hydroelectric turbine industries seems to be a vital and necessary innovation in turbine industries. Hydroelectric turbine materials usually are made of thick gage sections and EBW can be a good alternative to join those thick sections with a single pass without filler addition. The application of the EBW for thick gage sections is summarized in the next part in spite of having the limited literatures on thick gage sections about 50 mm.

2.1.4 Electron beam welding of thick section metals

EBW has been broadly used for joining different alloys, eg. a 17 mm thick Ti6Al4V with filler addition (Barreda et al., 2001), a 17.5 mm thick Ti6Al4V (Saresh et al., 2007), materials with different thicknesses from 6 to 30 mm of Mg-Al alloys (Su et al., 2002), a 10 mm thick IN706 (Ferro et al., 2005), 30 and 50 mm thick Mg-based alloys (Wu et al., 2004), a 19 mm thick 17-4 PH stainless steel (Wanjara et Jahazi, 2008), a 6 mm thick of dissimilar austenitic stainless steel (AISI 304) and low alloy steel (AISI 4140) (Arivazhagan et al., 2011). Among them, Srinivasan in 2004 (Srinivasan et al., 2004) studied a 20 mm thick supermartensitic stainless steel (SMSS) using one pass EBW process with two GTA cosmetic capping passes on both the face and root sides with matching filler addition, as shown in Figure 2-5. They evaluated the hydrogen assisted stress cracking behaviour, microstructure and microhardness of the joint. The SMSS used in this study had a chemical composition (wt. %) of 11.65% Cr, 6.49% Ni, 1.87% Mn, 0.006% C, 2.33% Mo, 0.294% Si, 0.475% Cu, 0.009% N. Generally, the properties and performance of welded martensitic stainless steels are affected by the chemical composition. Among different steels in this group, the low carbon martensitic stainless steels have been widely applied in turbine runners manufacturing. Thus, the following includes a critical review about low carbon martensitic stainless steels as the target material for hydroelectric turbine and the effect of each element on the phase constituents and microstructures.
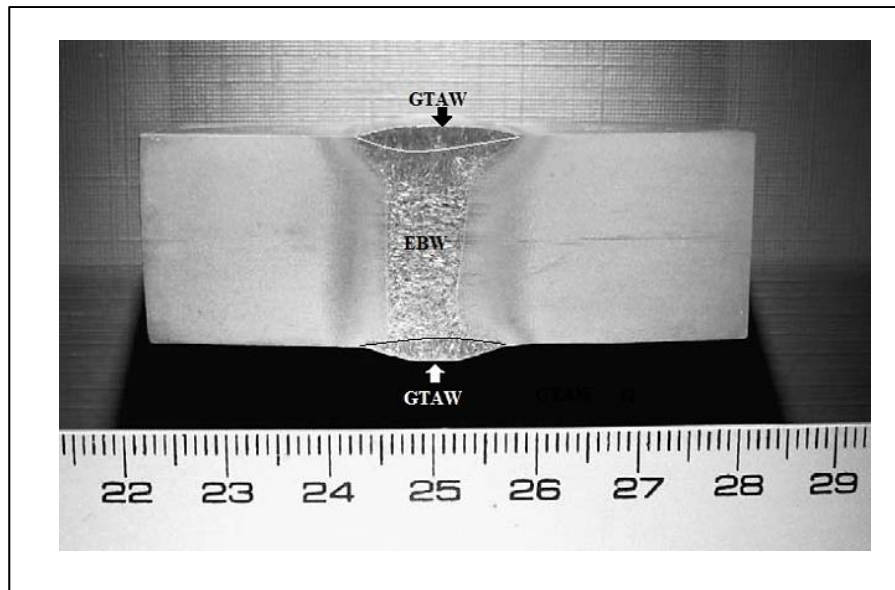
Figure 2-5 The macro section of the EB weldment
(scale in cm) (Srinivasan, Sharkawy et Dietzel, 2004)

2.2   Low carbon martensitic stainless steels

The 13%Cr-4%Ni steels belong to the group of "low carbon martensitic stainless steels". These martensitic stainless steels, based on the Fe-C-Cr ternary system, undergo a transformation that readily forms martensite from the austenite phase. Hence, even under the relatively slow cooling rates, the FZ is predominately martensite. Adding carbon to these martensitic stainless steels cause hardening and strengthening and also increase the susceptibility to hydrogen induced cracking or cold cracking. Therefore, having a balance between hardening and crack susceptibility requires control of carbon content. For this purpose, a level of carbon content below 0.06 wt.% permits a hardness up to 35 HRC (Hardness Rockwell C scale) providing a combination of characteristics (e.g. relatively high strength, corrosion resistance, good weldability) that overall produce a superior performance of the martensitic stainless steel over a prolonged life. There are other elements in low carbon martensitic stainless steels such as Cr, Ni, Mo, etc, that also affect the weld properties.

2.2.1 Alloying elements in martensitic stainless steels

In order to comprehend the properties of martensitic stainless steels and the related phenomena that happen in a weldment (FZ and HAZ), understanding the effect of the alloying elements used in these steels on the phase diagram are obligatory. Though the cooling and heating rates during welding are fast and thus the conditions are non-equilibrium, the equilibrium phase diagram can aid to explain and predict the phase transformation and phases in the weldment. The important alloying elements in 13%Cr-4%Ni are Fe, Cr, Ni, and Mo. Cr is a ferrite-stabilizer and restricts the austenite region, thus in alloys with more than 12%Cr, no austenite will remain as shown in the Fe-Cr phase diagram in Figure 2-6a. By increasing the Cr above 45%, a brittle intermetallic compound consisting of Cr and Fe, the σ-phase, will precipitate at approximately 820°C from δ. As can be seen in the phase diagram for steel with 13%Cr, there is not any transformation of $\gamma \rightarrow \alpha'$ (martensite), however to obtain a martensitic stainless steel, this transformation is needed. Therefore, the other alloying elements are added to take advantages of the $\gamma \rightarrow \alpha'$ phase transformation (Folkhard et Rabensteiner, 1988).

In order to have the $\gamma \rightarrow \alpha'$ phase transformation in 13%Cr stainless steel, Ni is added as an austenite-stabilizer to increase the γ region, as shown in Figure 2-6b to have a 13%Cr-4%Ni grade. The extension of the γ region and the lower $\gamma \rightarrow \alpha'$ phase transformation temperature can be seen clearly in Figure 2-6c. By increasing Ni from 0% to 6%, the start temperature of the $\gamma \rightarrow \alpha'$ phase transformation decreases about 200°C.

Carbon as another austenite forming element in martensitic stainless steel is usually kept lower than 0.06% in order to improve the weldability and meet the requirement of hardness and toughness in the weld and HAZ. Generally, Cr in presence of carbon is a strong carbide-forming element and specifically, in martensitic stainless steels may produce carbides such as $M_{23}C_6$ and M_7C_3. Figure 2-7 shows sections of the ternary Fe-Cr-C phase diagram at 13%Cr. It is evident that the carbide $M_{23}C_6$ (designated C_1 in Figure 2-7) might precipitate at temperatures below 700°C even at very low carbon contents (Folkhard et Rabensteiner, 1988).
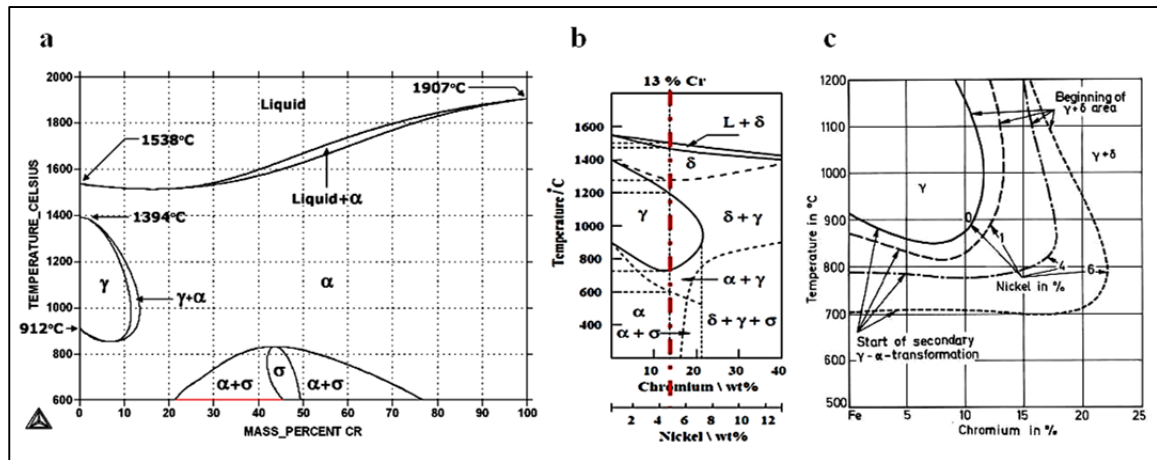
Figure 2-6 Phase diagram: (a) Fe-Cr, (b) Fe-Cr-Ni, and (c) Fe-Cr-with different Ni
(Folkhard et Rabensteiner, 1988)

The other element added to this grade of stainless steels is Mo. Mo is added up to 3%
to martensitic stainless steel to improve the corrosion resistance. It is also a ferrite-forming
element which restricts the austenite region. Thus it should be balanced with Cr, C, and Ni in
order to have the desired $\gamma \rightarrow \alpha'$ phase transformation. In addition to the aforementioned
elements (Cr, Ni, C, and Mo), there are other elements that may exist in martensitic stainless
steels such as Mn (austenite-former) and sometimes Ti (ferrite-former), and Nb (ferrite-
former) (Folkhard et Rabensteiner, 1988).
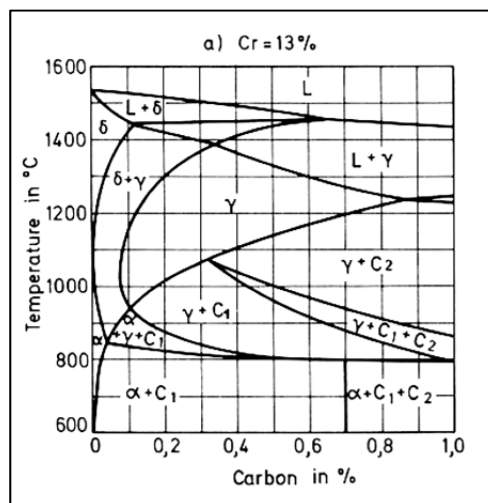
Figure 2-7 Ternary Fe-Cr-C phase
diagram at 13%Cr (Folkhard et
Rabensteiner, 1988),

2.2.2 Phase transformation in martensitic stainless steels

Phase diagrams show the equilibrium constituents of different alloys that are obtained at low heating and cooling rates. However, to form martensitic stainless steels, the alloy shouldn't cool at the equilibrium conditions. For example, the phase diagram indicated that at ~1450°C, the liquid solidifies to δ-ferrite, then at ~1230°C, δ-ferrite transforms to γ. Consequently, at ~700°C, γ → α' phase transformation occurs and α phase remains stable at room temperature. Actually, during welding, the alloy is supercooled, and other phases and microstructures may form, such as martensite, which is not predictable by the phase diagram. The other phases in martensitic stainless steels, which cannot be predicted by the phase diagram is the retained austenite at room temperature that may remain from γ → α' phase transformation. Applying PWHT including tempering at ~600°C, might also form a finely dispersed reversed austenite in which tends to increase the toughness (Niederau, 1982). These phases that are present after welding are due to the non-equilibrium condition and aren't accurately predicted by phase diagram, and the effect of the cooling rate on the microstructure may be investigated by means of a TTT diagram. An example of TTT diagram of 410 stainless steels is shown in Figure 2-8 (Atkins, 1980).
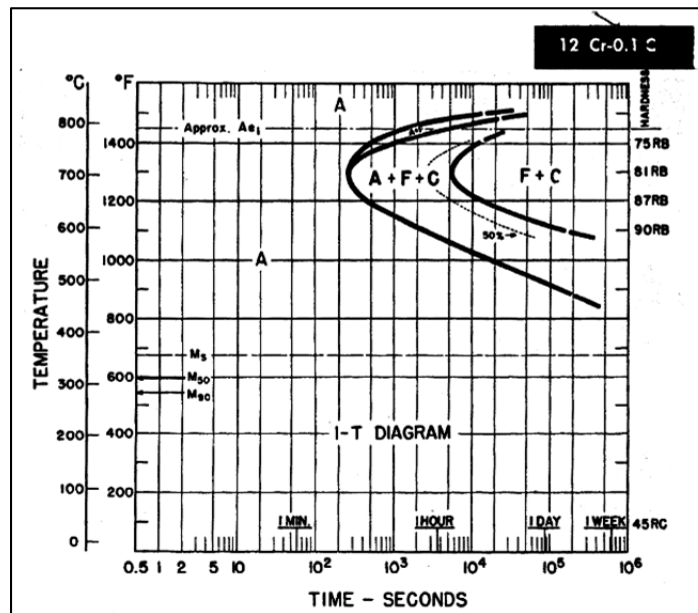
Figure 2-8 TTT diagram of 410
stainless steels (Atkins, 1980)

As Figure 2-8 shows, even at slow cooling rates, the final microstructure for the 410 stainless steel is predominantly martensite. By developing the steel manufacturing and producing a low carbon martensitic stainless steels, the nose of the transformation curve can be shifted to longer times in order to have martensite even at slow cooling rates.

2.2.3   Different zones in martensitic stainless steels weldment

Generally, the weld metal is exposed to the highest temperature during welding and on progress towards the HAZ, the temperature decreases until reaching the BM region where the microstructure is not affected. So, in the FZ the material is molten; however, in HAZ the transformations are in solid state. In fusion welding processes, the weldment is composed of three main zones including FZ, HAZ, and BM. The FZ of martensitic stainless steels contains predominantly martensite with up to 5% delta ferrite and up to 30% retained austenite that was observed in several studies with various welding processes (Carrouge, 2004; Enerhaug, 2001; Thibault, 2009). The fraction of each phase depends on the heat treatment of the as-received materials, chemical composition, PWHT, filler metal addition and welding process. The FZ micrograph of EB welded SMSS, as shown in Figure 2-9, reveals predominantly tempered martensite due to PWHT at 630°C ± 10°C for 30 min. Also a small amount of ferrite stringers are present.
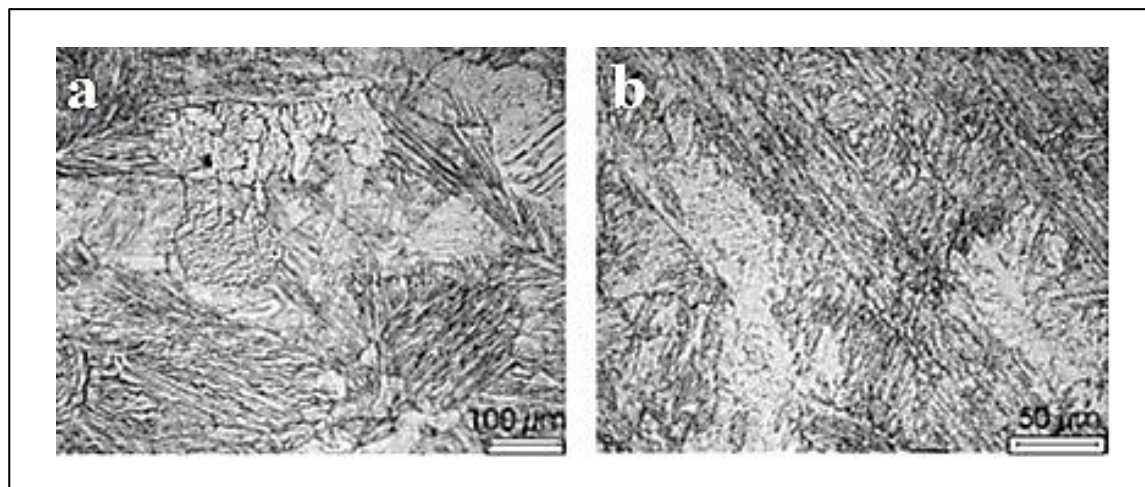
Figure 2-9 Optical micrographs revealing tempered martensite in FZ: (a) with dendritic structure and (b) higher magnification of (a) (Srinivasan et al., 2004)

20

The HAZ of this group of materials can be divided to several zones based on the different microstructure and phases, distinctive microhardness values and various responses to the etchant. Srinivasan observed distinct HAZs in 20 mm thick EB welded SMSS, as shown in Figure 2-10 (Srinivasan et al., 2004) which were in agreement with other researchers who used other welding processes, such as FCAW (Thibault, 2009) and GTAW (Carrouge, 2004; Enerhaug, 2001). However, it's noteworthy that these HAZs were identified differently in various research studies. The different regions of the HAZ in the EB weld of Srinivasan's study were referred to as coarse-grained HAZ (CGHAZ) adjacent to the fusion boundary, fine-grained HAZ (FGHAZ) and HAZ next to the BM, as shown in Figure 2-10.
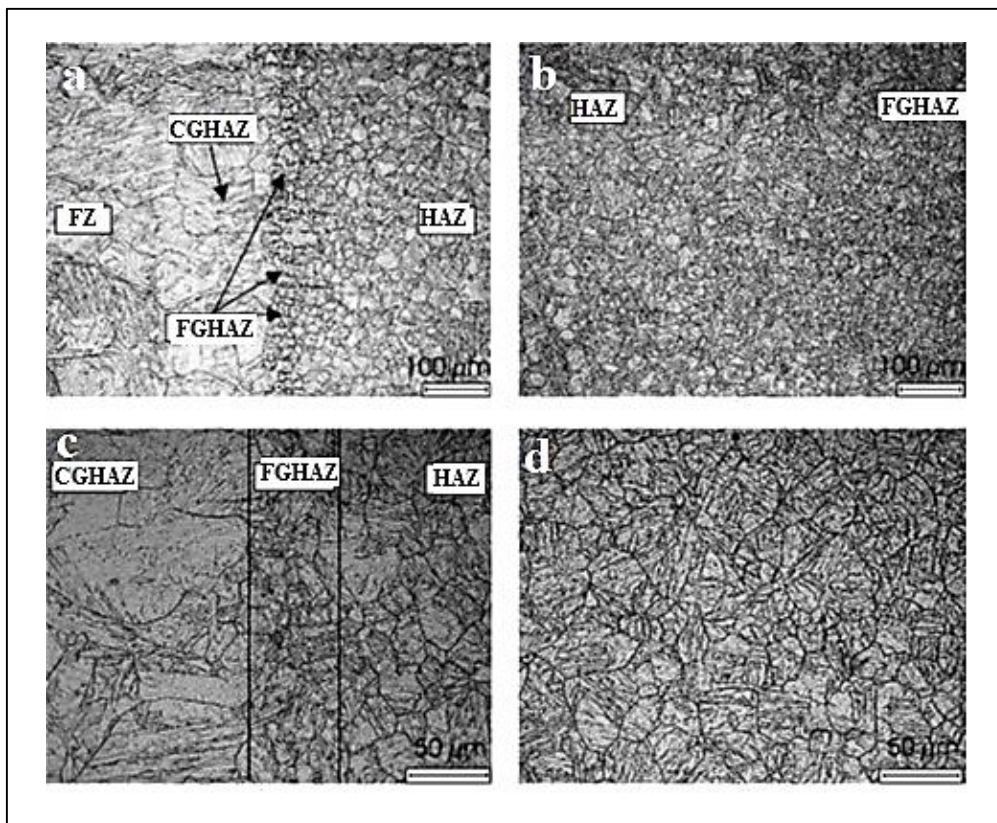
Figure 2-10 Optical micrographs of the EB SMSS weldment:
(a) FZ and 3 HAZs, (b) FGHAZ and HAZ, (c) CGHAZ and
FGHAZ at higher magnification, (d) HAZ zone adjacent to
BM at higher magnification (Srinivasan et al., 2004)

Considering previous findings on the microstructural evolution of the welded SMSS, the maximum number of regions that were recognized was in GTAW process performed by Enerhauge (Enerhaug, 2001) who described 5 distinct regions in the HAZs, HAZ1-5. Other researchers (Carrouge, 2004; Thibault, 2009) were unable to recognize HAZ1 and they defined only 4 HAZs in the weldment. In the present manuscript-based thesis, 4 HAZs were observed in the EB Weldment of the martensitic stainless steel and will be explained in Chapters 3 and 4. Based on the equilibrium phase diagram, as mentioned in previous section (Figure 2-6b), the HAZs of martensitic stainless steels can be divided into five distinctive zones (Enerhaug et al., 2001; Thibault et al., 2010) as below:

- Zone I: partially melted zone adjacent to fusion boundary that contains newly formed delta ferrite during heating.
- Zone II: completely transformation to delta ferrite on heating with significant grain growth and also referred to as coarse-grained HAZ or CG-HAZ.
- Zone III: partial transformation of austenite to delta ferrite on heating, and referred to as the high temperature dual-phase region.
- Zone IV: complete transformation of martensite to austenite on heating.
- Zone V: partial transformation of martensite to austenite on heating, and referred to as low temperature dual-phase region.

The microhardness evolution (Enerhaug et al., 2001; Thibault et al., 2010) proved the presence of various HAZs with the related microstructures. The microhardness profile in SMSS (Srinivasan et al., 2004) after PWHT is illustrated in Figure 2-11 and showed a maximum hardness value of 362 HV in the HAZ at a distance of about 5 mm from the weld centerline (adjacent to CGHAZ toward the BM) (Srinivasan et al., 2004).

22
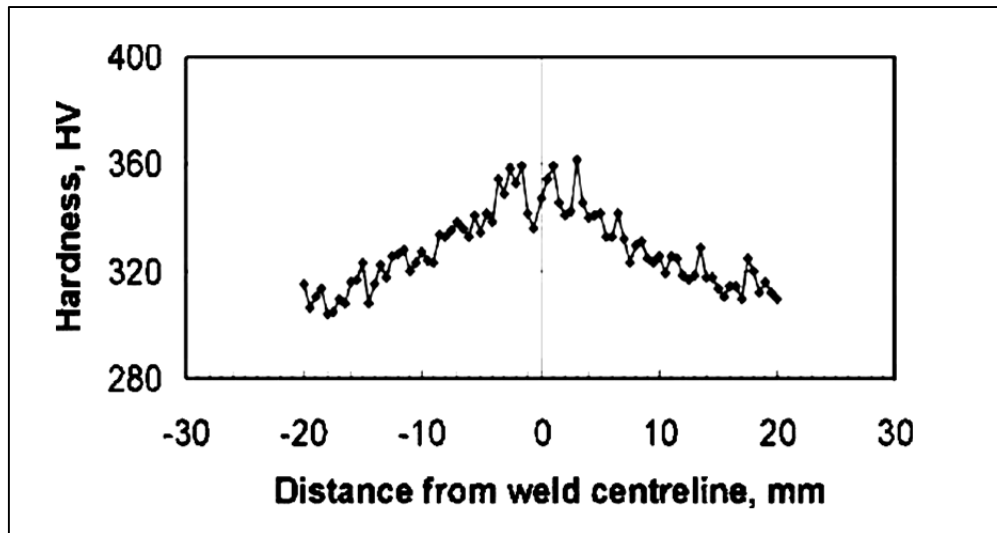
Figure 2-11 Microhardness profile of the SMSS EB weld
cross section after PWHT (Srinivasan et al., 2004)

2.2.4 Tensile properties in martensitic stainless steels

The cyclic stress induced by a turbine runner may lead to cracking in the components, thus the strength of the materials used in turbine runners has a significant effect on fatigue and rupture resistance. Generally, materials which have yield and ultimate strengths very close to each other, may fail in a brittle manner. Therefore, tensile properties must be considered as an important factor in material and weld metal selections for turbine runners. Commonly, the tensile properties mean the global tensile properties that depend on the failure zone of the weldment and may have a combination of BM, FZ, and HAZ properties. On the other hand, the global tensile properties only determine the properties at failure location which is affected by other zones. For instance, if the failure location is in BM, global properties are mostly related to the BM as well as the effects of the FZ or HAZs which are located outside of the failure location. Tensile fractographs of the EB welded SMSS (Srinivasan et al., 2004), as illustrated in Figure 2-12, showed the typical ductile fracture with dimple structure.
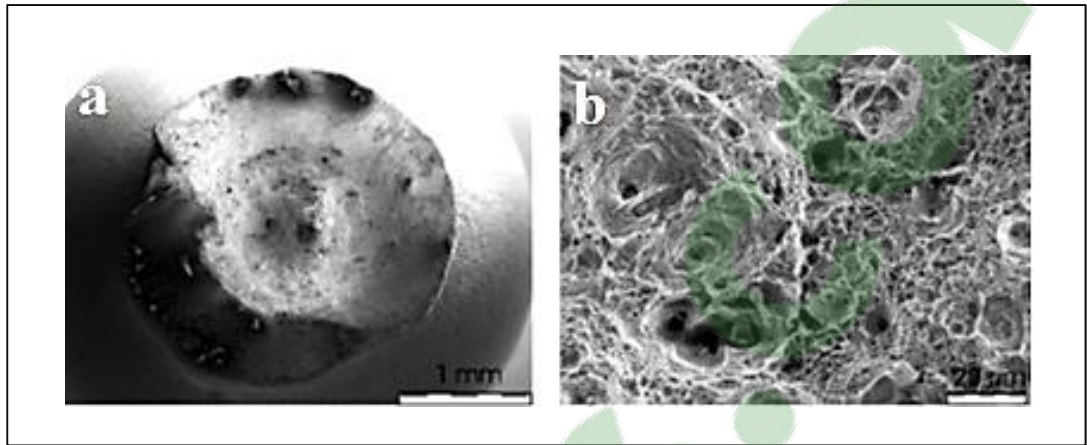
Figure 2-12 Fracture surface appearance of EB welded SMSS tested in air: (a) an overview of the fracture (showing the cup and cone fracture) and (b) fracture surface showing dimples (Srinivasan et al., 2004)

The tensile samples of the EB weld failed in the BM and demonstrated lower ductility and tensile strength compared to BM which can be probably due to the composite-like structure of the tensile sample including FZ, HAZs, and BM. From global tensile test results, it can be concluded that the FZ tensile properties in EB welded SMSS are stronger than the BM tensile properties, but to understand the exact values it is necessary to test locally in different zones of the weldment.

Therefore, the idea of measuring the local tensile properties of each zone in the weldment developed to help understand the effect of different heat treatment conditions, welding properties and ductility in different locations of the weldment. By considering this idea, researchers interested in measuring local properties deliberately prepared miniature tensile samples which needed accurate machining and equipment (Cam et al., 1999). By developing technology and photography equipment, the DIC system was introduced as a new tool to measure the local properties during tensile testing (Abu et al., 2012; Dalgaard et al., 2012). By utilizing DIC, it becomes possible to measure the local tensile properties by only testing one tensile sample. To the best knowledge of the author, in spite of the availability of DIC for more than three decades, there hasn't been any study about local properties of EB welded martensitic stainless steels without filler addition by only one pass.

2.3 Principles of DIC

DIC is an optical 2D or 3D non-contacting technique for measuring the surface displacements during mechanical testing and forming (Leclerc et al., 2009; Lockwood et Reynolds, 2003; Pan et al., 2009; Reynolds et Duvall, 1999). DIC requires capturing a set of images before (reference image) and after deformation (deformed image) from the measured surface which contain a random texture such as a speckle pattern (spraying black airbrush on white background) as shown in Figure 2-13. The speckle size, speckle density, type of algorithm, subset size, subset overlap, and gray level interpolation should be optimized obtain an accurate DIC results. Subsets are defined as small rectangular regions which consist of n×n pixels in a reference image (Tang et al., 2012).

Figure 2-13 Speckle pattern on the measured surface

Basic theory of DIC that has been studied since 1980s (Ackermann, 1984; Leclerc et al., 2009; Moser et Lightner, 2007; Peters et Ranson, 1982), is to track a random gray pattern in a subset, between a reference image and a deformed image. The newer technique of DIC is 3D DIC method that is based on the stereovision system (Orteu et al., 2011) and utilizes two cameras from different angles at the same time to capture the 2D images at the same area of the object as shown in Figure 2-14. The calibration of cameras to determine the position and orientation of the camera and focal length of the lenses (Hild et Roux, 2006) are essential to have accurate results. The 3D contours of strain are then obtained using the best combination of two CCD cameras to match each point of the deformed images. As shown in Figure 2-15, points of each camera in a given stage are matched together in order to be a physical point. This matching procedure is called stereo match. Then, each point of the reference image and deformed image are matched together, which is called temporal match. After all matching processes are finished, 3D coordinates of all the point can be obtained through triangulation method using stereo and temporal matches. By comparing the coordinates of each point in

each stage with the reference stage, the displacement of that point can be calculated at the stage of interest (Bornert et al., 2009).
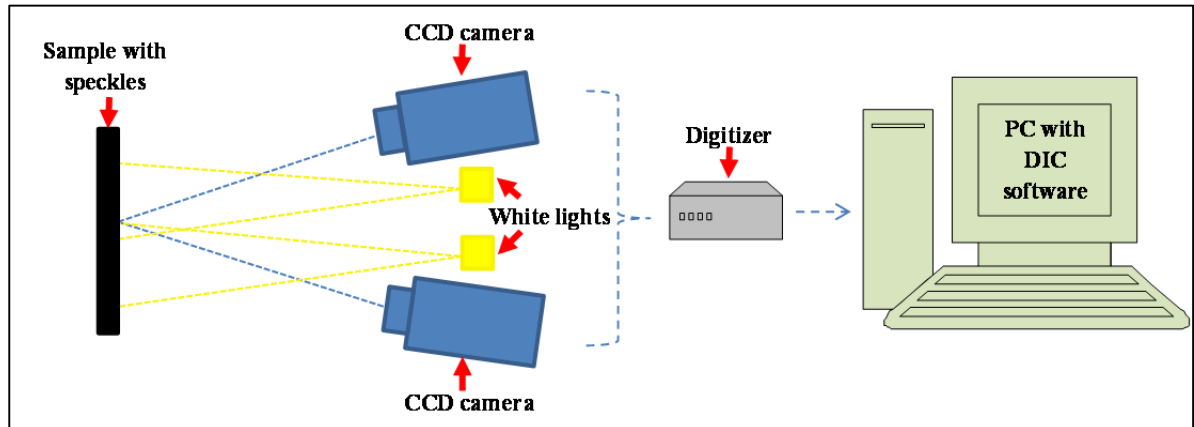
Figure 2-14 Typical schematic of the 3D DIC technique.
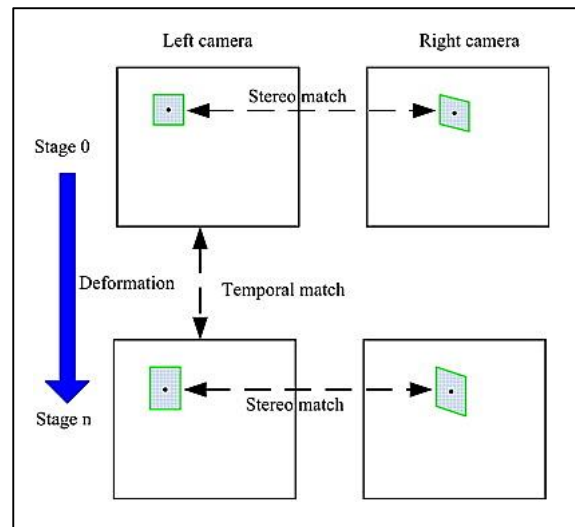
Figure 2-15 Schematic illustration of
matching procedures of the 3D DIC
(Tang et al., 2012)

The 3D DIC methodology with two cameras and stereo-vision has been developed in different studies (Grytten et al., 2009; Kabir et al., 2012; Reynolds et Duvall, 1999; Wanjara et al., 2014) for various welded materials in order to determine full-field displacements during uniaxial tensile tests on the weldment as a heterogeneous material including FZ, HAZ, and BM. Utilizing two cameras provide the ability of observing the surface from different

directions and finding a 3D coordinate of any point. By comparing the changes between a reference images and series of images taken after load is applied, full-field three-dimensional displacements can be measured. This methodology has the advantage of determining the local properties of each zone of the weldment with minimum equipment along with a good repeatability and reliability of results.

2.3.1 Application of 3D DIC for local tensile properties in welded samples

Generally, the global strength of the weld depends on the distribution of properties across the different zones of the weldment including FZ, HAZ, and BM. Thus, weldment can be considered as a composite-like structure with distinct local properties. For many years mechanical characterisation of the weld has been addressed by the global properties of the weldment, however these global properties may not be a good representative for different locations across the weldment. Also, for achieving the local properties it was needed to extract miniature samples from each zone in order to characterize the weldment locally. Presently, by improving the imaging system such as DIC, there is possibility to use one standard sample and simultaneously obtain local properties in different zones. The 3D DIC has been increasingly used for close to 20 years as a very applicable tool for displacement measurements (Reynolds et Duvall, 1999) of mechanical testing such as tensile testing providing the local stress–strain curves across the weldment (Kabir et al., 2012; Leitão et al., 2012; Wanjara et al., 2014).

As abovementioned, the DIC can provide the local stress-strain curves with considering different gage lengths. Contrary to DIC, the extensometer usually used in tensile testing can only determine the displacement of the whole length and consequently provides a single stress-strain curve. However by DIC, different gage lengths can be evaluated per single test. Research done by (PI et al., 2010) showed that the result of DIC was in good agreement with the curve measured by extensometer with the same gage lengths as shown in Figure 2-16. In addition, by considering different gage lengths of 1.5, 3, 6, 12.5, 20 mm (line1.5, line3, line6, line12.5, and line20); the local true stress-strain curves were displayed for various gage lengths. The gage length of the sample which calculated by extensometer was 50 mm and therefore, the difference between the curves calculated by extensometer and DIC can be

attributed to the difference in gage length between in extensometer measurement and DIC measurement. Different curves shown in Figure 2-16, demonstrated that by increasing the gage length toward the whole gage length of sample, the DIC curve approaches the extensometer curve.
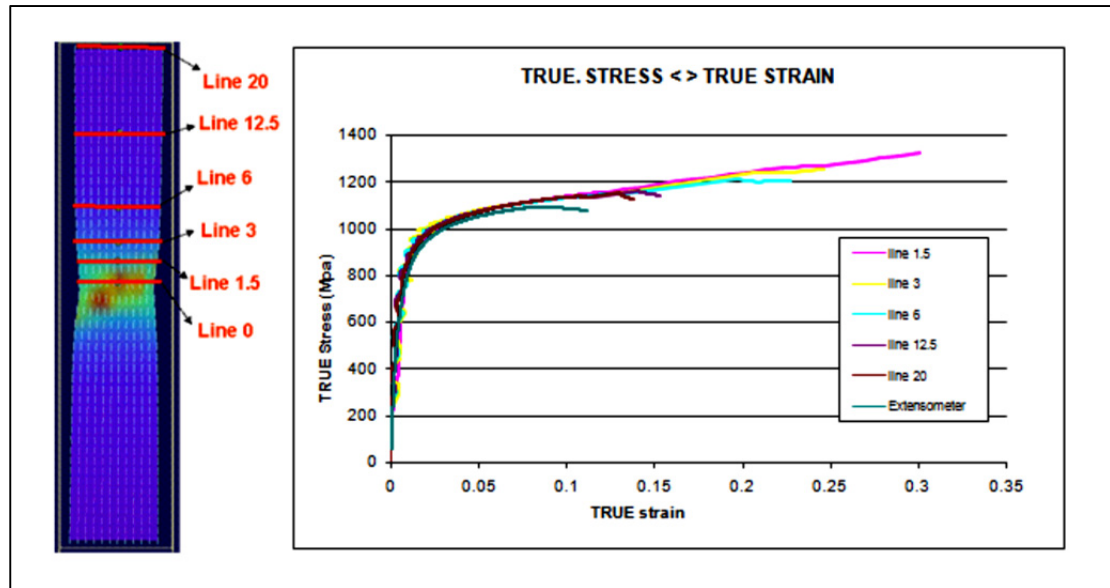
Figure 2-16 True strain-stress curves calculated by extensometer and DIC with different gage lengths (PI et al., 2010).

To the best of author knowledge, there isn't any study on the local properties of EB welded low carbon martensitic stainless steel. Thus, in the present manuscript-based thesis, the procedure used for measuring tensile properties is similar to aforementioned procedure, with a little difference that there is combination of FZ and HAZs in the EB welded low martensitic stainless steel at the middle of tensile samples. Therefore, for measuring the local properties of each zone, the gage length must be defined the same as each zone of interest. For example, for local properties of the FZ, the gage length shall establish the same as the length of FZ. Therefore, before testing, the tensile samples on the opposite side of speckles side were etched and then each zone including FZ and HAZs was carefully measured as will be described in detail in Chapter 4.

2.4   Weld distortion and residual stresses

2.4.1   Measurements of residual stress by contour method

The residual stresses can be measured by different techniques such as destructive or non-destructive techniques. For example in lifetime assessment of structures such as bridges, aircraft structures, offshore platforms or in-service turbines, that need to be periodically inspected in the field, the non-destructive techniques are preferred. Non-destructive techniques use some inherent physical properties of the sample in order to determine the stress state. By comparison, in the destructive techniques including sectioning, contour, hole-drilling, ring-core and deep-hole, residual stresses are calculated by the measurement of deformations due to the releasing of residual stresses upon removal of material (Lachmann et al., 1999).

Among different methods, the neutron diffraction and contour methods were paid more attention in the literature for thick welds. These methods were compared in FCAW of low transformation temperature 13%Cr–4%Ni in as-welded condition (Thibault et al., 2010). It was concluded that in HAZ of 13%Cr–4%Ni material because of the presence of retained austenite, the residual stress measured by neutron diffraction method is higher than contour method because the former methods used only strains in martensite. In addition, neutron diffraction method needs to measure the lattice parameter which is hard in the HAZ since its value varies in this zone. Therefore, our focus will be measuring residual stress by contour method for thick gage section of welded parts as is described in Chapter 5.

The contour technique is a destructive technique of measuring residual stresses in one direction, in a 2D plane through a weld. The technique consists of three main stages, as shown schematically in Figure 2-17. In the first stage, the surface on which its residual stress measurement is desired; is cut using wire-EDM. The residual stresses of the surface will be released by cutting and cause a deformed surface. In the second stage, the surface profile of the deformed surface is measured using a co-ordinate measurement machine (CMM) with either a touch trigger probe, or a laser attachment. The third stage is the data analysis to convert 3D surface contour into 2D stress field, namely the filtering of the raw data array and

the superposition of the surface contour in a FE model. The FE model forces the deformed surface to return to the flat surface. The forces required to bring back the deformed surface to the flat surface are equivalent to the stresses that originally existing within the welded material (Prime et DeWald, 2013).
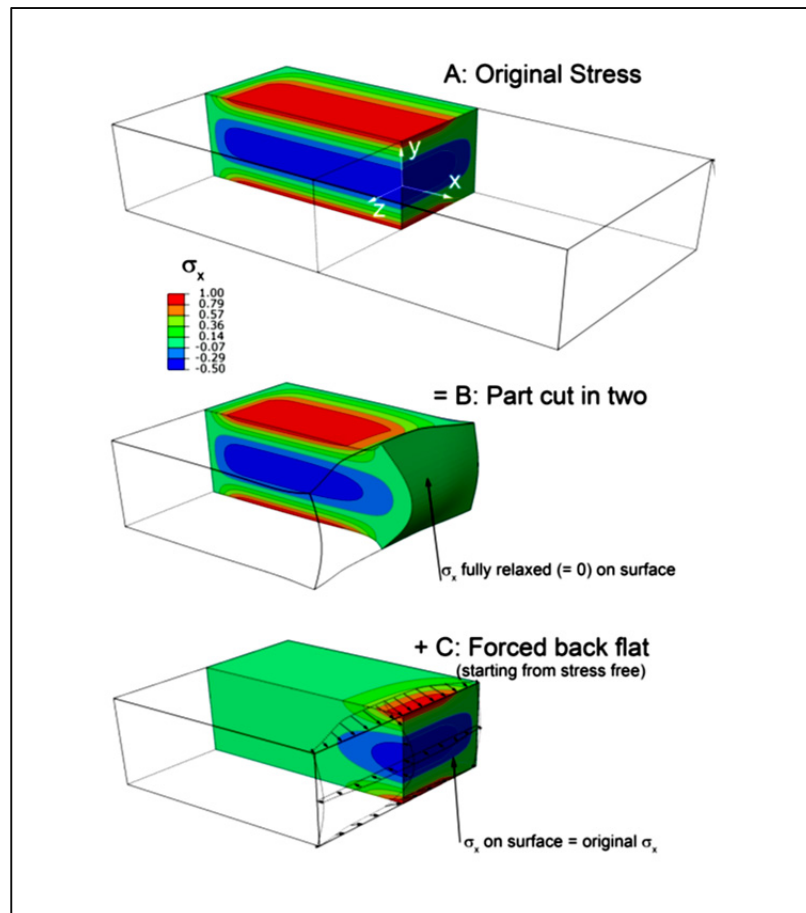
Figure 2-17 Contour method principle for mapping
residual stresses on one quarter of the original body
(Prime et DeWald, 2013)

The raw data measured by CMM may have the 'noise' inputs such as the surface roughness from EDM. Therefore, the raw data needs to be filtered and smoothed before being applied to the FE model. As shown in Figure 2-18 after measuring the contours of both sides of the cut, the contours must be averaged to remove errors caused by antisymmetric cutting effects (Prime et DeWald, 2013).
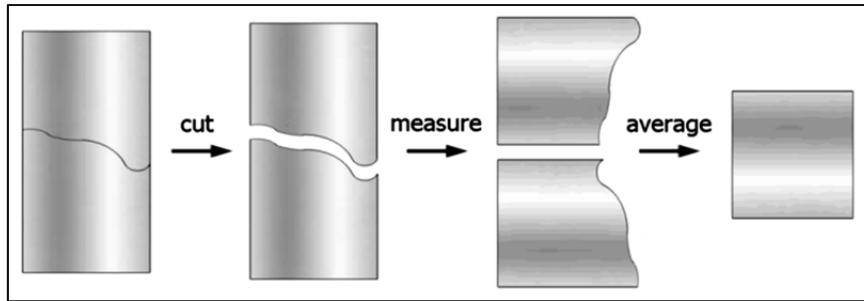
Figure 2-18 One solution to remove errors due to the EDM cut

2.4.2   Effect of phase transformation on distortion and residual stresses in welding

The determination of turbine runner properties including fatigue lifespan, distortion, dimensional stability, and failures can be noticeably affected by residual stresses in weldments (Totten, 2005). Residual stresses in weldment can be defined as stresses that left in the part after welding in absence of thermal gradients or external forces. The welding-induced residual stress may be the result of different contractions which occur during cooling to room temperature. As a consequence of non-uniform heat distributions, plastic deformations and phase transformations occurring across the weldment, different residual stresses patterns for the weld region and the heat affected zone (HAZ) are generated. For instance, as shown in Figure 2-19, residual stresses induced by shrinkage usually produces tension in the FZ. By contrast, residual stresses induced by transformation form compression state of residual stresses in FZ (Macherauch et Hauk, 1987). Therefore, the idea of having a compressive residual stress in FZ by reducing the phase transformation temperature attracted the researchers' attention to develop the low transformation temperature martensite material as filler addition in order to diminish the need for post processes such as hammer peening (Simoneau et al., 2009). Ohta et al. in 1999 (Ohta et al., 1999) welded a 20 mm thick JIS SPV490 steel with a low transformation temperature filler wire of M_S ~180°C and M_f ~room temperature. By contrast, usual welding wires had M_S ~500°C –400°C and the results showed higher residual tensile stress for the wire with higher M_S because the net strain in this wire was contraction and caused tensile residual stresses.

The formation mechanism of compressive residual stress in low transformation temperature welds can be explained in relation to M_s and M_f temperatures, as shown in Figure

2-20 (Shiga et al., 2010). Shiga et al. in 2010 used butt welded joints of 20 mm thickness and 200 mm width in order to assure that the residual stress may be generated by only thermal stress due to the weld shrinkage. Figure 2-20 is a schematic explaining the formation mechanism of residual stresses arising from different thermal stress behaviour among three different materials with various M_s of 460°C, 244°C, and 60°C. In material with M_s of 460°C as a conventional material, during cooling after welding, the thermal stress decreased to M_f of 220°C and it then increased from the M_f to room temperature up to 400-450 MPa. By contrast for the other two materials with low transformation temperature of M_s 244°C and 60°C, the thermal stress of weld metal continuously was reduced and had compressive stress and then increased to about -300 MPa, again in the range of compression stress because their M_f were low. Thus, with the lower M_s and M_f temperatures, the more compressive residual stresses form (Shiga et al., 2010).
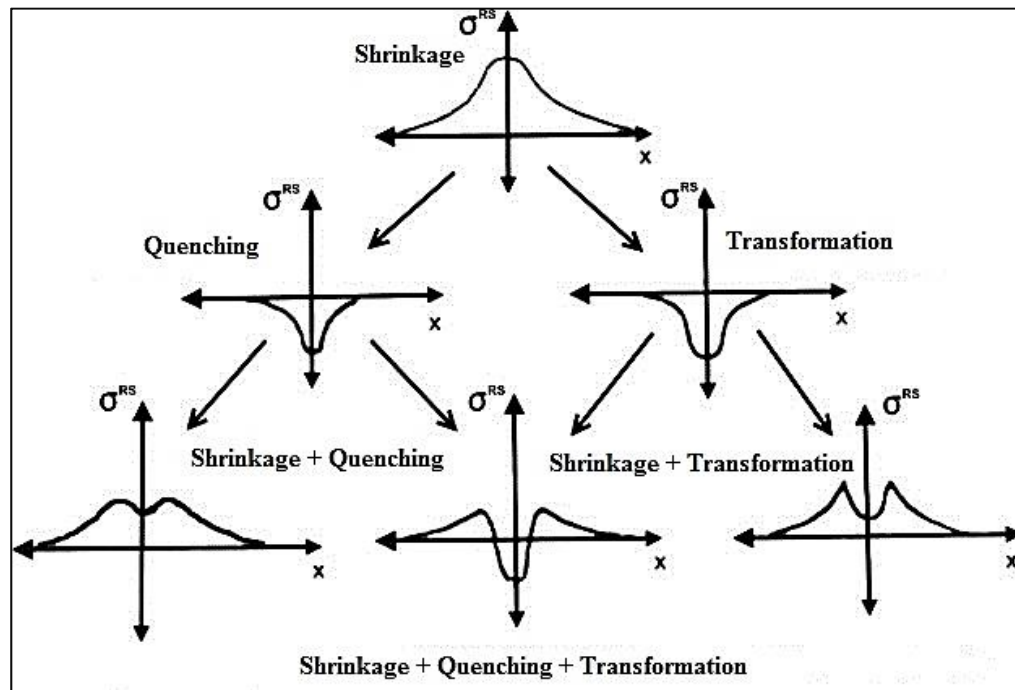
Figure 2-19 Change of residual stress due to
metallurgical processes during welding
(Macherauch et Hauk, 1987)
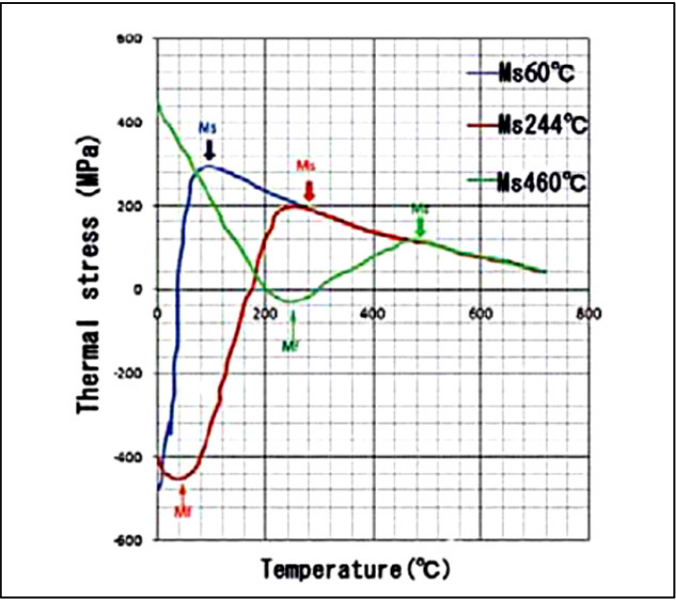
Figure 2-20 Schematic diagrams
representing the formation mechanism of
residual stresses in relation to M_s and M_f
temperatures (Shiga et al., 2010)

The low transformation temperature of martensite may also effect the distortion of the weldment as studied by Bhadeshia (Bhadeshia, 2004). He concluded that the angular distortion in welds with lower transformation temperature of martensite is lower as shown in Table 2-1.

Table 2-1 The chemical compositions (wt.%), calculated transformation
temperature range (ΔT (℃)) and measured distortion θ for two manual metal
arc, multi-pass weld deposits (Bhadeshia, 2004)

	C	Si	Mn	Ni-	Mo	Cr	ΔT (℃)	θ (°)
Wt.%	0.06	0.5	0.9	-	-	-	802-400	14.5
Wt.%	0.06	0.3	1.6	1.7	0.4	0.35	422-350	8

2.5   Conclusions

In the current chapter, various major aspects of EBW were presented. Also, the microstructure and phase constituents of low carbon martensitic stainless steels and their tensile behavior by utilizing DIC for investigation of local tensile properties were reviewed. In addition, residual stress and distortion induced by welding affected by phase transformation temperature were described, focusing on the contour method. Finally, this review has led us to conclude that:

- There is a substantial need to develop an advanced welding process such as EBW as an alternative process for manufacturing hydroelectric turbine runners which are made of thick gage section of materials. The main benefit is to eliminate the need for filler addition and multi-pass welding processes.

- There is no research on the EBZHT for preheating before EBW. Therefore, applying the EBZHT as preheating, particularly for thick gage section of hydroelectric turbine materials is pioneer research in this domain.

- A few studies have focused on using DIC for measuring the local tensile properties. But no work is present for local tensile properties in different weldment zones of low carbon martensitic stainless steels.

- Only one study exists for welding-induced distortion measurement by DIC which utilized a methodology different from that the used in the present work. Therefore, according to literature review, welding-induced distortion measurement by automated optical measurement system has yet to be studied. To the best knowledge of the author, no research on characterizing the local tensile properties and welding-induced distortion measurement by DIC has been undertaken for low martensitic stainless steels welds.

- Very limited studies have been reported for residual stresses measured by contour method for thickness of 50 mm. There is no reported work on residual stresses measured by the contour method (or any other technology) in a thick gage section of low carbon martensitic stainless steels assembled by EBW.

CHAPITRE 3

CHARACTERISTICS OF AN AUTOGENOUS SINGLE PASS ELECTRON BEAM WELD IN THICK GAGE CA6NM STEEL

S. Sarafan [a], P. Wanjara [b], H. Champliaud [a] and D. Thibault [c]

[a] École de technologie supérieure, Montréal, Québec, Canada H3C 1K3
[b] National Research Council Canada, Aerospace, Montréal, Québec, Canada H3T 2B2
[c] Institut de recherche d'Hydro-Québec (IREQ), Varennes, Québec, Canada J3X 1S1

3.1   Abstract

CA6NM is a low carbon martensitic stainless steel that is widely applied in hydroelectric turbine manufacturing. Using conventional fusion welding techniques, the fabrication of a thick section in CA6NM requires a V-groove joint design and multiple passes to achieve the required penetration. However, exposure to a substantial heat input through this process renders large fusion and heat affected zones, microstructural variations as well as distortion of the assembly, which pose difficulties for the manufacture and performance of the component. The application of a high energy density technique, namely electron beam (EB) welding, was used in the present work to penetrate a 60 mm thick section in CA6NM with a single pass without filler metal. To prevent cracking in the weldment, the CA6NM was heated to 100-170°C before EB welding using a zonal preheat treatment, which was applied in-situ using a defocused beam. The as-welded CA6NM exhibited a narrow fusion zone (FZ) and a series of distinct yet very small heat-affected zones (HAZ) with different microstructural characteristics. As compared to the base metal (BM) hardness of 289±4 HV, the EB weldment exhibited a hardness maximum of 425 HV in the HAZs and an average hardness of 395±6 HV in the FZ. Post-weld heat treatment (PWHT) was effective in lowering the hardness in the FZ of the EB weldment to a mean value of 346±13 HV.

36

3.2   Introduction

Hydroelectric power is a competitive and efficient source of renewable energy that currently represents 16% of the global electricity generation (Kumar et al., 2011). Though hydropower is a mature technology for electricity generation that may not require scientific breakthroughs to increase the global energy supply, research and development is still necessary for improving product reliability and safety, reducing manufacturing costs of small- and large-capacity installations as well as decreasing the operational, maintenance and replacement costs of the primary machinery/elements in existing hydropower plants. As a consequence, a priority for research and technology development is the advancement of cost-efficient design, manufacturing and repair of materials for the turbine, the core element of the hydropower system, which is engineered to operate for decades in a hydro-abrasive environment (erosion, corrosion, cavitation) with little maintenance and periodic overhaul every few years.

In deliberating the relative geometric dimensions of hydropower turbine elements, it is unsurprising that the manufacturing challenges for shaping and assembly are considerable. The choice of shaping methods for the fabrication of parts includes casting, forming and material removal (machining, grinding, and polishing). These pre-fabricated parts are then assembled, currently, by different welding techniques, such as manual metal arc welding, gas tungsten arc welding (GTAW) or semiautomatic techniques such as gas metal arc welding (GMAW) with solid wires or flux cored wires. Traditionally, the application of high energy density joining technologies, such as laser beam welding and EB welding, was not considered due to the site welding requirements and size-related complexities of the parts to be assembled or repaired. However, with the recent advancements in these technologies in combination with advanced computer aided design, the manufacturing requirements for assembly of hydropower turbine elements may be addressable through weldability research and development.

In the present work, EB welding was investigated for joining hydropower turbine materials using a high energy density technology. EB welding is a mature manufacturing technology that has a demonstrated capability to join thick gage section materials in a single pass with considerably lower heat input than conventional arc processes (Handbook, 1993; Meleka, 1971; Schultz, 1993). The weldment is characterized by a higher depth to width ratio, narrower FZ and HAZ, and lower distortion compared to other conventional arc welding processes. The application of EB welding in a vacuum environment prevents contamination of the molten weld pool from atmospheric elements, and as well minimizes diffusion/divergence of the focused electron beam from scattering and ionisation that would occur under atmospheric pressure (Handbook, 1993; Schultz, 1993).

This research is a part of a larger program (CReFaRRE) targeted at developing novel technologies for manufacturing hydroelectric turbines. In the present paper the weldability of CA6NM, a 13% Cr–4% Ni low carbon martensitic stainless steel with a cast microstructure, was characterised. Based on the optimised parametric conditions, in-situ preheating and EB welding of 60 mm thick CA6NM was performed. Microstructure examination in combination with the Fe-Cr-Ni phase diagram was employed to interpret the phase transformations occurring across the weldment and the resulting microhardness evolution.

3.3   Experimental procedure

3.3.1   Material

The material conditions (alloy, thickness, heat treatment) selected in this study were defined by the design specifications for hydroelectric turbine manufacturing. Specifically, 60 mm thick normalized and tempered castings of ASTM A743 (ASTM-A743/A743M) grade CA6NM, with a chemical composition (wt. %) of 12.4% Cr, 3.51% Ni, 0.738% Mn, 0.056% C, 0.519% Mo, 0.538% Si, <0.003% Ti, 0.035% P, 0.001% S, were selected from the Litostroj Group. It is noteworthy that welding of CA6NM castings is recommended in the heat treated, single- or double-temper, condition over the as-cast condition (ASTM-A487/A487-93, 2012; Handbook, 2004). As indicated in Figure 3-1a the CA6NM castings were normalized by heating to 1050°C for 6 hours followed by cooling in air to below the

martensite finish temperature (Mf) of 90°C (Côté, 2007). The material was then given two temper treatments, namely a 610°C temper followed by a 590°C temper, as illustrated in Figure 3-1a. As illustrated in optical microscopy image (OMI) given in Figure 3-1b, the as-received cast microstructure of the normalized and tempered CA6NM reveals predominantly martensite laths. This is consistent with that reported in the literature (Carrouge et al., 2004; Enerhaug et al., 2001; Thibault et al., 2009), but depending on the heat treatment, other phase constituents can also be present, including up to 5 vol. % ferrite and up to 30 vol. % of retained austenite (Bilmes, 2001; Carrouge, 2004; Enerhaug, 2001; Thibault, 2009; 2011).

3.3.2   Preparation for welding

The as-received CA6NM plates (in the normalized and tempered condition) were machined to obtain coupons with dimensions of 200 mm in length, 40 mm in width and 60 mm in thickness, as illustrated in Figure 3-2. Prior to welding, the surfaces of the coupons were degreased with acetone, followed by fine grinding with a scouring pad and final cleaning with ethanol to remove any surface contamination. The coupons were then demagnetized using an enclosed demagnetizer (R.B. Annis 4.5" × 14") followed by a surface demagnetizer (Electro-Matic model A13-1) to achieve a surface magnetic field reading between 0 and 1 gauss (Bakunov et al., 2004). It is noteworthy that a residual magnetism lower than 5 gauss is recommended in (02-855/2:2010, 2010) to prevent interference with the welding procedure.

The coupons were then fixed to the worktable of the EB welding system using a clamping fixture. It is worth mentioning that as the EB welding parameters typically ramp up to the programmed conditions at the start of the weld procedure and ramp down to zero at the end of the weld procedure, 'run on' and 'run off' lengths were established, as identified in Figure 3-2. To allow a stable weld length of about 200 mm, 'run on' and 'run off' tabs, each ~20 mm in length, were tacked to the coupon on either end.
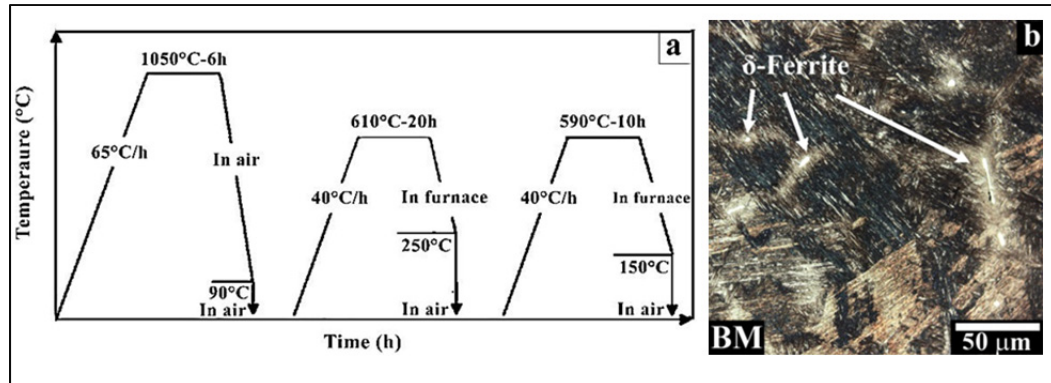
Figure 3-1 (a) The normalizing and tempering thermal cycles applied to the cast CA6NM material (b) the as-received cast microstructure of the normalized and tempered CA6NM (OMI)
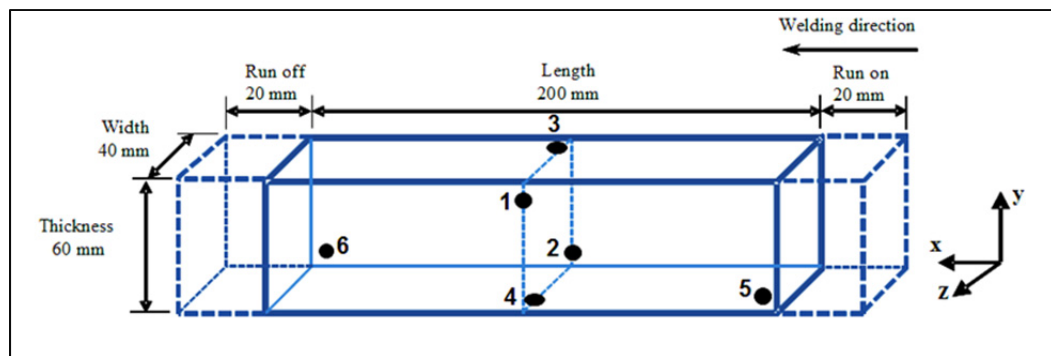
Figure 3-2 Schematic of the CA6NM coupon (with dimensions) used for BOP welding. The run on and run off tabs as well as the location of the different thermocouples are indicated.

3.3.3   Welding Procedure

The recommended guideline for welding CA6NM includes preheating, especially for thick gage sections, to temperatures of 100°C-170°C (Handbook, 2004). The preheat temperature must be applied throughout the entire thickness of the section and must be monitored using thermocouples, a contact pyrometer or temperature-indicating crayons. To preheat the CA6NM coupons, an electron beam zonal heat treatment (EBZHT) (Chen et al., 2002) was developed in the present work using a defocused beam that was oscillated in a circular path on the top surface of the CA6NM coupons along the longitudinal direction, as illustrated in Figure 3-3. The temperature distribution in the different regions of the coupon

was measured using a series of K type thermocouples (typically 6) affixed at different locations, as illustrated in Figure 3-2. The temperature from each thermocouple was acquired via wireless data recording with a Universal Wireless Thermocouple Connector (UWTC). Multiple EBZHT passes were conducted to achieve the required temperature range throughout the entire coupon. Upon reaching the required preheat temperature, autogenous bead-on-plate EB welds were produced along the length of the coupon using a set of parameters chosen to achieve full penetration in the 60 mm thick section. In particular, using a 42 kW Sciaky W2000 EB welding system (60 kV/700 mA) operating with pressure lower than 6.7×10^{-3} Pa, a heat input of 94.5 J·mm^{-1} with a 10% defocused electron beam positioned at 45 mm below the top surface of the coupon allowed full penetration and an integral weld with minimized spiking at the weld root (i.e. smoothened under bead).
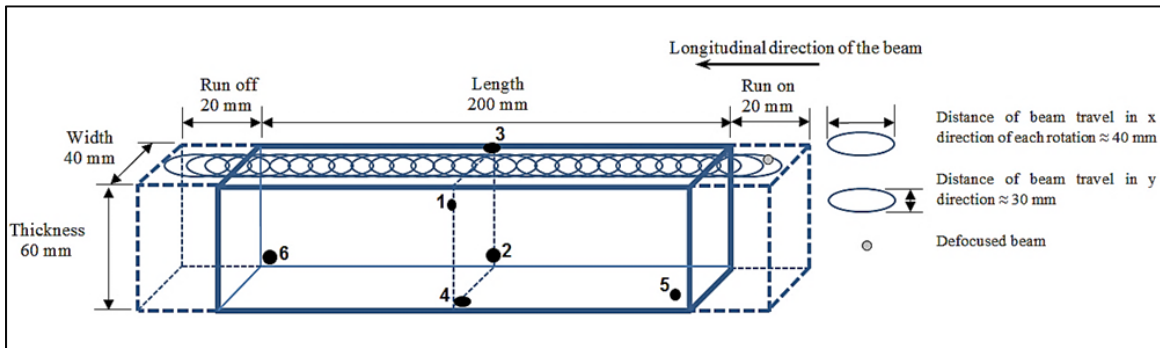
Figure 3-3 Preheat treatment of the coupon

The recommended guideline for PWHT is to cool the welded CA6NM to 95°C or below to ensure that the martensite phase transformation is complete prior to re-tempering between 565°C to 620°C (ASTM-A487/A487-93, 2012). In the present work, transverse slices, with dimensions of 20 mm in length, 20 mm in width and 60 mm in thickness, were cut from a fully penetrated CA6NM EB weld and heat treated at 600±5°C for 9.5 hours with a heating rate of 50°C/h and cooled in air, as illustrated in Figure 3-4.
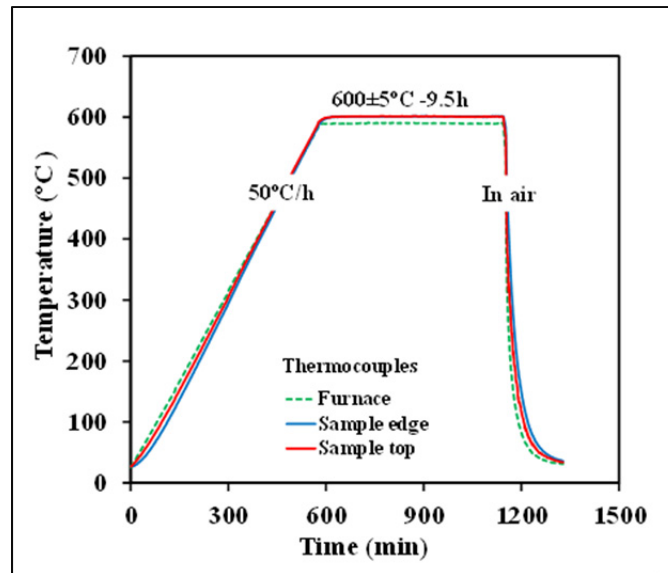
Figure 3-4 Post-weld heat treatment cycle
applied to the EB weld

It is notable that the temperature was monitored and controlled using K-type thermocouples; two thermocouples were attached to the sample surface to measure the temperature at two locations (center and edge) and another to control the furnace temperature.

3.3.4　Metallographic and microhardness testing techniques

The CA6NM EB welds (with and without PWHT) were sectioned transverse to the welding direction (plane Y-Z in Figure 3-2) to extract specimens from within the stable region for metallographic preparation and subsequent microscopic examination. Specifically, after sectioning of the EB welds using an abrasive cut-off wheel, the specimens were ground with 220 and 800 grit SiC papers followed by rough polishing using 9, 3 and 1 μm diamond suspensions with an alcohol based lubricant on silk polishing cloths. Final polishing was conducted using 0.05 μm colloidal silica on a porous pad. To reveal the general microstructural features, electrolytic etching of the specimens was performed by immersion at room temperature for 20 seconds in a solution of 10% oxalic acid with a voltage of 6 V at a current of 1.6 A using an austenitic stainless steel cathode. To improve differentiation of the various phases in the general microstructure of the different regions of the weldment, the

specimens were chemically etched at room temperature by immersion for 10-35 seconds in Vilella's reagent (5 mL HCl, 1 g picric acid, 100 mL methanol). Selective etching for δ ferrite phase was performed by electrolytic etching at room temperature in a 20% aqueous solution of NaOH (~10 seconds) with a voltage of 6 V at a current of 1.6 A using an austenitic stainless steel cathode (Wanjara et Jahazi, 2008).

An optical microscope (Olympus GX-71) was used to examine the microstructural characteristics of the weldments in the FZ and HAZ at magnifications up to 1000x. Image analysis software (AnalySIS Five) on the optical microscope was used to quantify the δ ferrite fraction. Also, secondary electron imaging (SEI) was performed at 20 keV on a Hitachi S-3600N scanning electron microscope (SEM) equipped with energy dispersive X-ray (EDX) analysis system to perform local compositional analysis in the HAZ.

To measure the retained austenite fraction at room temperature, X-ray diffraction (XRD) studies were carried out on selected specimens extracted from the as-received CA6NM material (in the normalized and tempered condition) and the EB weld. For the latter, the FZ was sampled in the as-welded and PWHTed condition. Specimens that were 3 mm thick, 10 mm in length and 10 mm in width were prepared by grinding with 1200-grit SiC paper and chemical etching in an aqueous solution of 30% HCl and 30% HNO_3. The X-ray diffraction data were collected at room temperature using a Bruker AXS D8-Advance diffractometer with CuKα radiation (wavelength of 0.15418 nm) at 40 kV and 30 mA. The diffraction angle (2θ), at which the X-rays impinged the specimen surface, was varied from 40° to 140° with a step size of 0.05° and 3 seconds in each step. The DiffracPlus software of the diffractometer allowed initial processing of the diffraction pattern to differentiate the peaks corresponding to the austenite phase from the martensite phase. Quantification of the austenite fraction was performed using Topas R, analysis software based on the Rietveld method (Young, 1993).

For the CA6NM EB welds in the as-welded and PWHTed conditions, Vickers microhardness testing was performed using a Struers Duramin A300 machine equipped with an automated x-y stage and a fully automated testing cycle (i.e. stage movement, loading, focusing, and measurement). Specifically, Vickers microhardness measurements were carried

out on transverse sections of the weldments (i.e. perpendicular to the welding direction) at an interval of 0.3 mm with a load of 500 g for a dwell period of 3 seconds. The Vickers microhardness testing was performed incrementally over the entire FZ and HAZ area of the welds, with a minimum test point separation distance of at least three times the diagonal measurement of the indent. The results were then graphically plotted in Matlab to generate a two-dimensional (2D) Vickers microhardness map from the collection of 19 hardness distribution profiles that were evenly spaced over the 60 mm thick weld cross section. In this way, the microhardness changes over the entire surface of the EB welds could be visualized.

3.4 Results and discussions

3.4.1 Temperature evolution

The typical temperature evolution during the EB welding cycle is illustrated in Figure 3-5a, for two locations on the weld coupon. For the application of the EBZHT to preheat the CA6NM before welding, it was ascertained that three oscillation passes with a defocused electron beam were needed to stabilize the temperature in the range of 100-170°C, the preheat range recommended by (Handbook, 2004). As shown in Figure 3-5a, during welding, the linear heat input of 94.5 J·mm-1 resulted in a sharp increase in the temperature on approach of the EB heat source at locations 1 and 3, which corresponded approximately to the HAZ closest to the BM (i.e. HAZ5 as described later) on the top surface of the EB weldment. Upon passing of the EB heat source beyond locations 1 and 3, the temperature decreased rapidly at first and then at a decreasing rate. In due consideration of the symmetry conditions existing at locations 1 and 3, the matching thermal profiles give good assurance in the temperature data. Also, the thermal profiles measured at the other locations gave similar plots though the peak temperature was lower (~500°C), which is reasonable considering their location at the bottom surface of the EB weldment.

It is noteworthy that in the absence of preheating microfissures at the root and centerline cracks at the mid-thickness were observed in the FZ of the EB welds in CA6NM (Sarafan et al., 2013), as illustrated in Figure 3-5b and c. In general, cracking in welds is

dependent on three main factors: hydrogen, stress and microstructure. During autogenous EB welding in a vacuum environment, the risk of hydrogen entrapment is eliminated. However, the thermal stresses in EB welding are high due to the rapid heating and cooling rates, as well as the low heat input. This combined with a susceptible microstructure due to, for instance a steel chemistry with higher levels of carbon and/or high cooling rates (from a low heat input, a thick gage section and no preheating) can explain the occurrence of the root and centreline cracks in the FZ of the EB welds in CA6NM. In particular, Arata (Arata et al., 1972) categorized the microfissures at the root as horizontal cracks and attributed their occurrence to solidification phenomenon. In contrast, the centerline cracks, referred to as vertical cracks (Arata et al., 1972), were associated to the thermal stresses and microstructural transformations (i.e. higher hardness of the FZ) in the EB weldments. It is noteworthy that with increasing gage thickness, the self-restraint capability and inherent rigidity of the material increase (Srivastava et al., 2010). Arata (Arata et al., 1972) thus concluded that the risk of vertical cracks is greater when the hardness exceeds 600 HV in a 20 mm thick section.

Consequently with increasing gage thickness, this increasing tendency of crack formation may not be preventable even at a lower FZ hardness. Hence, for a given material chemistry and gage thickness, the application of preheating is naturally used to prevent cracking by reducing the cooling rate, which in turn reduces the shrinkage stresses. Previously Chen considered EBZHT for PWHT in a low alloy ultra-high strength 30CrMnSiNi2A steel (Chen et al., 2002). In the present work, EBZHT, a relatively new procedure that can be conducted in-situ with the EB welding system, was developed for preheating the CA6NM and was demonstrated to be effective in producing a crack free weld bead, as reported in our previous work (Sarafan et al.,2013) and illustrated in Figure 3-5d. This development and demonstration of the EBZHT for preheating CA6NM may enable further savings in energy and time for hydroelectric turbine manufacturing using EB welding.
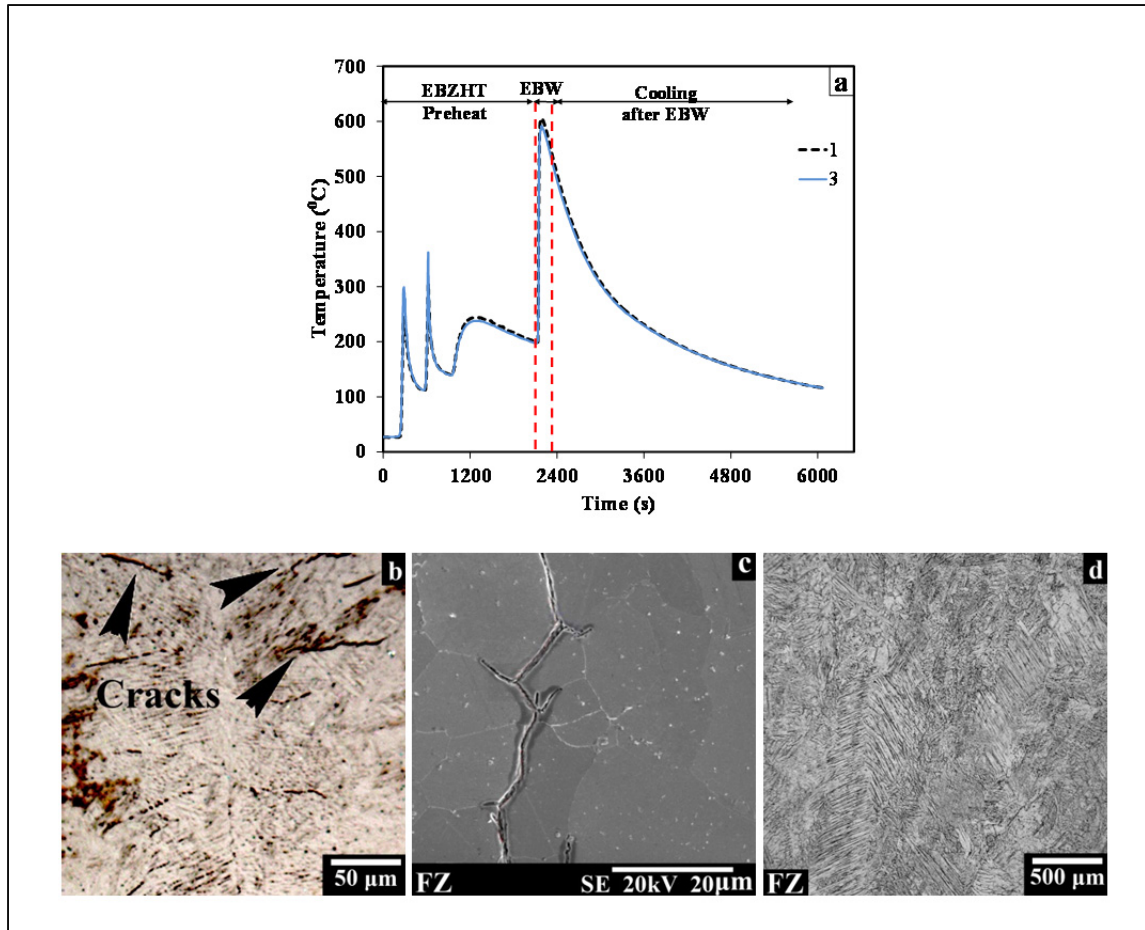
Figure 3-5 (a) Typical thermal cycle showing the temperature evolution during preheating by EBZHT and subsequent EB welding and cooling of the CA6NM (b) horizontal and (c) vertical cracks occurring in the FZ of CA6NM welds in the absence of preheating, and (d) crack free

3.4.2   Microstructural and hardness evolution of as-welded CA6NM

In the as-welded condition, a fully penetrated EB weldment in CA6NM consisted of several distinct regions, as illustrated in Figure 3-6a and b. Specifically, the BM microstructure of the as-received CA6NM in the normalized and tempered condition consisted predominately of tempered martensite laths, as shown in Figure 3-6b, as well as Figure 3-6c. Analysis of the other microstructural constituents using image analysis with optical microscopy and XRD indicated that up to 5 vol. % delta ferrite and 6.9 vol. % retained austenite were also present in the BM. By contrast, within the FZ (Figure 3-6d-f), heating to the melting temperature of CA6NM (~1500°C) followed by re-solidification

resulted in a microstructure consisting of oriented dendritic columnar grains that were predominately martensite (re-transformed). In addition, selective etching revealed the presence of fine δ-ferrite (4.7 vol. %) in the interdendritic regions, as illustrated in Figure 3-6e. Also, the FZ of the EB welds contained 5.6 vol. % of retained austenite, which most likely was present between the martensitic laths (Song et al., 2010).

Due to the varying thermal conditions experienced across the weldment, between the FZ and BM, different HAZs are present (Figure 3-6g-k). HAZ1, lying immediately adjacent to the FZ, is often referred to as the partially melted zone (PMZ), since in this region incipient melting of the nucleated delta ferrite formed on heating (Figure 3-6l) occurs. For the EB weldments in CA6NM, HAZ1 was impossible to distinguish as evidenced by its absence in Figure 3-6b. This finding is analogous to that previously reported in the literature for flux-cored arc welding (FCAW) (Thibault, 2009) and GTAW (Carrouge, 2004) of martensitic stainless steels. It is noteworthy that HAZ by definition usually refers to areas in the weldment where only solid phase transformations occur and, in theory, precludes the PMZ or HAZ1, which involves heating into the L+δ region (Figure 3-6l). The remaining different HAZs (Figure 3-6g-k) that were distinguishable in EB welded CA6NM could be categorized according to the maximum temperatures experienced during welding: (1) low temperature HAZs (HAZ4 and HAZ5) and (2) high temperature HAZs (HAZ2 and HAZ3).

Specifically, the four different HAZs had microstructures (Figure 3-6g-k) corresponding to the transformation of the tempered martensitic structure of the as-received CA6NM, which could be explained through the equilibrium ternary Fe-Cr-Ni phase diagram (Folkhard et Rabensteiner, 1988), as given in Figure 3-6l. The microhardness variation in these different regions (Figure 3-6m) can also aid in the identification of the different HAZs and their relative location from the weld centerline. Hence, to understand the evolution in the microstructure and the resulting microhardness in the weldment, it is important to consider the thermal history in the different zones in relation to the critical transformation temperatures of CA6NM. In particular, the thermal conditions during EB welding encompassed temperatures up to the melting point of ~1500°C (Handbook, 2004) in the

vicinity of the FZ to a temperature in the BM where no significant phase transformation occurred.

Immediately adjacent to the BM, HAZ5 is often referred to as the low temperature dual-phase ($\alpha'+\gamma$) region, as the local temperatures on heating surpass the critical temperature for the transformation of $\alpha' \rightarrow \alpha'+\gamma$ (i.e. A_{e1} in the equilibrium phase diagram given in Figure 3-6l). In particular, the peak temperature recorded at locations 1 and 3 that corresponded roughly to the BM/HAZ5 interface was 600°C, as revealed in Figure 3-5a. As such, during the heating cycle of EB welding, the microstructure of the CA6NM BM, which is predominately tempered martensite with residual quantities of delta ferrite and retained austenite, partially transforms in HAZ5 to austenite (often referred to as reversed austenite). Cooling after EB welding then results in the reverse transformation of austenite to martensite. The occurrence of re-transformed martensite, often referred to as untempered martensite, so as to differentiate against the tempered martensite condition of the BM, would result in an increase in hardness. The austenite formed on heating in HAZ5 may also remain stable on cooling, which would tend to decrease the hardness. Previous work on multi-pass FCAW of 13%Cr–4%Ni martensitic stainless steel has reported (Thibault, 2009) that both stable austenite and untempered martensite sub-zones are possible in HAZ5.

The occurrence of these sub-zones is manifested as an initial hardness decrease in HAZ5, followed by a hardness increase, relative to the BM (Carrouge, 2004; Thibault, 2009). In the present work, examination of the microhardness profile of the EB weld in CA6NM indicates a similar tendency; the microhardness decreases from the BM average value of 289±4 HV to a minimum of 268 HV near the onset of HAZ5 and then progressively increases towards HAZ4. Notwithstanding the discernible hardness changes, the microstructural characteristics of HAZ5 (Figure 3-6k) were overall not distinguishably different from the BM under optical and scanning electron microscopy. It is noteworthy, however, that by over-etching the sample, the microstructure of HAZ5 could be seen (under optical microscopy) to change progressively from a dark etched region next to the BM to a light etched region next to HAZ4 (Sarafan et al., 2013). This agrees well with the analysis of the transformations on heating and cooling. That is, transitioning from the BM to HAZ4, the

temperature increases in HAZ5 and a greater quantity of austenite progressively forms on heating, which on cooling then transforms to untempered martensite that is brighter in appearance relative to the tempered martensite when etched and viewed under optical microscopy (Figure 3-6b).

In HAZ4, referred to as the single phase austenite region, the temperatures surpass the critical temperature for complete transformation of martensite to austenite ($\alpha'+\gamma\rightarrow\gamma$), as represented by A_{e3} in the equilibrium phase diagram shown in Figure 3-6l. However the progressive rise in hardness in HAZ4 (from 350 HV to 425 HV) suggests that the microstructure of HAZ4 (Figure 3-6i and j) does not completely transform from martensite to austenite on heating, especially in the region adjacent to HAZ5, which may be related to insufficient time (kinetics) due to the short exposure time during EB welding. With this perspective, it is deemed that in HAZ4 the tempered martensite structure of the BM transforms increasingly to austenite and upon cooling re-transforms to martensite (untempered). Considering the quasi-binary equilibrium diagram for Fe-Cr-Ni-0.053C (Figure 3-7), the dissolution of $M_{23}C_6$ carbides also occurs concomitantly in HAZ4 with the austenite to martensite phase transformation. In comparison with HAZ5, the microstructural difference between HAZ4 (Figure 3-6j) and the BM (Figure 3-6c) was more evident (Figure 3-6a-b). Specifically, the weaker etching response of HAZ4 compared to HAZ5 and the BM gives a good premise for the concomitant occurrence of carbide dissolution in HAZ4. Previously for multi-pass FCAW of 13%Cr–4%Ni martensitic stainless steel, it was reported that in HAZ4 both carbide dissolution and grain growth are possible (Thibault, 2009).
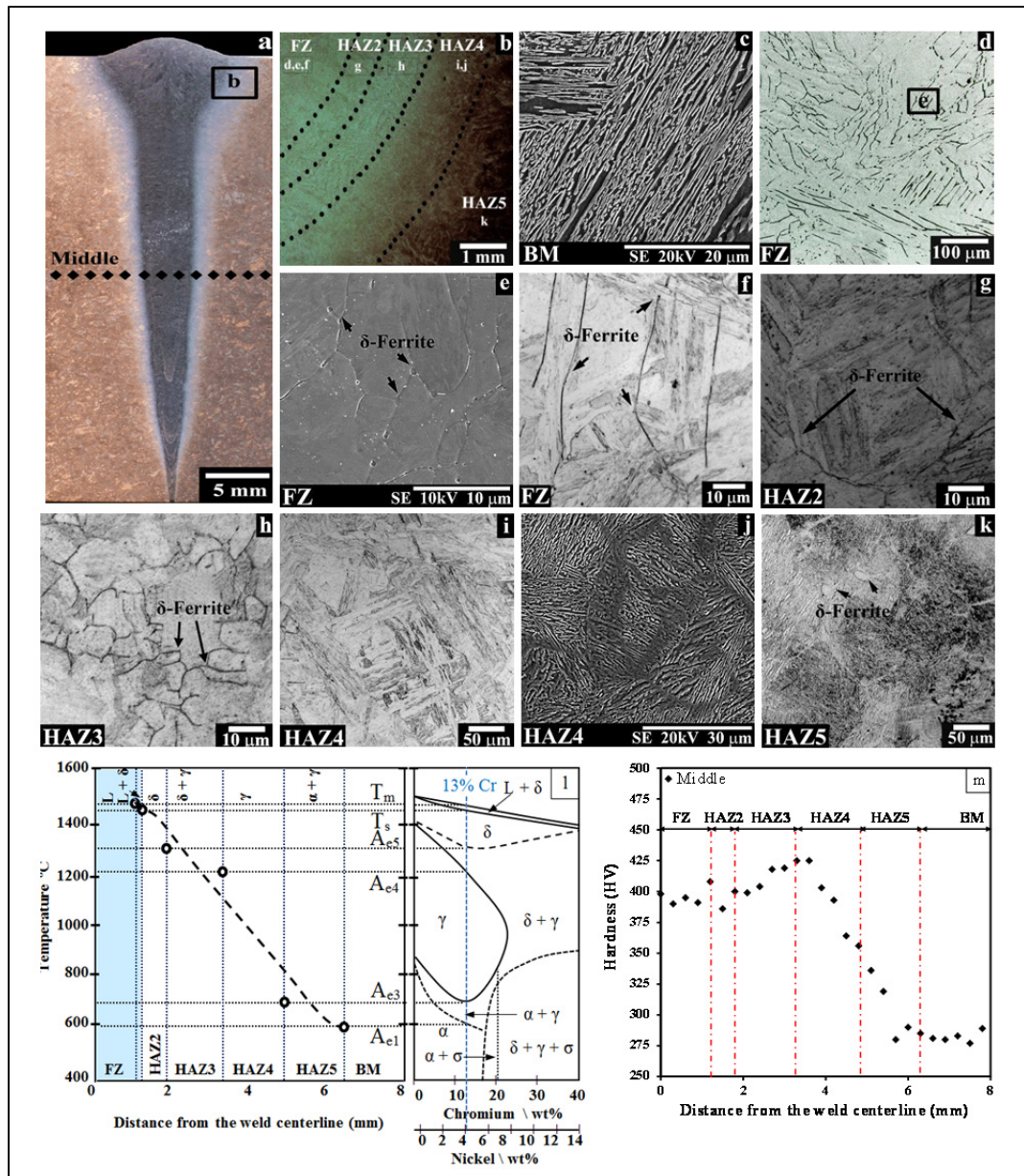
Figure 3-6 As-welded CA6NM: (a) macrostructure of the transverse weld cross-section (OMI) (b) HAZ sub-regions adjacent to the FZ with the absence of HAZ1 (OMI), (c) SEI of BM microstructure (OMI given in Figure 3-1b), (d-f) FZ microstructure selectively etched for delta ferrite (OMI and SEI), (g) HAZ2 microstructure (OMI), (h) HAZ3 microstructure (OMI), (i-j) HAZ4 microstructure (OMI and SEI), (k) HAZ5 microstructure (OMI), (l) schematic diagram showing the microstructural changes in the low and high temperature HAZs in relation to the Fe-Cr-Ni equilibrium phase diagram (Folkhard et Rabensteiner, 1988), and (m) microhardness profile at the mid-thickness
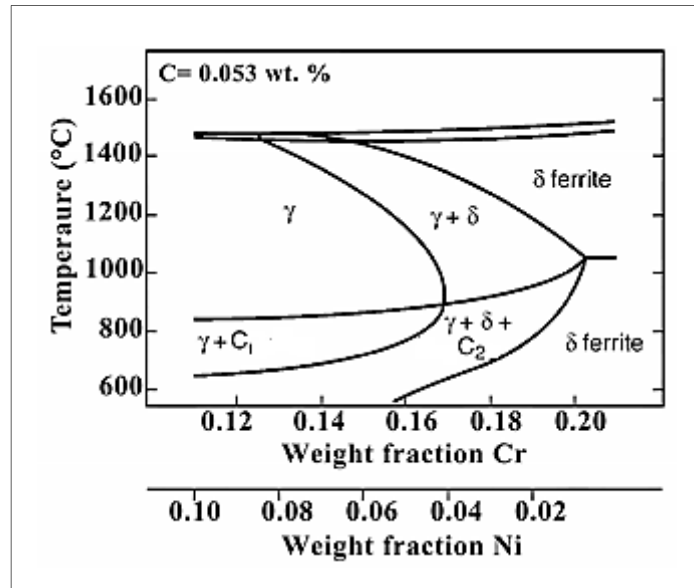
Figure 3-7 Calculated quasi-binary
equilibrium phase diagram for Fe-Cr-Ni-
0.053C (Lippold et Kotecki, 2005) (C1 and
C2 are M23C6 and M7C3 carbides)

In the present work, though evidence for carbide dissolution is present, grain structural changes were not observed as the low heat input applied with the single pass EB welding process limited the breadth of the HAZ as well as the extent of grain growth. At the onset of HAZ3, referred to as the high temperature dual phase ($\gamma+\delta$) region, the BM has been heated to temperatures above that required to start the transformation of austenite to delta ferrite ($\gamma \rightarrow \gamma+\delta$), as characterized by A_{e4} in the equilibrium phase diagram shown in Figure 3-6l. As such, the nucleation of delta ferrite on heating during EB welding occurs at the grain boundaries and on cooling evidence of its formation is retained at the prior-austenitic grain boundaries (Figure 3-6h). The presence of retained delta ferrite can be explained by the partitioning of ferrite stabilising elements and the fast cooling rate after EB welding (Bilmes et al., 2001). In particular, EDX microanalyses of the martensitic matrix and the delta ferrite within HAZ3 indicated that the latter was significantly enriched with ferrite-stabilizer elements such as Cr and Mo, but depleted in Ni (austenite-stabilizer), as shown in Table 3-1. The partitioning of these ferrite stabilising elements to delta ferrite on heating and their inability to diffuse back into the matrix during rapid cooling then results in the retention of

delta ferrite at room temperature in HAZ3. In fact, work on FCAW of 13%Cr–4%Ni martensitic stainless steel also indicated the presence of delta ferrite stringers around the austenite grains (Thibault et al., 2009). Inevitably, the formation of delta ferrite lowers the hardness, and, at the onset of HAZ3, the hardness was observed to decrease (Figure 3-6m). Specifically the microhardness progressively decreased from a value of 425 HV near HAZ4 to 400 HV near HAZ2. This finding is in agreement with the drop in hardness (15 HV) identified in the work of Enerhaug et al. (Enerhaug et al., 2001) on super martensitic stainless steel weldments assembled by GMAW.

Table 3-1 EDX microanalysis (wt. %) of phases in EB welded CA6NM

Phase	Cr	Ni	Mo
Ferrite	16.59±0.24	1.19±0.2	0.59±0.35
Martensitic Matrix	13.25±0.29	3.83±0.32	1.19±0.27

In HAZ2, referred to as the single phase delta ferrite region, the temperature is locally above that required to completely transform austenite to delta ferrite ($\gamma+\delta\rightarrow\delta$), which at equilibrium is represented by A_{e5} as shown in Figure 3-6l. At these elevated temperatures, significant growth of the delta ferrite grains occurs during heating. Upon cooling, re-transformation of the delta ferrite to austenite (and subsequently to martensite) occurs such that the room temperature microstructure in HAZ2 consists of a coarse grained (untempered) martensitic structure (Figure 3-6g). It is noteworthy that fine delta ferrite stringers are also present at the prior-austenite grain boundaries; most likely due to the locally higher concentration of ferrite stabilizing elements that suppresses transformation during rapid cooling. These microstructural observations in HAZ2 for EB welded CA6NM are in agreement with previous work on FCAW (Thibault et al., 2009) and GMAW (Enerhaug et al., 2001) of martensitic stainless steels that indicated microstructural characteristics of coarse-grained re-transformed martensite with fine delta ferrite at the prior-austenite grain boundaries. In addition, as illustrated in Figure 3-6m, the microhardness values in HAZ2 ranged between 385-410 HV. Previously, work on FCAW (Thibault et al., 2009) and GMAW (Enerhaug et al., 2001) of martensitic stainless steels revealed average

microhardness values in HAZ2 of ~350 HV and 265 HV, respectively. The higher hardness for the EB weldments is most likely due to the higher carbon content of the martensitic stainless steel (Table 3-2). Generally the carbon content is considered as the principal factor determining the hardness of the martensitic structure, since it controls the lattice dilation during transformation to a slipped or twinned product (ASME Boiler and Pressure Vessel Code, 2007), while substitutional elements in the chemical composition play a secondary role in resolving the absolute hardness value. It is noteworthy that the narrow breadth of HAZ2 in each weld limits the number of hardness measurements (i.e. 2-3 data points) and renders the assessments in this area to be less conclusive statistically, as compared to the other HAZs.

Table 3-2 Comparison of HAZ2 characteristics in EB welded CA6NM with reported findings for martensitic stainless steels

	GMAW (Enerhaug et al., 2001)	FCAW (Thibault et al., 2009)	EBW
Carbon Content (%)	0.011	0.023	0.056
HAZ2 Hardness (HV)	263-267	344-362	380-410
HAZ2 Breadth (mm)	0.5	0.4	0.4

3.4.3   Microstructural and hardness evolution of PWHTed CA6NM

Generally for martensitic stainless steels, PWHT is realized to temper the re-transformed martensite, so as to enable a decrease in the hardness, and thereby an increase in the toughness, as well as a decrease in the residual stresses (Srivastava et al., 2010). For CA6NM, a PWHT at 600°C for 9.5 hours is recommended in (Song et al., 2010b) to meet the mechanical property requirements for the gage thickness welded in this work (60 mm) and service conditions of hydroelectric turbine materials. As illustrated in Figure 3-8, the application of this PWHT at 600°C was observed to homogenize the microhardness and microstructural gradients determined for the as-welded condition. Specifically, examining the 2D hardness map of the entire surface of the CA6NM weldment in the as-welded condition (Figure 3-8a) reveals a definite correspondence to the macrostructure of the

transverse weld cross-section given in Figure 3-6a. As discussed above, six different microstructural zones (BM, FZ, HAZ2, HAZ3, HAZ4 and HAZ5) are discernible in the macrograph of the EB weldment in the as-welded condition. Through superimposing of this macrograph (Figure 3-6a) on the 2D microhardness map in the as-welded condition (Figure 3-8a), five different microstructural zones, namely the BM, FZ, HAZ3, HAZ4 and HAZ5, can be clearly related to the different discretized hardness regions, as revealed in Figure 3-8a. It is noteworthy that HAZ2 could not be differentiated in the 2D microhardness map due its limited size and similarity in hardness with the FZ. Discriminating for the different HAZs in the 2D microhardness map (as well as in the macrograph) also became progressively more difficult towards the root of the weld due to the reduced breadth of each area. Overall, the 2D microhardness map indicated good symmetry in the hardness distribution on either side of the weld centerline, though some variance could be noted especially towards the weld crown, which may be due to minor tilting of the electron beam gun. Also noticeable was the lower hardness in the central region of the FZ, spanning from a location just above the beam focus position to the weld crown. In particular, the hardness towards the narrower root area of the FZ (408 HV) was higher than that towards the wider crown area (390 HV), especially near the centerline. This is reasonably related to the thermal gradients and cooling rate variations in the EB weldment (Arata et al., 1976; Song et al., 2010a). Also Arata (Arata et al., 1973) reported that the hardness could be roughly 100 HV higher in the root area of the FZ of different ferrous alloys (i.e. SM41, HT60 and HT80) as compared to the underbead below the top crown surface.

In contrast, the 2D microhardness map for CA6NM in the PWHTed condition reveals three different regions, as illustrated in Figure 3-8b. In particular, the BM region, initially at 289±4 HV in the as-welded condition was determined to have a hardness of 270±5 HV in the PWHTed condition. The region encompassing the four HAZs (i.e. HAZ2, HAZ3, HAZ4 and HAZ5) as well as the adjacent FZ periphery exhibited hardness values in the range of 270 HV to 300 HV in the PWHTed CA6NM. In the central region of the FZ, the hardness was the highest, ranging from 330 HV to 340 HV after PWHT.
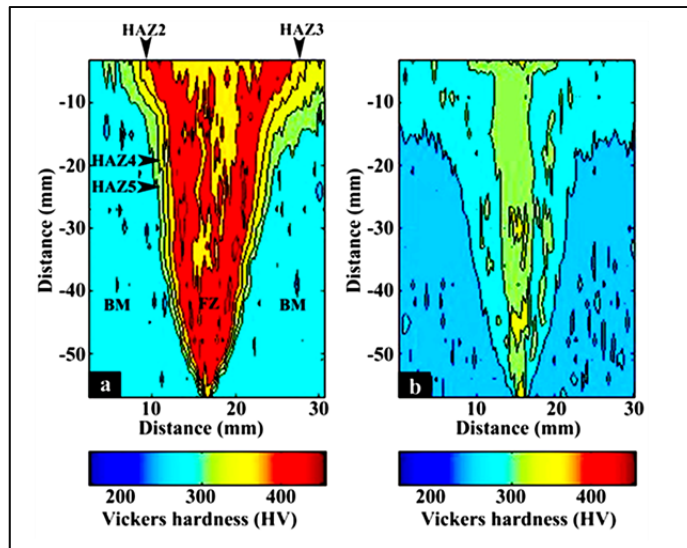
Figure 3-8 2D Microhardness map of fully
penetrated CA6NM welds in the (a) as-welded and
(b) PWHTed conditions

This evolution in hardness from the BM to the FZ can be examined closely by considering a profile across the mid-section of the EB weldment in the PWHTed condition, as illustrated in Figure 3-9. For the BM region, the drop in hardness (~20 HV) due to PWHT can be reasoned by considering the transformations that would occur at 600°C for the microstructural constituents in the as-received CA6NM that was in the normalized and tempered condition. Specifically, on heating the predominantly martensitic microstructure of CA6NM would begin to partially transform to austenite during prolonged holding for 9 hours at 600°C, just above the critical temperature for the transformation of martensite to austenite ($\alpha' \rightarrow \alpha' + \gamma$), as illustrated in equilibrium phase diagram in Figure 3-6l. This reversed austenite can stabilize during tempering just above this transformation temperature and be retained during cooling to room temperature through a mechanism described as anomalous phase transformation (Arata et al., 1976; Song et al., 2010a). In particular, using transmission electron microscopy, Song et al. (Song et al., 2010b) determined that the precipitation of $M_{23}C_6$ carbides in the martensite laths during tempering just above the $\alpha' \rightarrow \alpha' + \gamma$ transformation temperature leads to the adjoining regions being enriched in Ni which, in turn, encourages austenite nucleation. This reversed austenite that forms at the martensite lath boundaries does not transform on cooling and co-exists in a cube-cube orientation

relationship with the $M_{23}C_6$ carbides and a Kurdjumov-Sachs relationship with the martensite (Song et al., 2010a). In the present work, characterization of the BM using XRD (Figure 3-10) indicated that the fraction of retained austenite increases after PWHT, as given in Table 3-3. Notwithstanding this microstructural change, the delta ferrite content in the BM remained similar after PWHT. As retained austenite is softer than martensite, the higher retained austenite content in the PWHTed BM then reasonably explains the observed reduction in hardness.
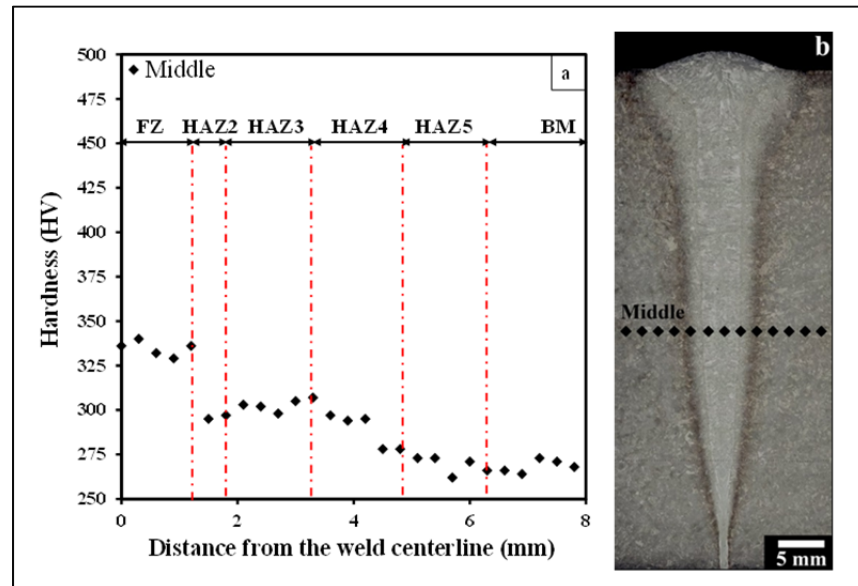
Figure 3-9 PWHTed CA6NM: (a) microhardness profile at mid-thickness and (b) macrostructure of transverse cross-section
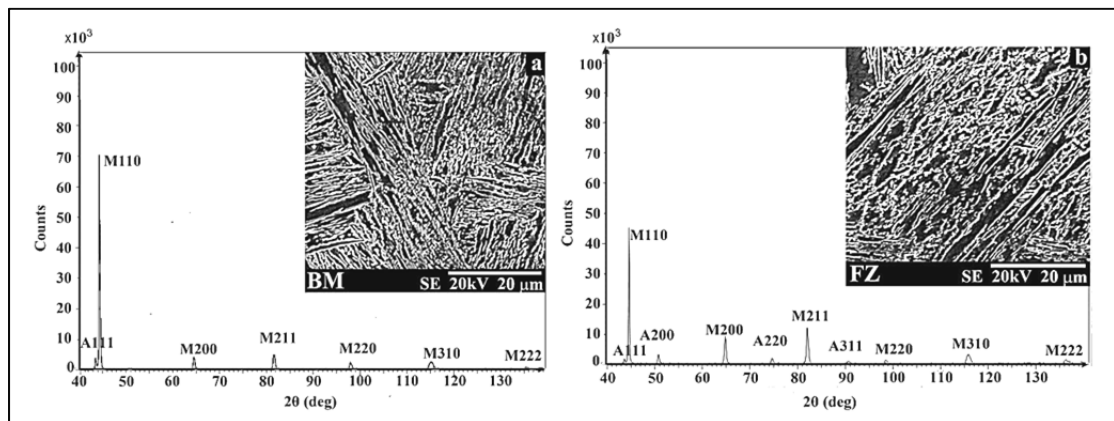
Figure 3-10 XRD pattern for the PWHTed microstructure in the (a) BM and (b) FZ

Table 3-3 XRD and image analysis results in as-welded and PWHTed
conditions CA6NM

Microstructural Features	As-Received	As-welded	PWHTed
Delta ferrite in FZ (%)	N/A	4.7	4.7
Retained austenite in FZ (%)	N/A	5.6	10.2
Delta Ferrite in BM (%)	5	N/A	5.1
Retained austenite in BM (%)	6.9	N/A	22.4

Adjacent to the BM, the low temperature HAZ that encompasses HAZ4 and HAZ5 was noted to consist of a mixture of tempered martensite and re-transformed (untempered) martensite, with remnant quantities of retained austenite and delta ferrite, upon cooling after welding. PWHT of this microstructure at 600°C would lead to the following transformations:

(1) For the remnant tempered martensite that did not undergo transformation on heating during welding, the PWHT results in its partial transformation to austenite, which upon cooling can be retained as described above. Hence PWHT of the tempered martensite fraction would tend to decrease the hardness due to the increased likelihood of reversed austenite.

(2) For the tempered martensite that undergoes transformation on heating during welding and re-transforms to martensite on cooling, the PWHT would soften this untempered martensitic fraction. As the PWHT involves a single tempering cycle as compared to the two tempering cycles imparted to the as-received CA6NM, it is reasonable that the extent of softening of the untempered martensite would be lower.

Hence, initially on approaching HAZ5 from the BM, the fraction of untempered martensite would remain relatively small and the formation of reverse austenite would then manifest as a hardness reduction (minimum value of 262 HV), as illustrated in Figure 3-9a. Subsequently the progressive increase in temperature within HAZ5 and HAZ4 on heating during welding rapidly increased the untempered martensite fraction and, in turn, the hardness (Figure 3-6m). PWHT then softened the untempered martensite but the trend of

increasing hardness remained, such that the hardness near the HAZ4/HAZ3 interface was ~307 HV, as shown in Figure 3-9a. Microscopic examination of HAZ4 and HAZ5 after PWHT (Figure 3-10) indicated structural features with marked similarity to the CA6NM BM (PWHTed).

For the high temperature HAZ (i.e. HAZ2 and HAZ3), the formation of delta ferrite on heating and its subsequent transformation to austenite (and then untempered martensite) or retention along the prior-austenite grain boundaries on cooling was noted above (Figure 3-6g-h). The effect of PWHT on this microstructure resulted in a softening of the untempered martensite that manifested as a hardness drop (~100 HV) relative to the as-welded condition. It is noteworthy that the decrease in hardness observed between HAZ3 and the onset of HAZ2, due to the retention of delta ferrite at the prior-austenite grain boundaries in the as-welded condition (Figure 3-6m), remains in the PWHTed condition (Figure 3-9a), though the hardness difference is lower for the latter. The microstructure in HAZ2 and HAZ3 in the PWHTed condition (Figure 3-11) closely resembled that observed in the as-welded condition (Figure 3-6g-h).

The occurrence of melting and re-solidification in the FZ resulted in a microstructure consisting of re-transformed (untempered) martensite with 4.7 vol. % of delta ferrite and 5.6 vol. % retained austenite in the as-welded condition, as mentioned above. Naturally, PWHT rendered softening of the untempered martensite in the FZ. Also, after PWHT, though the fraction of delta ferrite remained constant, the amount of retained austenite nearly doubled (10.2 vol. %). Tempering of the martensite along with the higher retained austenite fraction was observed to decrease the FZ hardness by 100 HV in the PWHTed condition relative to the as-welded condition. It is also noteworthy that in the PWHTed condition the central region of the FZ was about 15-30 HV higher than adjoining periphery. In addition, the hardness was greater in the central root area of the FZ (368 HV) relative to the underbead area below the crown (342 HV). This may be a residual effect from the hardness variation in the as-welded condition that also exhibited a difference in hardness between the crown and root areas.
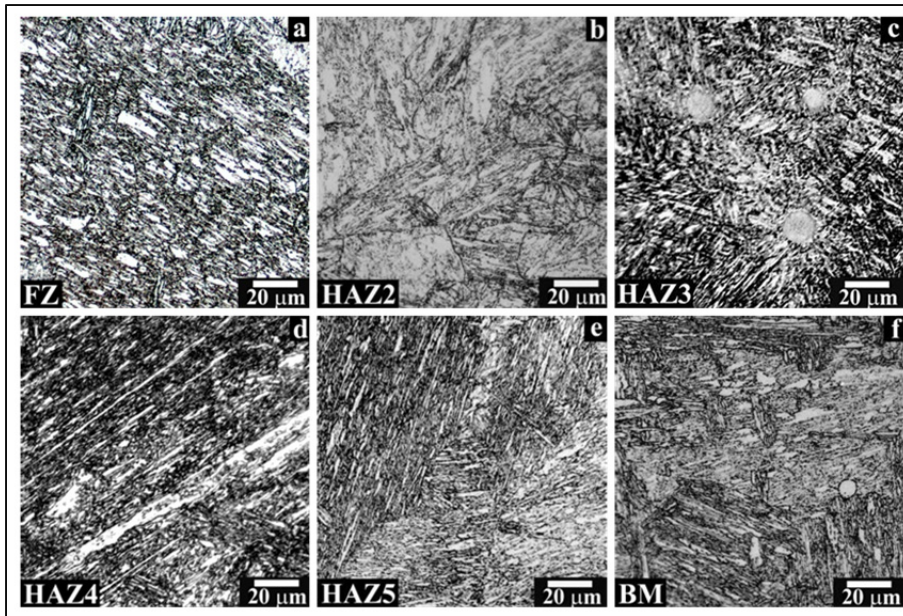
Figure 3-11 Microstructure in PWHT condition: (a) FZ, (b) HAZ2,
(c) HAZ3, (d) HAZ4, (e) HAZ5 and (f) BM

3.5   Conclusions

Based on the results of the present research on electron beam (EB) welding of a 13%Cr–4%Ni martensitic stainless steel (CA6NM), the following conclusions can be drawn:

- Autogenous EB welding can be successfully applied to penetrate 60 mm thick CA6NM.

- To prevent cracking of the CA6NM during EB welding, preheating in the range of 100-170°C is necessary. An electron beam zonal heat treatment (EBZHT) process can suitably preheat the CA6NM in-situ the EB welding system. The electron beam zonal heat treatment process involved oscillating a defocused beam in a circular path along the path of the weld seam. Real-time acquisition of the thermal cycles during the EBZHT process indicated that after 3 sequential passes of the oscillated and defocused beam the preheat temperature range required for welding CA6NM could be reached.

- The single pass autogenous EB welds exhibited distinct regions that comprised the CA6NM base metal, fusion zone and an elaborate heat affected zone (HAZ) within

which four different sub-regions were distinguishable. Each region in the EB weldment could be interpreted by considering the microstructural observations in relation to the ternary Fe–Cr–Ni phase diagram and an illustrative examination of the local thermal history transpiring during EB welding.

- In general, for the as-welded condition, the hardness profiles revealed maximum (425 HV) and minimum (268 HV) values in the low temperature HAZs, namely HAZ4 and HAZ5, respectively. A reduction in hardness was seen in the high temperature HAZs (HAZ2 and HAZ3) that was attributed to the formation of delta ferrite on heating. Specifically, in HAZ3 the hardness decreased from 425 HV near the HAZ4 to 400 HV adjacent to HAZ2; the microhardness values in HAZ2 ranged between 385-410 HV. EDX analysis of HAZ3 indicated that the delta ferrite formed on heating is retained due to the partitioning of ferrite stabilizing elements, namely Cr and Mo, during transformation. Specifically the delta ferrite was enriched in Cr and Mo and depleted in Ni.

- The application of a post-weld heat treatment (PWHT) was observed to generate a relatively uniform microstructure with minimum and maximum hardness values in the weldment of 270±5 HV and 346±13 HV, respectively in the base metal and the fusion zone. The reduction in the hardness in the base metal was attributed to the stabilization of austenite during PWHT that resulted in a relatively high volume fraction of retained austenite (~22 vol. %) in the microstructure. The hardness in the fusion zone that varied from 390-408 HV in the as-welded condition decreased after PWHT due to tempering of the re-transformed martensite as well as the higher (double) fraction of retained austenite.

3.6   Acknowledgments

3.7 References

Arata, Y, Matsuda, F, Nakata, K. 1972. « Quench Hardening and Cracking in Electron beam weld metal of carbon and low alloy hardenable steels ». *Transactions of JWRI*, vol. 1, nº 1, p. 39-51.

Arata, Y, Tomie, M, Kohyama, A. 1976. « 100KW class electron beam welding technology (report III): characteristics of deep penetration bead and its analysis ». *Transactions of JWRI*, vol. 5, nº 1, p. 11-18.

Arata, Y; Tomie, M; Terai, K; Nagai, H; Hattori, T. 1973. « Shape decision of high energy density beam ». *Transactions of JWRI*, vol. 2, nº 2, p. 130-146.

ASME Boiler and Pressure Vessel Code. 2007. Section VIII, Division 1, « *Rules for construction of pressure vessels* ». ASME, New York.

ASTM-A487/A487-93. 2012. « *Standard specification for castings suitable for pressure service, corrosion resistant, for general application* ». West Conshohocken, PA.

ASTM-A743/A743M. 2006. « *Standard specification for castings, iron-chromium, iron-chromium-nickel* ». West Conshohocken, PA.

Bakunov, AS; Muzhitskii, VF. 2004. « The control of the magnetisation of components prior to welding operations ». *Welding International*, vol. 18, nº 6, p. 498-500.

Bilmes, PD; Solari, M; Llorente, CL. 2001. « Characteristics and effects of austenite resulting from tempering of 13Cr–NiMo martensitic steel weld metals ». *Materials Characterization*, vol. 46, nº 4, p. 285-296.

Carrouge, D; Bhadeshia, HKDH; Woollin, P. 2004. « Effect of δ-ferrite on impact properties of supermartensitic stainless steel heat affected zones ». *Science and Technology of Welding & Joining*, vol. 9, nº 5, p. 377-389.

Chen, FR, Huo, LX, Zhang, YF, Zhang, L, Liu, FJ, Chen, G. 2002. « Effects of electron beam local post-weld heat-treatment on the microstructure and properties of

30CrMnSiNi2A steel welded joints ». *Journal of Materials Processing Technology*, vol. 129, nº 1, p. 412-417.

Côté, M. 2007. « *Étude des cinétiques de transformation de phase d'un acier inoxydable martensitique 13%Cr-4%Ni* ». École de Technologie Supérieure.

Enerhaug, J; Steinsmo, UM. 2001. « Factors Affecting Initiation of Pitting Corrosion in Super Martensitic Stainless Steel Weldments ». *Science and Technology of Welding & Joining*, vol. 6, nº 5, p. 330-338.

Folkhard, E, Günther, R. 1988. « *Welding Metallurgy of Stainless Steels* ». *Springer*.

Handbook. 2004. « *Steel castings handbook supplement 8: high alloys data sheets, corrosion series* ». Steel Founders' Society of America, USA.

Handbook, Metals. 1993. « *Welding, brazing and soldering* ». *ASM International*, Materials Park, vol. 6, p. 117-118, USA.

Kumar, A. 2011. « *IPCC special report on renewable energy sources and climate change mitigation* ». United Kingdom and New York, NY, USA.

Lippold, JC, Kotecki, DJ. 2005. « Welding metallurgy and weldability of stainless steels ». ISBN 0-471-47379-0, Wiley-VCH.

Meleka, AH. 1971. « *Electron beam welding: principles and practice* ». McGraw-Hill, London.

Sarafan, S, Wanjara, P, Champliaud, H, Mathieu, L, Lanteigne, J. 2013. « Characteristics of electron beam welded CA6NM ». Proceeding of Material Science and Technology, p. 720-732, Canada.

Schultz, Helmut. 1993. « *Electron beam welding* ». Woodhead Publishing.

Song, YY, Li, XY, Rong, LJ, Li, YY. 2010a. « Anomalous phase transformation from martensite to austenite in Fe-13%Cr-4%Ni-Mo martensitic stainless steel ». *Journal of Materials Science & Technology*, vol. 26, nº 9, p. 823-826.

Song, YY, Li, XY, Rong, LJ, Ping, DH, Yin, FX, Li., YY. 2010b. « Formation of the reversed austenite during intercritical tempering in a Fe–13%Cr–4%Ni–Mo martensitic stainless steel ». *Materials Letters*, vol. 64, nº 13, p. 1411-1414.

Srivastava, BK, Tewari, S, Prakash, J. 2010. « A Review on effect of preheating and/or post-weld heat treatmemt (PWHT) on mechanical behaviour of ferrous metals ». *International Journal of Engineering Science and Technology*, vol. 2, nº 4, p. 625-631.

Thibault, D, Bocher, P, Thomas, M, Gharghouri, M, Côté, M. 2010. « Residual stress characterization in low transformation temperature 13%Cr–4%Ni stainless steel weld by neutron diffraction and the contour method ». *Materials Science and Engineering: A*, vol. 527, nº 23, p. 6205-6210.

Thibault, D; Bocher, P; Thomas, M. 2009. « Residual stress and microstructure in welds of 13%Cr–4%Ni martensitic stainless steel ». *Journal of Materials Processing Technology*, vol. 209, nº 4, p. 2195-2202.

Thibault, D; Bocher, P; Thomas, M; Lanteigne, J; Hovington, P; Robichaud, P. 2011. « Reformed austenite transformation during fatigue crack propagation of 13%Cr–4%Ni stainless steel ». *Materials Science and Engineering: A*, vol. 528, nº 21, p. 6519-6526.

Wanjara, P, Jahazi, M. 2008. « Characterization of electron beam welded 17-4PH stainless steel ». *Canadian Metallurgical Quarterly*, vol. 47, nº 4, p. 413-435.

Young, RA. 1993. « *Introduction to the Rietveld method* ». The Rietveld Method, vol. 5, p. 1-38.

CHAPITRE 4

GLOBAL AND LOCAL CHARACTERISTICS OF AN AUTOGENOUS SINGLE PASS ELECTRON BEAM WELD IN THICK GAGE UNS S41500 STEEL

S. Sarafan [a], P. Wanjara [b], J. Gholipour [b] and H. Champliaud [a]

[a] École de technologie supérieure, Montréal, Québec, Canada H3C 1K3
[b] National Research Council Canada, Aerospace, Montréal, Québec, Canada H3T 2B2

4.1   Abstract

Electron beam welding of UNS S41500, a low carbon martensitic stainless steel utilized in hydroelectric turbine manufacturing, was investigated by applying a single pass autogenous process to penetrate a gage section thickness of 72 mm without preheating. In both the as-welded and post-weld heat treated conditions, the characteristics of the welds, including the evolution in microhardness and microstructure across the weldments, as well as the global and local tensile properties, were evaluated. In the as-welded condition, assessment of the microhardness and the associated microstructure across the welds led to the identification of six different regions, including the fusion zone, four heat affected zones and the base metal; each of these regions consisted of different phase constituents, such as tempered martensite, untempered martensite, delta ferrite and retained austenite. Post-weld heat treatment, undertaken to temper the untempered martensite in the as-welded microstructure, was effective in homogenizing the hardness across the weldment. The mechanical response of the welds, determined through tensile testing at room temperature with an automated non-contact three-dimensional deformation measurement system, indicated that the global tensile properties in both the as-welded and PWHTed conditions met the acceptance criteria stipulated for hydroelectric turbine applications in the ASME Section IX standard. Also, evaluation of the local tensile properties in the fusion and heat affected

64

zones of the as-welded samples allowed a more comprehensive understanding of the strength and ductility associated with the different microstructural features in the "composite" nature of the weldment. Fractographic analysis demonstrated dimpled features on the tensile fracture surfaces and failure was associated with debonding between the martensitic matrix and the secondary phases (such as delta ferrite and retained austenite) that resulted in the formation, growth and coalescence of voids into a macroscale crack.

Keywords: Electron beam welding, Wrought martensitic stainless steel UNS S41500, Post-weld heat treatment, Tensile properties, Digital image correlation, Microhardness.

NOMENCLATURE			
Ac_1	Start temperature of austenite formation on heating	HAZ	Heat-affected zone
Ac_3	Finish temperature of austenite formation on heating	HLAW	Hybrid-laser arc welding
Ac_4	Start temperature of delta ferrite formation on heating	HV	Vickers hardness number
Ac_5	Finish temperature of delta ferrite formation on heating	M_f	Martensite finish temperature
BM	Base metal	LSM	Laser scanning microscope
CCD	Charge-coupled device	PMZ	Partial melted zone
DIC	Digital image correlation	OM	Optical microscope
DBTT	Ductile-to-brittle transition temperature	PWHT	Post-weld heat treatment
EB	Electron beam	s	Seconds
EBW	Electron beam welding	SEI	Secondary electron imaging
%El.	Total percent elongation	SEM	Scanning electron microscope
FCAW	Flux-cored arc welding	UTS	Ultimate tensile strength
fps	Frames per second	XRD	X-ray diffraction
FZ	Fusion zone	YS	Yield strength
G	Gage length	α	Martensite
GTAW	Gas tungsten arc welding	δ	Delta ferrite
h	Hours	γ	Austenite

4.2   Introduction

Stainless steels (Fe-Cr-C ternary alloys) are typically categorized on the basis of their microstructures into five groups – ferritic, austenitic, martensitic, duplex (austenitic - ferritic) and precipitation hardening – and the selection of a specific grade depends on the particular properties required for the intended application. For instance, martensitic stainless steel grades are usually selected for applications where both wear resistance and corrosion properties are important. Specifically, the hardenability, tensile strength and ductility of martensitic stainless steels are strongly dependent on the carbon content and the resulting phase constituents of the microstructure that can be controlled by heat treatment. With increasing carbon content, the susceptibility of martensitic stainless steels to hydrogen induced and/or cold cracking as well as sensitization increases. As such, low carbon (less than 0.06%) martensitic stainless steel grades with additions of nickel and molybdenum, such as UNS S41500, have been designed for high strength and toughness, as well as good corrosion resistance (Gooch, 1995).

The microstructure of low carbon martensitic stainless steels consists predominantly of martensite laths with secondary phases such as retained austenite (up to 30 vol. %) and delta ferrite (up to 5 vol. %), the fraction of which depend on the carbon content, austenite and ferrite stabilizing elements, and heat treatment conditions (Bilmes et al., 2001; Carrouge et al., 2004; Enerhaug et al., 2001; Thibault et al., 2009; 2011). With increasing carbon content in low carbon martensitic stainless steels, the transformed martensite during cooling is harder, but concomitantly the extent of chromium carbide precipitation at the grain boundaries increases and results in a microstructure with a greater susceptibility to embrittlement (Kumar et al., 2013). For this reason, molybdenum, a ferrite stabilizer, is added to low carbon martensitic stainless steels to provide solid solution strengthening of the martensite phase, whilst improving both the general and localized corrosion resistance (Carrouge et al., 2004). However, as molybdenum is a strong ferrite stabilizing element, the austenite – ferrite balance in the alloy is reconstituted by the addition of nickel, an austenite stabilizer. The addition of nickel in the low carbon martensitic stainless steels reduces the extent of delta ferrite formation at the grain boundaries, which in turn improves the impact

toughness of the martensitic microstructure (Carrouge et al., 2004). For any given composition, the mechanical properties (strength, toughness, ductility) of low carbon martensitic stainless steels can be tailored by applying a suitable heat treatment. For instance, tempering of low carbon martensitic stainless steels close to the Ac1 gives superior toughness due to the formation of finely distributed reversed austenite along the martensite interlath boundaries (Song et al., 2010; Wang et al., 2010).

Wrought grades of low carbon martensitic stainless steel can be manufactured using various steelmaking processes, commencing from casting to successive operations of hot and/or cold working with intermittent heat treatment stages to attain different product forms for a broad array of engineering applications. Moreover, as low carbon martensitic stainless steel grades have good weldability, joining technologies can be integrated into the manufacturing process to diversify applications in numerous fields. Accordingly, research on the weldability of normalized and tempered low carbon martensitic stainless steels, such as grade 13%Cr–4%Ni, has been the focus of several investigators working on intended applications in the oil and gas, hydraulic turbines and power generation industries, for instance. To date, this weldability research on low carbon martensitic stainless steel has centred on conventional (manual) arc welding processes, such as GTAW with solid wires or flux-cored wires. For example, Enerhaug et al. (Enerhaug et al., 2001) applied multi-pass GTAW to join 20 mm thick supermartensitic stainless steel pipe and characterized the evolution in the microhardness, microstructure and pitting corrosion behaviour across the FZ and five HAZs. Carrouge et al. (Carrouge et al., 2004) examined GTAW of 12 mm thick supermartensitic stainless steel pipe to understand the effect of delta ferrite on the DBTT and indicated that the small grain size in the dual-phase region of the HAZ gives lower crack propagation even with the presence of 40% delta ferrite locally. Thibault et al. (Thibault et al., 2009) used FCAW to overlay six weld beads to fill a 4 mm square groove in a 54 mm thick UNS S41500 plate and examined the microhardness, microstructural phase constituents and residual stresses across the weldment.

However, for the assembly of thick-gage sections in low carbon martensitic stainless steels, conventional arc welding processes may not be sustainable from the context of the

high operational costs associated with manufacturing. In particular, multi-pass arc welding of thick sections with filler addition entails both extensive preparations for machining of the grooved interface as well as considerable material and labour investment to bridge the "gap" between the workpieces. As such, advanced high energy density processes, such as EBW, can offer considerable technological advantages for full penetration in thick gage sections by means of an autogenous single pass process. Specifically, both the high penetration depth and low heat input characteristics of EBW (Meleka, 1971) would generate a narrow FZ with a restricted HAZ, as well as minimized shrinkage and distortion (Sanderson et al., 2000) in the weld that, in turn, are promising for more uniform and/or reliable mechanical performance. In the present paper, EBW of UNS S41500, a 13%Cr–4%Ni low carbon martensitic wrought stainless steel grade, was conducted autogenously to produce a minimum penetration depth of 72 mm in a single pass without the application of preheating. Microstructural examination in combination with microhardness measurements were employed to interpret the phase transformations occurring across the weldment in the as-welded and PWHTed conditions. The mechanical properties of the EB welds were also evaluated using tensile testing in conjunction with a digital image correlation system, Aramis®, to understand the strain distribution in the different regions of the weld just before failure.

4.3   Experimental Procedure

4.3.1   Materials

The materials conditions (alloy, thickness, heat treatment) selected in this study were defined by the design specifications for hydroelectric turbine manufacturing. Specifically, 88 mm thick hot rolled ASTM A240 (ASTM-A240/A240M, 2004) grade UNS S41500, with a chemical composition (wt. %) of 13.02% Cr, 3.91% Ni, 0.74% Mn, 0.026% C, 0.56% Mo, 0.345% Si, 0.031% N, 0.021% P, 0.001% S, was selected. It is noteworthy that welding of UNS S41500 is recommended in the heat treated condition, single- or double-temper, over the as-rolled condition (ASTM-A480/A480M, 2012). As indicated in Figure 4-1, the UNS S41500 plates were normalized by heating up to 1000°C for 0.5 h followed by cooling in water to below the Mf of 90°C (Côté, 2007). The material was then subjected to a single-

temper heat treatment cycle that involved tempering at 600°C for 4 h, as illustrated in Figure 4-1.
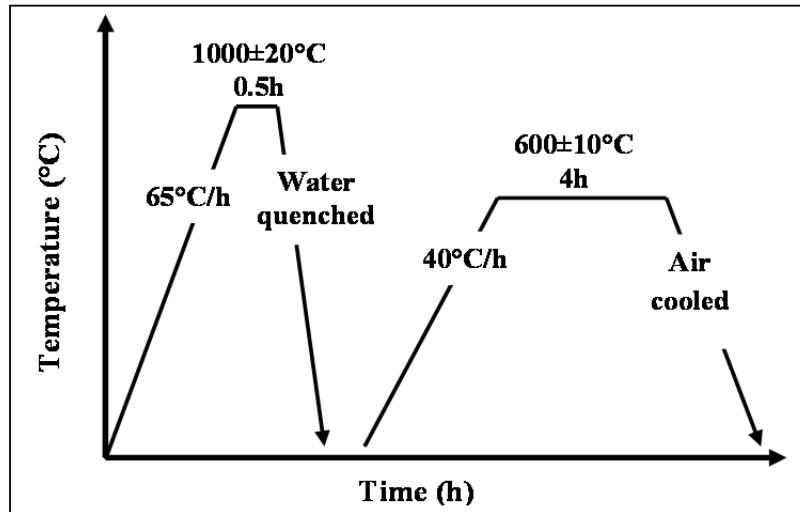
Figure 4-1 The normalizing and tempering thermal cycles
applied to UNS S41500 prior to EBW

4.3.2   Preparations for welding

The as-received UNS S41500 plates (in the normalized and tempered condition) were machined to obtain coupons with dimensions of 200 mm in length, 95 mm in width and 88 mm in thickness. Prior to welding, the surfaces of the coupons were degreased with acetone, followed by fine grinding with a scouring pad and final cleaning with ethanol to remove any surface contamination. The coupons were then demagnetized using an enclosed demagnetizer (R.B. Annis 4.5" × 14") followed by a surface demagnetizer (Electro-Matic model A13-1) to achieve a surface magnetic field reading between 0 and 1 gauss (Bakunov et al., 2004).

The coupons were then fixed to the worktable of the EBW system using a clamping fixture. It is worth mentioning that as the EBW process parameters typically ramp up to the programmed conditions at the start of the weld procedure and ramp down to zero at the end of the weld procedure, 'run on' and 'run off' lengths were established, as identified in Figure 4-2. To allow a stable weld length of about 200 mm, 'run on' and 'run off' tabs, each ~20 mm in length, were tacked to the coupon on either end.

Welding direction

Run on
20 mm

Length
200 mm

Run off
20 mm

Width
95 mm

Thickness
88 mm

y

x

z
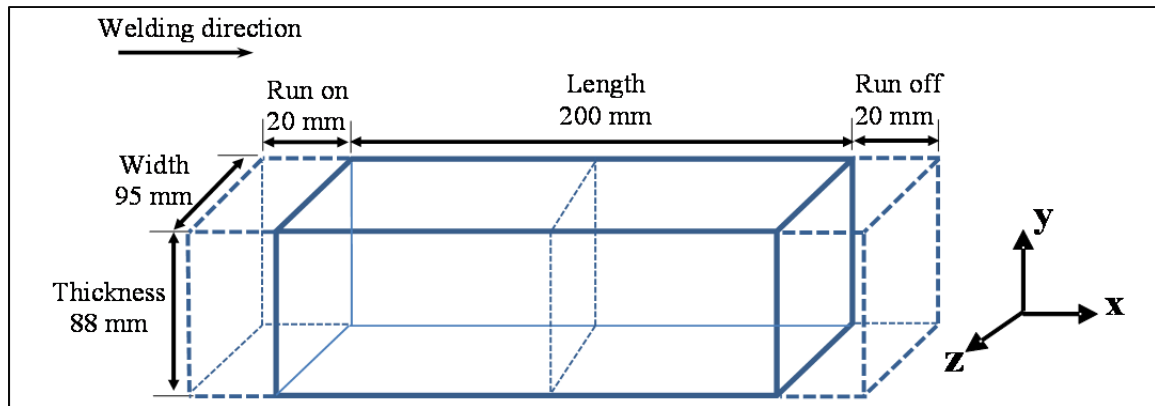
Figure 4-2 Schematic of the UNS S41500 coupon (with dimensions) used for bead-on-plate welding. The run on and run off tab lengths are indicated

4.3.3   Welding procedure

Autogenous bead-on-plate EB welds were produced along the length of the UNS S41500 coupon using a 42 kW Sciaky W2000 EBW system (60 kV/700 mA) operating with a pressure lower than 6.7×10-3 Pa. Specifically the electron beam was defocused by 10% and positioned at 62 mm below the top surface of the coupon. The objective for EBW was to demonstrate a minimum penetration of 72 mm across the 88 mm thick section of the UNS S41500 coupon with a single welding pass. It is noteworthy that partial penetration welds were manufactured so as to identify the backing surface boundary requirements for EBW that typically exhibits spiking at the weld root.

After EBW, the UNS S41500 welds were cooled to a temperature of 95°C or below to ensure that the martensite phase completely transformed prior to re-tempering between 565°C to 620°C according to the recommended guideline for PWHT (ASME Boiler and Pressure Vessel Code, 2007). In the present work, transverse slices, with dimensions of 20 mm in length, 95 mm in width and 88 mm in thickness, were sectioned from the partially penetrated UNS S41500 EB welds and tempered by heating at a rate of 50°C/h to 600±5°C, followed by holding for 12 h and then air-cooling, as illustrated in the thermal cycle given in Figure 4-3. It is notable that the temperature was monitored and controlled using K-Type thermocouples during PWHT; two thermocouples were attached to the sample surface to measure the temperature at two locations (top and bottom) and another to control the furnace

temperature. The difference between the measured temperatures from the furnace and thermocouples was less than 5°C.
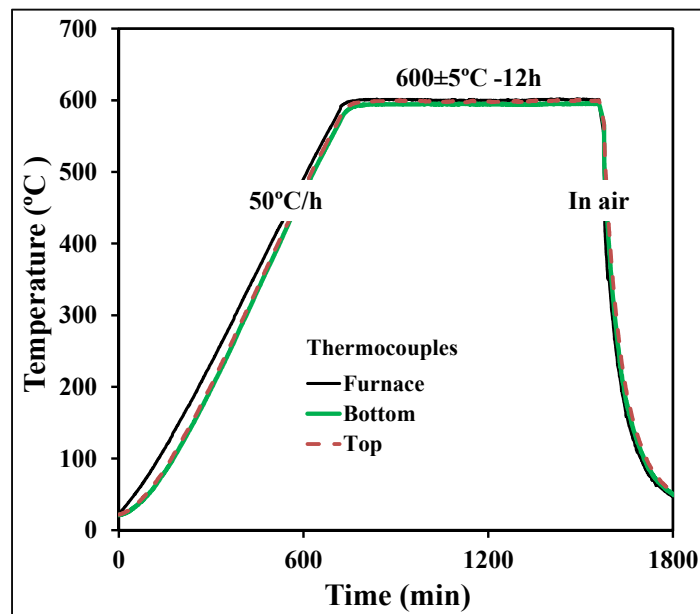
Figure 4-3 PWHT cycle applied after EBW

4.3.4   Metallographic and microhardness testing techniques

The UNS S41500 EB welds in the as-welded and PWHTed conditions were sectioned transverse to the welding direction (plane y-z in Figure 4-2) to extract specimens within the stable region for metallographic preparation and subsequent microscopic examination. Specifically, after sectioning of the EB welds using an abrasive cut-off wheel, the specimens were ground with 220 and 800 grit SiC papers followed by rough polishing using 9, 3 and 1 μm diamond suspensions with an alcohol based lubricant on silk polishing cloths. Final polishing was conducted using 0.05 μm colloidal silica on a porous pad. To reveal the general microstructural features, electrolytic etching of the specimens was performed by immersion at room temperature for 20 s in a solution of 10% oxalic acid with a voltage of 6 V at a current of 1.6 A using an austenitic stainless steel cathode.

An OM (Olympus GX-71) was used to examine the microstructural characteristics of the weldments in the FZ and the different HAZs at magnifications up to 1000x. A high

contrast U-DICRHC polarizing filter was used to adjust and enhance the contrast of the electrolytically etched microstructures in the FZ and different HAZs. Image analysis software (OLYMPUS Stream Motion) on the OM was used to quantify the delta ferrite fraction in the different regions.

To measure the retained austenite fraction at room temperature, XRD studies were carried out on select specimens extracted from (1) the as-received UNS S41500 material (in the normalized and tempered condition), (2) the FZ of the EB weld in the as-welded condition, (3) the BM region after PWHT and (4) the FZ in the PWHTed condition. Specifically, specimens with dimensions of 3 mm in thickness, 10 mm in length and 10 mm in width were extracted and prepared by grinding with 1200-grit SiC paper and chemical etching in an aqueous solution of 30% HCl and 30% HNO3. The X-ray diffraction data were collected at room temperature using a Bruker AXS D8-Advance diffractometer with CuKα radiation (wavelength of 0.15418 nm) at 40 kV and 30 mA. The diffraction angle (2θ), at which the X-rays impinged the specimen surface, was varied from 40° to 140° with a step size of 0.05° and a pause of 3 s at each step. The DiffracPlus software of the diffractometer allowed initial processing of the diffraction pattern to differentiate the peaks corresponding to the austenite phase from the martensite phase. Quantification of the retained austenite fraction was performed using Topas R, an analysis software based on the Rietveld method (Young, 1993).

For the UNS S41500 EB welds in the as-welded and PWHTed conditions, Vickers microhardness testing was performed using a Struers DuraScan machine equipped with an motorized x-y stage and a fully automated testing cycle (i.e. stage movement, loading, focusing, and measurement). Using the ecos WorkflowTM software module, Vickers microhardness mapping on the transverse sections of the EB welds (i.e. perpendicular to the welding direction) was carried out with a uniform distribution of test points across the entire surface at an interval of 2 mm (for mapping), a load of 500 g and a dwell period of 3 s. Two- and three-dimensional image maps of the hardness distribution on the surface of the EB welds in the as-welded and PWHTed conditions were then generated using the areaMASTER function in the ecos WorkflowTM software module. In addition, the microhardness profile

across the weld at a depth of 22 mm below the top surface was measured under similar loading conditions and a much smaller indent interval of 0.3 mm. It is noteworthy that the minimum test point separation distance for all measurements was at least three times the diagonal measurement of the indent to avoid contributions from the neighbouring strain fields (ASTM-E384-11E1, 2011).

4.3.5   Tensile testing methodology with DIC

Tensile samples were extracted from the as-welded and PWHTed UNS S41500 EB welds, as shown in Figure 4-4. Specifically, four types of tensile samples were prepared as described in Table 4-1: standard sub-size, Type A, Type B, and Type C. In particular, the standard sub-size tensile samples were extracted from the cross section of the EB welds (Figure 4-4a) in the as-welded and PWHTed conditions as well as the as-received BM, and then machined with dimensions according to ASTM E8M-04 with a gage length of 25.4 mm (ASTM-E8/E8M-15a, 2013). By contrast, the geometry (gage length and width) of Type A, B, and C tensile samples were scaled from the standard sub-size dimensions, as illustrated in Figure 4-4b and c, to trigger failure in different regions of the EB weld, e.g. FZ or HAZ, so as to determine the local mechanical properties in these regions. It is noteworthy that without this approach, failure occurred exclusively in the BM and it was not possible to characterize the local properties in the different regions of the EB weld.

In Table 4-1, the respective dimensions of Type A, B, and C tensile samples are given along with a parameter to ascribe the relative fraction of the gage length that consists of the FZ. For instance, Type A and C tensile samples have the same gage length, but the FZ/G ratio is different because the FZ fraction in the gage length of Type A is greater than that in Type C. In fact, in Type A tensile samples, the FZ spanned the entire gage length, while in Type C samples only 70% of the gage length was the FZ and the rest was the HAZ. By contrast, the gage length of Type B tensile samples was twice that of Type A or C. However, the FZ/G was only 40% in the Type B tensile samples. It is noteworthy that to determine the FZ/G ratio, one side of each tensile sample was metallographically prepared by grinding and polishing, as described previously, followed by chemical etching in an aqueous solution of Vilella's reagent to reveal the different microstructural regions.
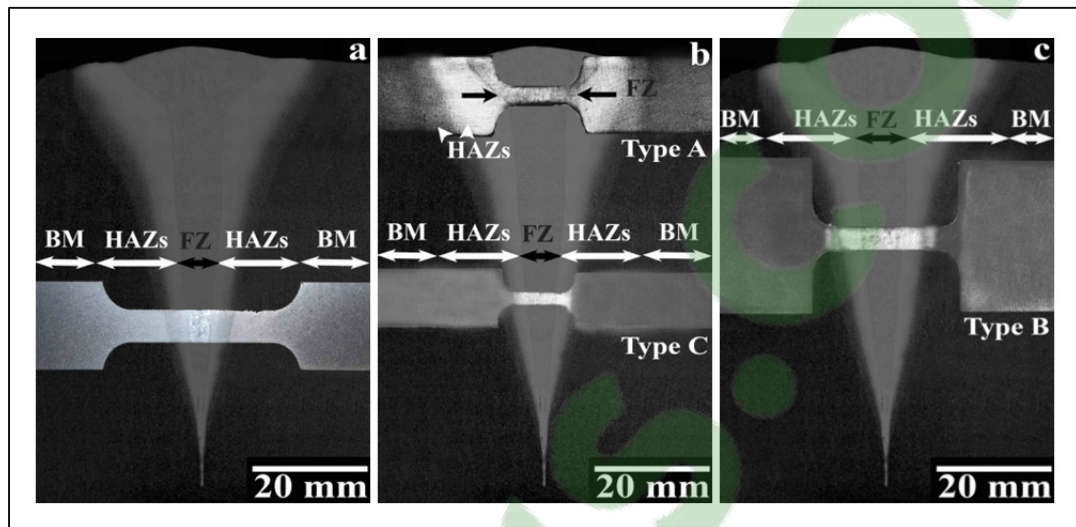
Figure 4-4 Tensile samples extracted from the transverse cross section of the
EB welds: (a) sub-size (As-welded and PWHTed), (b) Type A and Type C, and
(c) Type B samples

Table 4-1 Tensile sample dimensions extracted from the transverse cross
section of the EB weld

	Sub-size(ASTM-E8/E8M-15a, 2013)	Type A	Type B	Type C
G	25.4±0.1	10±0.1	20±0.1	10±0.1
W	6.4±0.02	2.9±0.02	2.9±0.02	2.9±0.02
T	3.8±0.02	2.95±0.02	2.95±0.02	2.95±0.02
A	34	30	25	30
R	3.15±0.02	3.15±0.02	3.15±0.02	3.15±0.02
B	15.2±0.02	12±0.02	20±0.02	12±0.02
FZ/G	0.3	1	0.4	0.7

For both the as-welded and PWHTed conditions, up to four tensile samples for each geometry were then mechanically tested at room temperature using a 250-kN MTS testing frame integrated with a laser extensometer and a non-contact optical 3D deformation measurement system, Aramis® (Gesellschaft fur Optische Messtechnik, Braunschweig, Germany (ARAMIS User Handbook, 2001)), as illustrated in Figure 4-5a. Prior to tensile testing, the etched side of the sample were marked with two pieces of retro-reflective tape to define the gage length for the laser extensometer measurements during testing, as shown in Figure 4-5b. On the opposite un-etched side, the surface of the tensile sample was first painted with a white background and then with a high-contrast random pattern of black speckles was applied, as illustrated in Figure 4-5c. It is noteworthy that as the functionality of the Aramis® system is sensitive to the quality of this speckle pattern, verification of pattern recognition was performed before conducting tensile testing to ensure proper strain recording along the entire gage length (Peters et Ranson, 1982; Wanjara et al., 2014). Tensile tests were conducted until rupture using displacement control at a rate of 2 mm·min^{-1}. To obtain the global stress-strain curves and related mechanical properties, the load data collected from the tensile testing machine, was used to calculate the engineering stresses during the test, while the related strains were calculated from the displacement obtained from the laser extensometer. The mechanical properties evaluated in this work included the YS, UTS, and %El. obtained from the stress-strain curve of each tensile sample.

The deformation captured by the Aramis® system was used to map the 2D strain distribution along the gage length of each tensile sample. Since the acquisition rate of the tensile machine and the laser extensometer (50 Hz) was different from the Aramis® system (2 fps or 2 Hz), synchronization of data was performed using an in-house code that matched the failure stage/point of the two strain acquisition systems and back-calculated the related stress data for each deformation stage recorded by the Aramis® system. In the end, the stress-strain curves obtained using the load data from the tensile machine with the strain data from the Aramis® system or the laser extensometer were compared to ensure corroboration between the two strain data sets.

After tensile testing, the topological characteristics of the fracture surface were mapped using an Olympus LEXT OLS4000 3D confocal LSM. Also SEI was performed at 20 keV on a Hitachi S-3600N SEM for fractographic examination of the fracture surface of select tensile samples. Also an Olympus DSX500 opto-digital microscope and a Hitachi TM3030 SEM were used to examine selected metallographic samples of the tensile fractures with a selective electrolytic etching for δ ferrite phase in a 20% aqueous solution of NaOH.
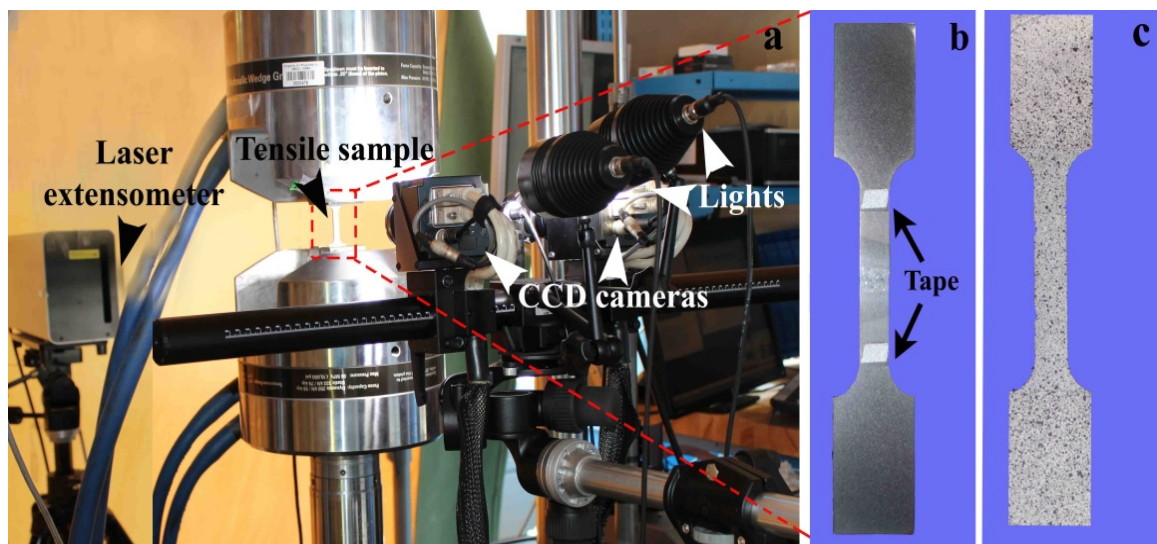
Figure 4-5 (a) MTS tensile testing configuration showing the position of the laser extensometer relative to the two CCD cameras of the Aramis® system, (b) etched side of the tensile sample showing the reflective tape applied to demarcate the gage length and (c) opposite side of the tensile sample that was painted with a speckle pattern

4.4   Results and Discussions

4.4.1   Microhardness and microstructural evolution in the as-welded and PWHTed conditions

Figure 4-6 illustrates the weld bead characteristics of EB welded UNS S41500 martensitic stainless steel using a single pass autogenous process without preheating that achieved a minimum penetration of 72 mm without the occurrence of weld defects (e.g. porosity or cracking). The etched macrostructure across the transverse cross section of EB welded UNS S41500 in the as-welded (Figure 4-6a) and PWHTed (Figure 4-6b) conditions

reveals different distinct regions. These can be interpreted from consideration of the microhardness evolution, thermal history during welding and PWHT, and possible phase transformations in the ternary Fe-Cr-Ni alloy system (Folkhard et al., 1988).
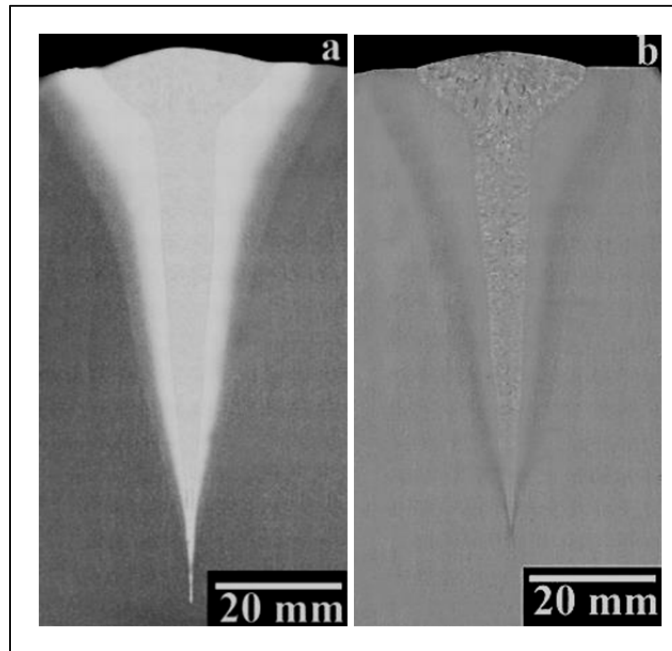
Figure 4-6 OM images of the macrostructure
showing the entire transverse cross section of
EB welded UNS S41500 in: (a) as-welded and
(b) PWHTed conditions

For the as-welded and PWHTed conditions, the 2D and 3D hardness maps (Figure 4-7) provide an overview of the hardness evolution on the entire transverse cross-section of EB welded UNS41500, as shown in Figure 4-6. For the as-welded condition, the minimum and maximum hardness values from these maps were 260 HV and 410 HV, which respectively correspond to the BM and HAZ of the EB welds. By contrast, the application of PWHT was observed to decrease the hardness throughout the entire weldment and the minimum and maximum hardness values were 258 HV and 323 HV, which correspond to the BM and FZ, respectively. Also, PWHT had the effect of reducing the occurrence of the hardness peaks and troughs such that an overall homogenization in the hardness values was apparent.
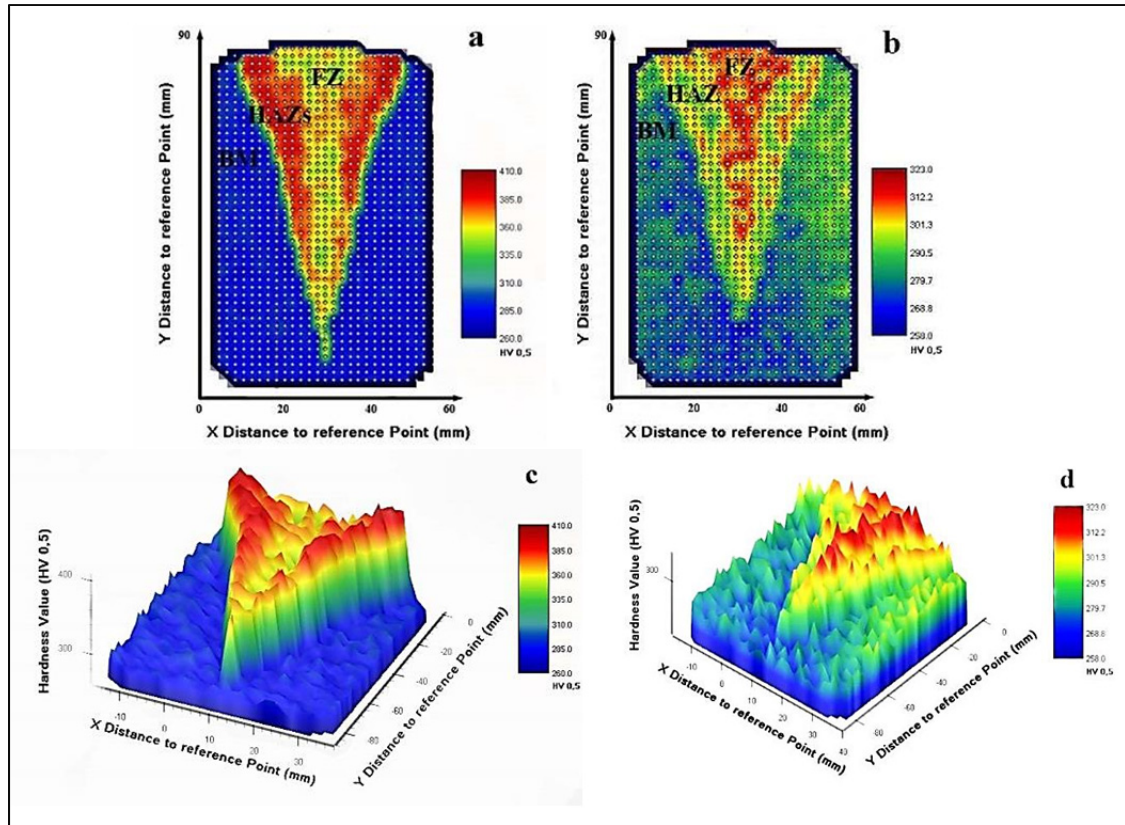
Figure 4-7 Two- and three-dimensional hardness maps for the entire transverse section of the EB welds: (a) and (c) as-welded, and (b) and (d) PWHTed conditions

Considering the relatively large indent interval (2 mm) applied for generation of the 2D and 3D hardness maps, discretization of the different areas in the weldment, especially in the HAZ was not possible without the generation of hardness profiles using a smaller indent spacing (0.3 mm). Accordingly, Figure 4-8a shows, for the as-welded and PWHTed conditions, the hardness evolution across the EB weldment at a depth of 22 mm below the top surface. It is noteworthy that at different depths from the top surface, the hardness profiles were found to be similar to those illustrated in Figure 4-8a, except for the relative breadth of the different regions identified. The hardness profiles corroborate the overall observations and findings of the minimum and maximum hardness values in the as-welded and PWHTed conditions determined from the 2D and 3D hardness maps. In addition, the hardness profiles give evidence of hardness differences within the HAZ of especially the as-welded UNS S41500, which are indicative of different microstructural characteristics. It is noteworthy that in Figure 4-8a, even though the demarcated regions, i.e. BM, HAZ5, HAZ4,

HAZ3, HAZ2 and FZ, were discretized strictly on the basis of observations for the as-welded condition, these remain as a point of reference for understanding the effect of PWHT on the hardness in each area.

Particularly, thermal cycling during EBW leads to temperatures ranging from the melting point of UNS S41500 (~1500°C) in the vicinity of FZ to a temperature in the BM where no significant phase transformations occur (~580°C). Considering the phase equilibrium in the Fe-Cr-Ni ternary diagram (Folkhard et al., 1988), the sequential phase changes that can occur in UNS S41500 during heating, which, on cooling, result in the different microstructural regions in the weld are: α + C1 (BM) → α + γ + C1 (HAZ5) → γ (HAZ4) → γ + δ (HAZ3) → δ (HAZ2) → δ + L (HAZ1)→ L (FZ), where C1 is the M23C6 carbides and L is the liquid phase.
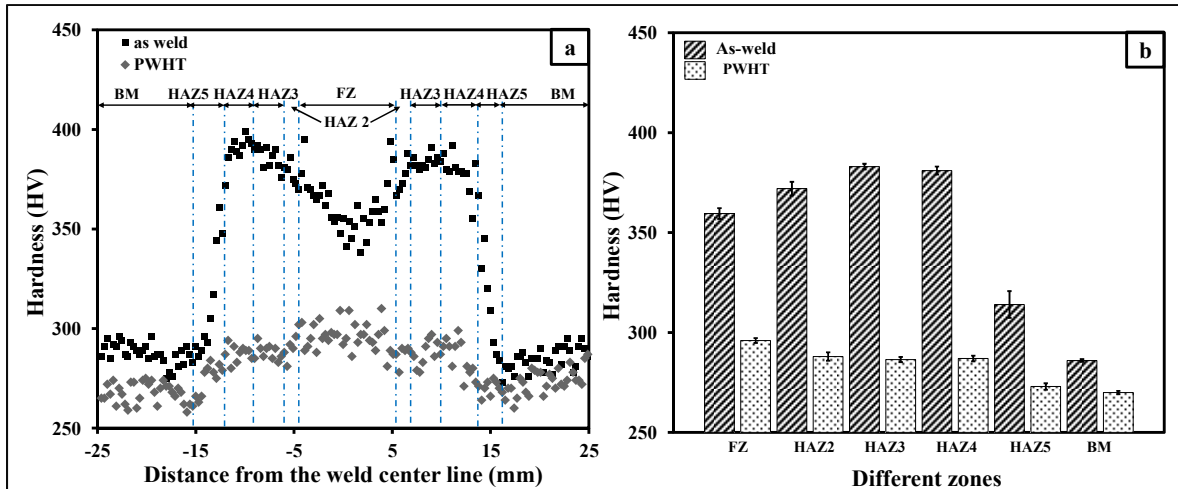
Figure 4-8 (a) Hardness profile across the as-welded and PWHTed EB welds at a position of 22 mm under the top surface, and (b) average hardness in the six different regions of the as-welded and PWHTed EB welds (with the error bars representing two standard deviations of uncertainty)

Consistent with the above analysis, the BM microstructure of the as-received UNS S41500 in the normalized and tempered condition consisted predominately of tempered martensite laths, as illustrated in Figure 4-9a. However, non-equilibrium solidification can lead to retention of high temperature phases in the microstructure of UNS S41500 at room temperature, such as delta ferrite (Figure 4-9a) and retained austenite (Wang et al., 2010). It

is noteworthy, however, that the retained austenite phase forms between the martensite laths in UNS S41500 and is relatively small in size (up to 500 nm) and, thus, difficult to discern with an OM or SEM (Bilmes, 2001; Thibault, 2011).
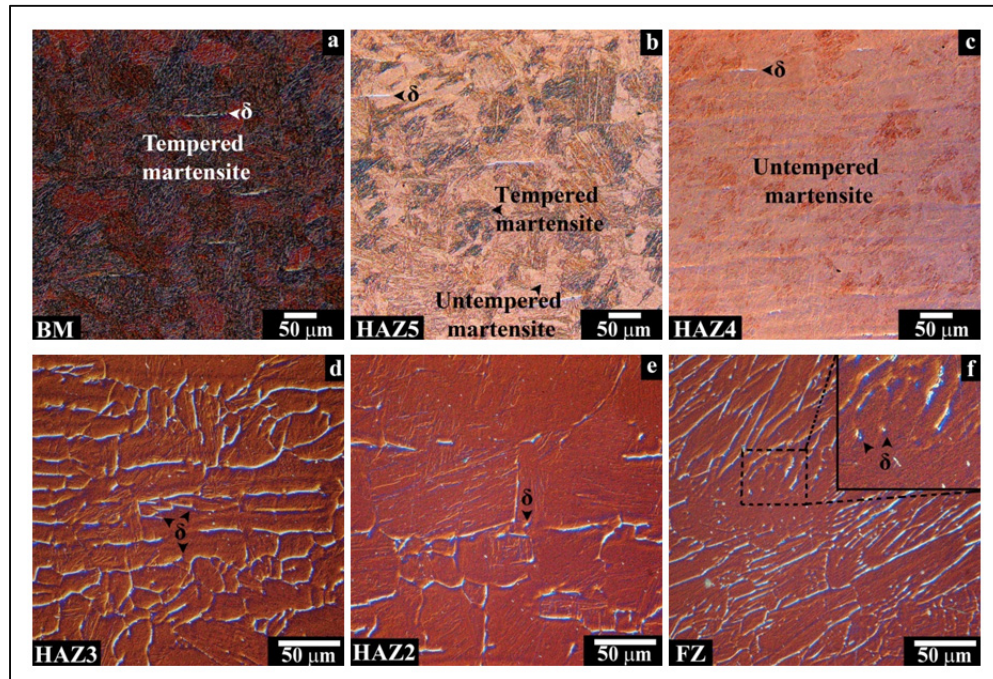
Figure 4-9 OM images of the microstructure in as-welded UNS S41500: (a) BM, (b) HAZ5, (c) HAZ4, (d) HAZ3, (e) HAZ2, and (f) FZ (with the absence of HAZ1)

The fraction of delta ferrite and retained austenite, measured using image analysis with OM and XRD, respectively, are given in Table 4-2. For this microstructural condition of the BM, the average hardness was 286±0.7 HV (Figure 4-8b). It is noteworthy that the average hardness reported in Figure 4-8b was calculated from the arithmetic average of the values measured for each region. After PWHT, the average hardness in the BM was observed to decrease by ~10 HV, as illustrated in Figure 4-8b. This softening can be attributed to the measured increase in the retained austenite fraction in the BM microstructure after PWHT, as given in Table 4-2. Specifically, during re-tempering of the as-received (normalized and tempered) BM microstructure, some martensite would partially transform to austenite (often referred to as reversed austenite). This reversed austenite stabilizes during prolonged holding for 12 h at 600°C, and then is retained during cooling to room temperature through a

mechanism described as anomalous phase transformation (Song et al., 2010a; Song et al., 2010b). Since the hardness of the retained austenite phase is lower than that of the tempered martensite or delta ferrite phases (Neubert et al., 2004), this softening can thus be reasonably explained by the increased fraction of retained austenite after PWHT.

Table 4-2 Fraction of delta ferrite and retained austenite measured by
XRD and image analysis

Microstructural Features	As-Received	As-welded	PWHTed
Delta Ferrite in (tempered) BM (%)	<5	N/A	<5
Retained austenite in (tempered) BM (%)	~10	N/A	~17
Delta ferrite in FZ (%)	N/A	<5	<5
Retained austenite in FZ (%)	N/A	~1	~14

During EBW, heating of the BM microstructure above the Ac1 temperature of ~580°C increasingly transforms the tempered martensite phase to reversed austenite. Hence in the HAZ closest to the BM, HAZ5, the reversed austenite formed on heating would transform to untempered martensite on cooling to room temperature after EBW. Microstructural observation of HAZ5 indicated the presence of a mixture of dark-etched regions (tempered martensite) and light-etched regions (untempered martensite), as illustrated in Figure 4-9b. Also, the hardness profile (Figure 4-8a) for the as-welded condition showed a progressive increase in the hardness within HAZ5. In particular, the hardness increased from 283 HV next to the BM, where the fraction of dark-etched tempered martensite was predominant, to 372 HV next to HAZ4, where the fraction of light-etched untempered martensite was predominant. Considering that the untempered martensite is harder than the tempered martensite, the observed microstructural evolution corroborates well with the measured microhardness evolution. PWHT then (i) tempered and softened the untempered martensite fraction and (ii) re-tempered and further softened (retained austenite stabilization) the remnant tempered martensite fraction in the HAZ5 microstructure. Hence, the overall hardness in HAZ5 after PWHT was lower than that in as-welded condition (Figure 4-8b). However, the trend of increasing hardness still remained, such that the hardness after PWHT was ~287 HV near the HAZ4 interface and 262 HV next to the BM.

The microstructure in HAZ4 is a consequence of the temperatures during EBW surpassing the Ac3. As such, on heating, the tempered martensite phase in the BM microstructure would fully transform in this region to austenite and concomitantly the dissolution of M23C6 carbides would also occur. It is noteworthy that full dissolution of the carbides in the austenite is a time-temperature dependent process (Folkhard et Rabensteiner, 1988). Thus in HAZ4, the extent of carbide dissolution is a function of the local conditions, namely chemical composition, peak temperature, and heating rate. Progressing from the HAZ5/HAZ4 boundary to the HAZ4/HAZ3 boundary, an increase in the carbide dissolution would raise the carbon content in the austenite. On cooling after welding, this austenite – with differing carbon contents – in HAZ4 reverts to untempered martensite (that has a hardness inherently related to this carbon content). Thus, a predominant martensitic microstructure was observed in HAZ4 (Figure 4-9c) and a maximum hardness of 399 HV was measured close to the HAZ3 boundary (Figure 4-8a) in the as-welded condition. PWHT naturally tempered this untempered martensitic microstructure in HAZ4, which decreased the hardness to 295 HV, roughly ~25% lower than the as-welded value.

During EBW, the region heated to temperatures above the Ac4, HAZ3, would experience full transformation of martensite to austenite and partial transformation of the austenite to delta ferrite. Thus, on heating, the nucleation of delta ferrite would occur at the prior-austenite grain boundaries where it can be retained due to the partitioning of ferrite-stabilising elements and the fast cooling rate after EBW (Bilmes, 2001). Figure 4-9d reveals the microstructure observed in HAZ3 that consisted of an untempered martensitic matrix with delta ferrite (~4%) retained at the prior-austenite grain boundaries. For the as-welded condition (Figure 4-8a), the hardness profile in HAZ3 revealed a slight decrease in hardness from the maximum value measured in HAZ4. However, the average hardness of HAZ3 was similar to that in HAZ4 for both the as-welded and PWHTed conditions, most likely due to the similarity in the microstructures, i.e. phases present (martensite, delta ferrite and retained austenite) and relative fractions.

Immediately adjacent to HAZ3, towards the FZ, HAZ2 was heated to temperatures above Ac5 during EBW. As such, full transformation of austenite to delta ferrite occurred in

HAZ2, and, due to the elevated temperatures, significant growth of the delta ferrite grains transpired during heating. On cooling, the microstructure in HAZ2 was observed to consist of coarse grained untempered martensite with some delta ferrite particles at the prior-austenite grain boundaries, as shown in Figure 4-9e. Progressive coarsening of the microstructure towards the FZ was observed in HAZ2 and the hardness decreased steadily from the HAZ3 boundary to the FZ as illustrated in Figure 4-8a. Also, in the as-welded condition, the average hardness of 372 HV measured in HAZ2 was lower than that in HAZ3 (383 HV) and HAZ4 (381 HV). This may be attributed to coarsening of the microstructure in HAZ2 relative to HAZ3 and HAZ4.

Between HAZ2 and the FZ, a PMZ or HAZ1 can be theoretically postulated. Here, incipient melting of the nucleated delta ferrite formed on heating during EBW would occur. However, for the EB weldments in UNS S41500, HAZ1 was impossible to distinguish; this finding is analogous to that previously reported for FCAW (Thibault; 2011), GTAW (Carrouge, 2004; Enerhaug, 2001) and EBW (Sarafan et al., 2015) of martensitic stainless steels with similar chemistries to that used in the present work.

In the FZ, heating to the melting temperature of UNS S41500 occurs during EBW and solidification on cooling resulted in a microstructure (Figure 4-9f) consisting of oriented dendritic columnar grains that were predominately martensite with the presence of up to 5 vol. % δ-ferrite remaining on the prior-austenite grain boundaries and less than 1 vol. % retained austenite (Table 4-2). In the as-welded condition, the hardness in the FZ ranged from maximum values (~394 HV) near the periphery to ~338 HV around the weld center. Also, the average hardness of the FZ (360 HV) in the as-welded condition was slightly less than that in the HAZ2, HAZ3 or HAZ4 (Figure 4-8b). By contrast, after PWHT, the average hardness in the FZ (296 HV) was slightly higher (288 HV) than HAZ2, HAZ3 or HAZ4. Also after PWHT, the maximum hardness in the FZ decreased from 394 HV to 309 HV (27% decrease) and the hardness distribution was observed to be considerably more uniform. For the PWHTed condition, this decrease in the FZ hardness can be attributed to tempering of the martensite phase, as well as the increased retained austenite fraction (Table 4-2) in the microstructure relative to the as-welded condition. It is also noteworthy that in the PWHTed

condition the central region of the FZ was about 15-30 HV higher than the adjoining periphery.

Overall, the microstructural observations for the BM, FZ and different HAZs in EB welded UNS S41500 are in agreement with previous work on martensitic and supermartensitic stainless steels that were joined by EBW (Sarafan et al., 2015; Sarafan et al., 2013), HLAW (Mirakhorli et al., 2014), FCAW (Thibault, 2009) and GTAW (Carrouge, 2004). Also, the trends in the hardness evolution were similar, though the absolute values for the average hardness in the different regions of the weldment were different, as compared in Table 4-3. The hardness difference may be due to the higher carbon content of the martensitic stainless steel, since it controls the lattice dilation during transformation to a slipped or twinned product (Lippold et al., 2005).

Table 4-3 Carbon content and average hardness in the six distinct regions of welded martensitic stainless steels

Welding process	Carbon (%)	BM (HV)	HAZ5 (HV)	HAZ4 (HV)	HAZ3 (HV)	HAZ2 (HV)	FZ (HV)
EBW [present work]	0.026	286	314	381	383	372	360
EBW* (Sarafan et al., 2013; 2015)	0.056	282	293	389	405	400	403
FCAW** (Thibault, 2009)	0.017	300	311	363	363	354	365

*BM was double tempered prior to welding
** Carbon content of filler metal was 0.02%

4.4.2 Tensile properties

The global tensile properties of the UNS S41500 in the as-welded and PWHTed conditions are summarized in Table 4-4 and Figure 4-10. It is noteworthy that the global tensile properties determined for the BM, as-welded and PWHTed conditions were obtained using standard sub-size specimens. Accordingly, for the as-welded and PWHTed conditions,

all six regions of the EB weld were present in the gage length of this tensile sample geometry and contributed to the global properties measured. By contrast, in the as-welded condition using Type A, B and C sample geometries only the FZ with/without the HAZs contributed to the measured global tensile properties.

Table 4-4 Global tensile properties and failure location for UNS S41500

Sample ID	Sample condition	Failure location	FZ/G	YS (MPa)	UTS (MPa)	%El. (%)
UNS S41500[1]	Tempered	BM	N/A	N/A	>755	N/A
UNS S41500[2]	Tempered	N/A	N/A	>620	>795	>15
BM*	BM	BM	N/A	741.9	855.9	20.7
As-welded*	As-Welded	BM	0.3	730.0	820.0	11.4
PWHTed*	PWHTed	BM	0.3	657.6	779.5	10.7
Type A	As-Welded	FZ	1	876.5	1094.8	21.9
Type B	As-Welded	FZ	0.4	914.9	1084.9	11.8
Type C	As-Welded	FZ	0.7	934.7	1122.8	21.6

*Standard sub-size tensile sample geometry, as defined in Table 4-1.
1 (ASME Boiler and Pressure Vessel Code, 2010)
2 (ASTM-A240/A240M, 2004)

For UNS S41500, the values measured for the as-received BM (in tempered condition), namely 742 MPa for the YS, 856 MPa for the UTS and 20.6% for the %El., meet the minimum requirements of 620 MPa for YS, 795 MPa for the UTS and 15% for the %El. as specified in (ASTM-A240/A240M, 2004). For the welds, the acceptance criterion according to ASME Section IX (ASME Boiler and Pressure Vessel Code, 2010) stipulates failure in the BM and a maximum reduction of 5% in the UTS (or a value of 755 MPa) for EB welded UNS S41500. In this work, the UTS measured for the as-welded condition (820 MPa) was ~3% higher than the specification for the BM (795 MPa), while that for PWHTed condition (780 MPa) was ~2% lower than the BM specification. Also, the fracture location during tensile testing of all the as-welded and PWHTed samples was exclusively in the BM region (Figure 4-11). This is unsurprising since the BM region in both the as-welded and PWHTed conditions had the lowest hardness (Figure 4-7 and Figure 4-8) and, as such, during tensile

testing, failure localization after necking occurred in this lower strength region. Thus, the tensile properties of EB welded UNS S41500 in both the as-welded and PWHTed conditions met the acceptance criteria of ASME Section IX, which validates the feasibility of applying EBW for hydroelectric turbine manufacture.
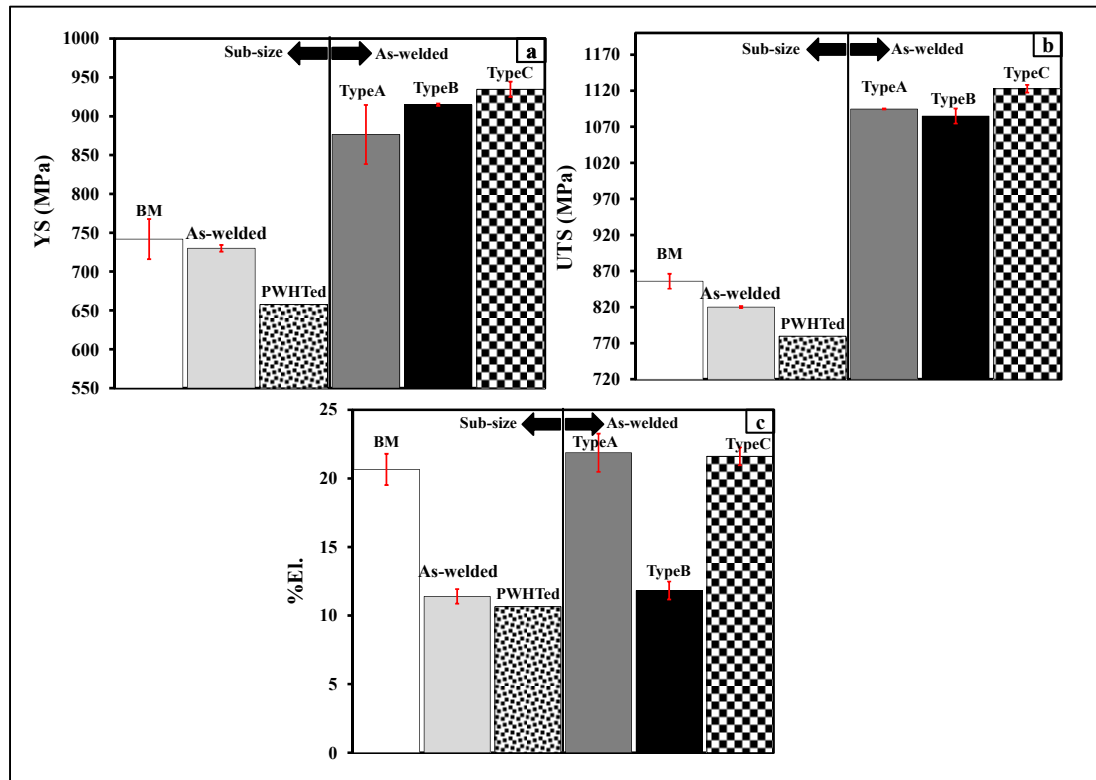
Figure 4-10 Effect of EBW, PWHT and tensile sample geometry on the global tensile properties of UNS S41500: (a) YS, (b) UTS, and (c) %El. Two standard deviations of uncertainty are also indicated by the error bars.
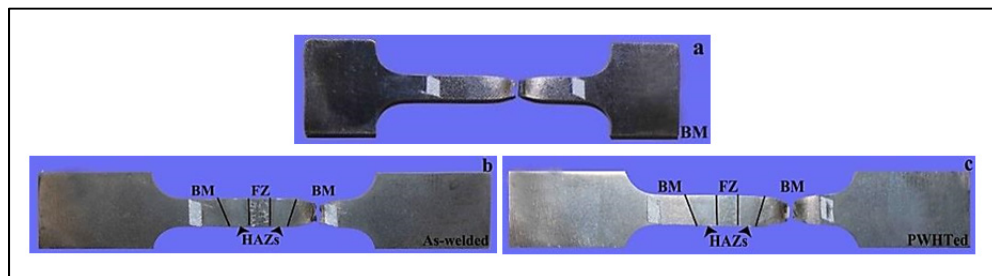
Figure 4-11 Typical failure locations in standard sub-size geometry samples that were tensile tested: (a) BM, (b) As-welded UNS S41500 and (c) PWHTed samples

As indicated in Table 4-4, the YS and UTS values in the as-welded condition (730 MPa and 820 MPa) were slightly lower than the measured values for BM (742 MPa and 856 MPa) and slightly greater than the PWHTed condition (658 MPa and 780 MPa). These results can be attributed predominately to the fraction of tempered, untempered and re-tempered martensite in the microstructure. For instance, compared to the tempered martensite microstructure of BM, the presence of untempered (higher hardness) martensite in the HAZ and FZ increases the strength locally, such that the strain localizes in the tempered martensite (lower hardness) microstructure of the BM and gives similar strength properties but a lower %El. (11.4%) for the weldment. PWHT tempers the untempered martensite in the FZ and HAZ and re-tempers the tempered martensite in the BM. Thus PWHT reduces the overall internal stresses and dislocation density (Zou et al., 2010) across the weld and renders slightly lower strength properties, as compared to the as-welded condition. However, even in the PWHTed condition, the differences in hardness between the re-tempered martensite in the BM (softer) and the tempered martensite in FZ and HAZ (harder) again result in strain localization and fracture in the BM at a relatively similar %El. value (10.7%).

The influence of these microstructural features in the different regions of the weldment on the global tensile properties was further examined using Type A, B, and C tensile samples. In particular, the global properties determined using Type A, B and C tensile samples indicated considerably higher YS (876-935 MPa) and UTS (1085-1123 MPa) values (Table 4-4), as well as failure exclusively in the FZ, as illustrated in Figure 4-12. These values for the YS and UTS are respectively ~ 22% and 29% greater than that of the BM (Figure 4-10). Also, compared to the measured YS of 730 MPa and UTS of 820 MPa for the as-welded sample, the YS and UTS measured using Type A, B and C tensile samples are respectively 24% and 35% greater. By contrast, the %El. measured using Type A (21.9%), B (11.8%) and C (21.6%) tensile samples was either similar to the BM (20.7%) or as-welded (11.4%) values. These findings suggest that the BM microstructure and associated strength properties override the global properties in the "composite" structure of the EB weldment (with six different regions). Hence, in the absence of the BM region in the Type A tensile samples, the excellent global properties (Table 4-4) are characteristic of the FZ microstructure, as validated in Figure 4-12a through hardness mapping and etching of the

fractured tensile samples. For Type B and C tensile samples, the global properties listed in Table 4-4are influenced by the characteristics of both the FZ and HAZs, as illustrated in Figure 4-12b and c. It is particularly noteworthy that as the FZ/G ratio decreases, the influence of the FZ characteristics on the global properties diminishes as well exemplified by comparing the results from Type B and C tensile samples. Specifically, the global tensile properties measured using the Type C sample geometry (FZ/G ratio of 0.7) are comparable to those obtained for the Type A sample geometry (FZ/G ratio of 1). By contrast, the global tensile properties measured using the Type B sample geometry (FZ/G ratio of 0.4) exhibited greater contributions from the HAZs, which then manifested in a lower elongation (11.8%) that was, nonetheless, comparable to the value of 11.4% measured for the as-welded sample that had a FZ/G ratio of 0.3. Hence, these global tensile properties measured locally in the EB weldment, which indicate high strength and good ductility for the as-welded microstructure in the FZ and HAZs, offer additional impetus to consider the EBW technology for next-generation hydroelectric turbine manufacture.
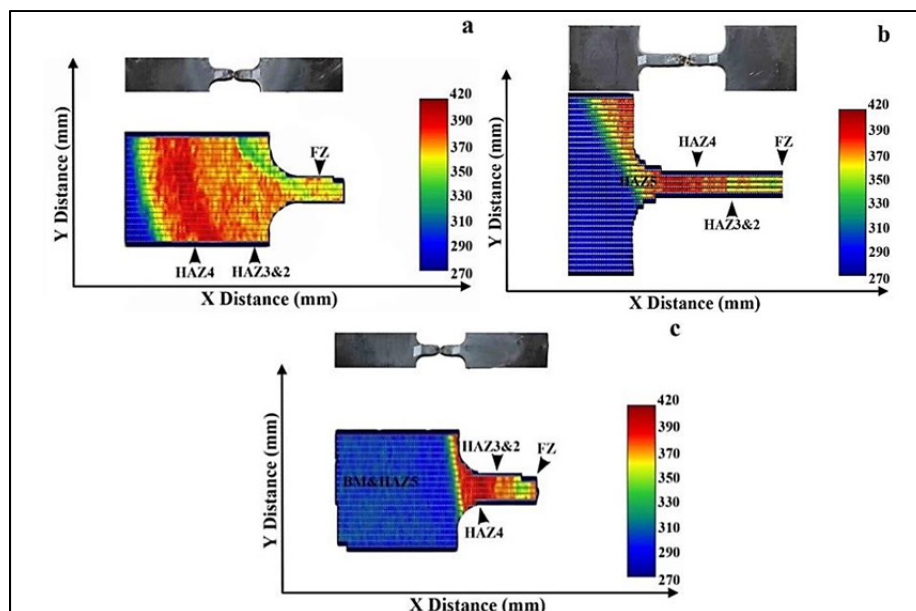
Figure 4-12 Typical fracture locations and associated 2D hardness maps in: (a) Type A, (b) Type B, and (c) Type C tensile samples extracted from as-welded UNS S41500

Examination of the tensile fracture surface using a confocal LSM enabled imaging of the cup and cone ductile topological features, as shown in Figure 4-13. In particular, both the matte optical reflectivity of the fracture surface (observed visually) and the surface roughness quantified in Figure 4-13, give evidence for the occurrence of plastic deformation during tensile loading.
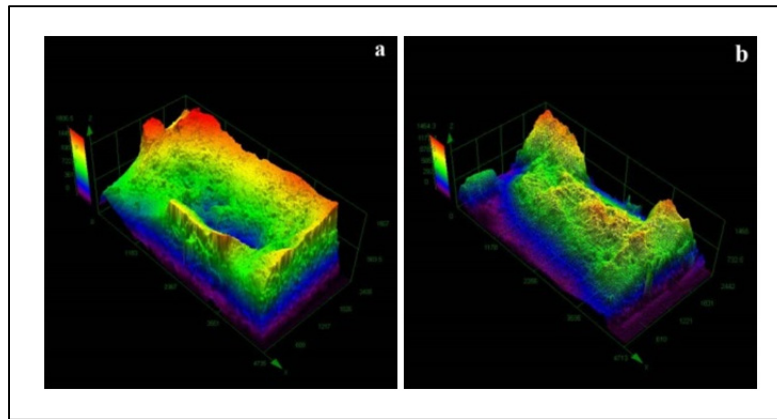
Figure 4-13 Images observed using a confocal LSM that
reveal (a) the cup and (b) the cone ductile fractures surfaces
of the as-welded UNS S41500 that failed in the BM

Closer examination of the tensile fracture surface using SEI with a SEM, as illustrated in Figure 4-14, indicated dimpled fracture surfaces for each sample condition tested and indicates that the principal failure mechanism involves microvoid formation, growth and coalescence in the matrix microstructure. In addition, the BM microstructure of predominantly tempered martensite was noted above (in Table 4-2) to consist of some secondary phases, including ~5 vol.% delta ferrite stringers and ~10 vol.% retained austenite between the martensite laths. As such, debonding at the interfaces between these secondary phases and the martensitic matrix can also occur during plastic deformation and the voids initiated by this process can grow and coalesce into a macroscale crack (Figure 4-14a). Tensile loading of both the As-welded and PWHTed samples resulted in strain localization and failure in the BM. As such, the dimpled features on the fractographic surface of both the As-welded (Figure 4-14b) and PWHTed (Figure 4-14c) samples were observed to be relatively similar to that of the BM. By contrast, the tensile fracture surface of Type A, B and

C samples that failed in the FZ exhibited finer and more uniformly distributed dimples, as revealed in Figure 4-14d-f. This may be a result of the fast cooling rate experienced in the FZ that refines the overall microstructure, namely lath martensite matrix with delta ferrite (Figure 4-9f) along the interdendritic prior-austenite grain boundaries and retained austenite (Table 4-4) along the martensite interlath boundaries. From a microscale perspective, though it is difficult to directly relate the dimple size with ductility, the presence of fine uniformly distributed dimples (as seen in Figure 4-14d-f) on the tensile fracture surfaces are reported to be indicative of high microstructural quality and fine, uniformly distributed second phase particles in ferrous alloys (Nguyen-Duy, Tremblay et Lanteigne, 1988). Thus, in present work, the formation of fine lath martensite with small secondary phase (delta ferrite and retained austenite) particles in the microstructure of the FZ leads to a more uniform distribution of the plastic deformation during tensile loading, as construed from the uniform and fine dimple morphologies on the fracture surface. By contrast, in the tempered microstructure of the BM, strain localization at the secondary phases is prominent and the tensile fracture surface manifests irregular dimple morphologies within which particulates could be observed (Figure 4-14c).
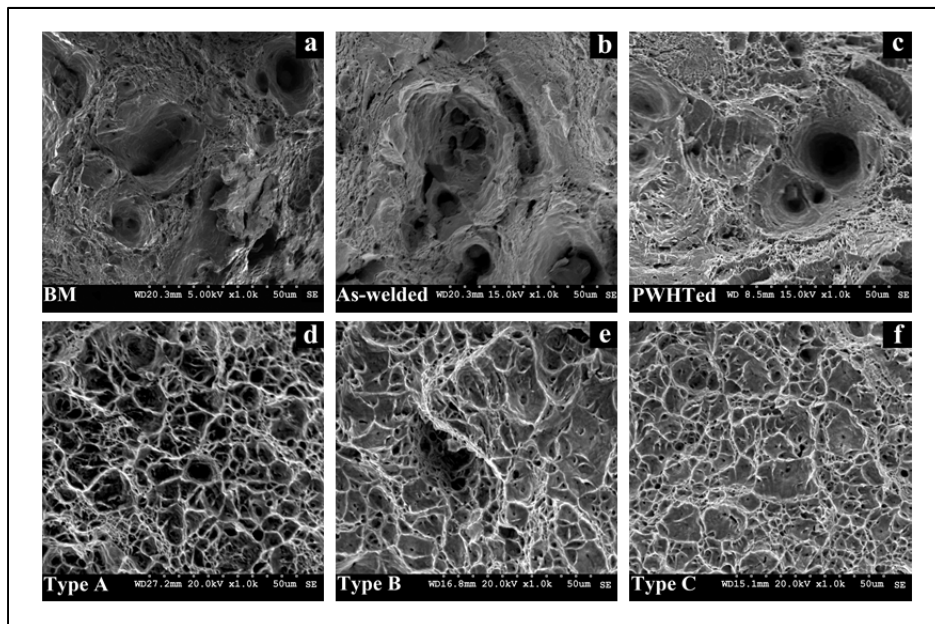
Figure 4-14 SEI of the tensile fracture surfaces for the: (a) BM, (b) As-welded, (c) PWHTed, (d) Type A, (e) Type B, and (f) Type C samples

These fractographic observations were complemented with examination of the microstructure near the failure location (Figure 4-15). In particular, for failure in the BM during tensile loading of the BM, As-welded and PWHTed samples (Figure 4-15a), the central zone of the fracture surface, where a hydrostatic stress state would dominate, voids, spherical in shape, were observed and their growth and coalescence into a macroscale crack propagating through the martensite matrix was evident. For Type A, B and C samples, where failure occurred in the FZ, the crack path through the martensitic matrix was seen to be influenced by the distribution of the secondary phases, such as delta ferrite, as indicated in Figure 4-15b. Specifically, decohesion between the delta ferrite/martensite interfaces was observed along with fracture of the delta ferrite particles. Hence tensile fracture in the UNS S41500 microstructure (BM or FZ) occurs through three possible mechanisms: (i) microvoid formation, growth and coalescence within the martensitic matrix, (ii) decohesion at the delta ferrite/martensite interfaces and (iii) fracture across the primary delta ferrite.
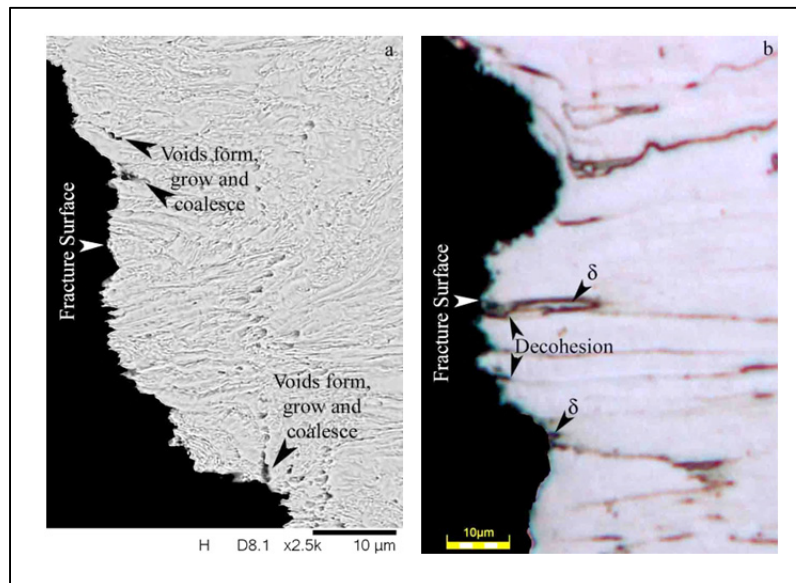
Figure 4-15 Typical images of the tensile fracture surfaces for: (a) BM, As-welded and PWHTed samples that failed in the BM and (b) Type A, B and C samples that failed in the FZ

4.4.3   Local tensile properties

The EB weldment was shown to comprise different microstructures and microhardness values and, as such, can be considered as "composite" structure with different zones, e.g. FZ, HAZs, and BM, which are expected to exhibit different mechanical properties locally. Using DIC, it is possible to extract the stress-strain curves in these different regions of the weldment by adjusting the gage length so that it spans the size of the region of interest. Once the stress–strain curve is plotted, it is possible to determine the yield stress and the localized plastic strain at fracture for a given location. These properties are termed "local" as they are derived from the mechanical response of the selected regions of interest.

Hence through DIC, the digital image of the specimen gage section immediately before rupture during tensile testing can be analyzed to understand the typical distributions of the major strains across the weldment just prior to failure, as illustrated in Figure 4-16 for the different welded samples (As-welded, PWHTed, Type A, Type B, and Type C). For each strain distribution, the adjacent scale indicates the strain magnitude. Hence, in these strain maps, the region experiencing localized deformation (strain concentration), indicated as the area with the highest intensity, corresponds to the location of the fracture that occurred immediately afterward. Using these strain maps, the inhomogeneous strain distributions (strain localization) within the tensile sample just prior to rupture can be examined methodically.
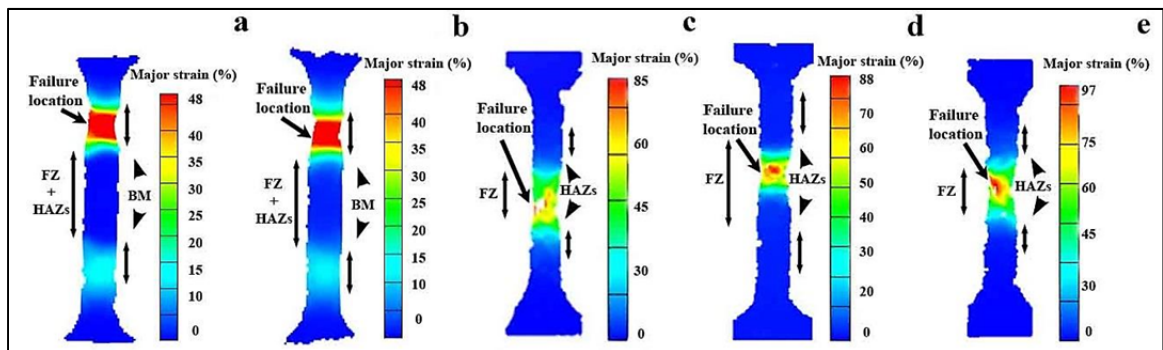
Figure 4-16 Major strain distribution map within the sample gage length as calculated by the Aramis® system just before failure for: (a) As-welded, (b) PWHTed, (c) Type A, (d) Type B, (e) Type C samples

Specifically, tensile loading of both the as-welded (Figure 4-16a) and PWHTed (Figure 4-16b) samples leads to considerable strain localization in the BM region but negligible (imperceptible) deformation in the FZ and HAZ. In particular, examining the major strain distributions along the median axis of the as-welded and PWHTed samples exemplifies clearly the inhomogeneity in the strain distribution between the BM, FZ and HAZ (Figure 4-17). Moreover, in the as-welded and PWHTed samples, the average global strain value was about 11% (Table 4-4), but the maximum local strain in the BM reached roughly 65%, while the FZ and most of the HAZ barely deformed (Figure 4-17b-c).
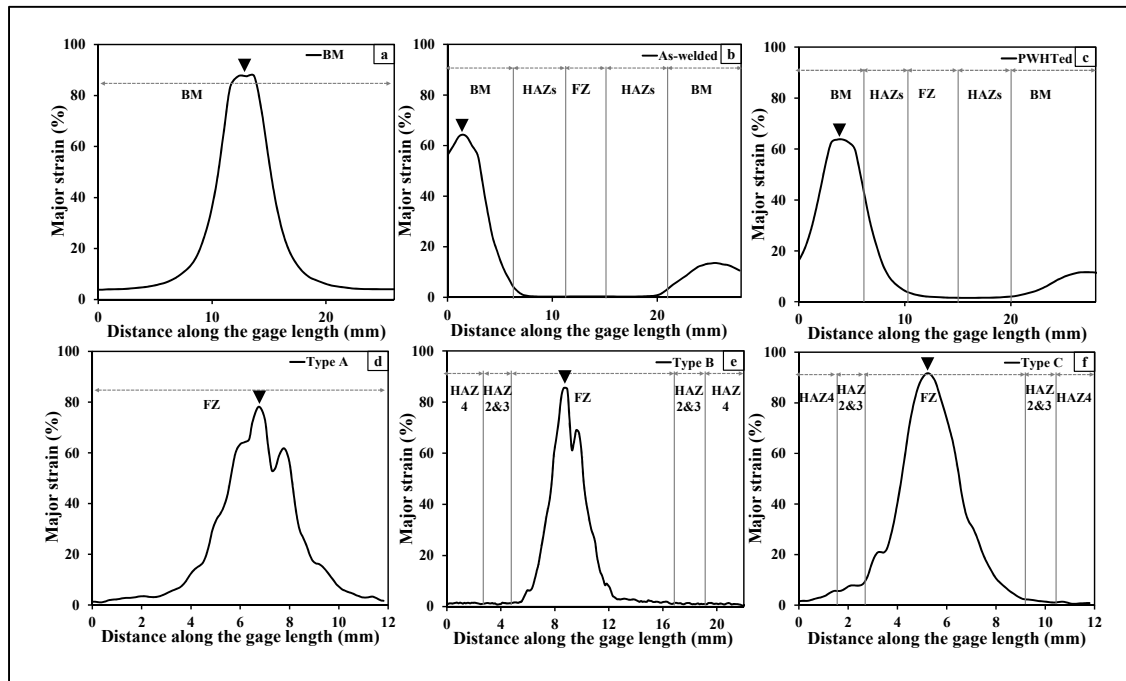
Figure 4-17 Distribution of the major strain along the median axis of the tensile sample gage length just prior to rupture: (a) BM, (b) As-welded, (c) PWHTed, (d) Type A, (e) Type B, and (f) Type C. The arrow demarcates the failure location.

It is noteworthy that the as-received UNS S41500 BM that had a global strain of 20.7% (Table 4-4) exhibited a local strain of 87.6% just prior to fracture (Figure 4-17a). Hence, with this situation of a large inhomogeneity in the strain distribution in the welded samples, discretization of the gage section (Nguyen-Duy, Tremblay et Lanteigne, 1988) in the area of the FZ and HAZ was ineffective for extracting the local properties. As such, Type A, B, and C tensile geometries were deliberated without the BM region in the gage length. In this way,

the FZ and HAZs deformed during tensile loading and failure triggered in these regions of interest, as illustrated in Figure 4-16c-e. For the Type A sample, which was comprised entirely of the FZ microstructure, the global strain was 21.9% (Table 4-4) but the strain locally was 78.2% in the FZ, as illustrated in Figure 4-17d. For the Type C sample that had a FZ/G ratio of 0.7, similar global (21.6%) and local (91%) strains are evident from Table 4-4and Figure 4-17e, respectively and fracture once again occurred in the FZ. Even in the Type B sample (FZ/G ratio of 0.4) where the global strain value of 11.8% was lower than that measured for the Type A and C samples, the local strain (85.1%) just before rupture in the FZ remained comparable (Figure 4-17d).

The local engineering stress-strain curves, extracted for the FZ and HAZ that were calculated using the Aramis® system, are shown in Figure 4-18, alongside the global mechanical response of the Type B and C samples. From the local mechanical response, the YS of the FZ, the high temperature HAZ (i.e. HAZ2 and 3) and HAZ4 were determined, as given in Table 4-5. In particular, for the FZ, the average value for the YS was calculated to be 869.2±30.2 MPa and the minimum %El. was ~20%. It is noteworthy that the YS and %El. data extracted from the local engineering stress-strain curves for the FZ from the Type B and C samples are in good agreement with the global values obtained through testing of the Type A sample geometry (100% FZ), which validates the accuracy of the analysis and results. For the microstructure in the combined region of HAZ2 and HAZ3, referred to as the high temperature HAZ, the average YS was 1076.0±57.2 MPa. For HAZ4, the average YS value was 941.5±9.2 MPa. Clearly, the FZ exhibits a lower YS than HAZ4 and the high temperature HAZ, which corroborates well with the microhardness findings (Table 4-3). However, as compared to the BM, the FZ properties appear to be superior – higher strength (YS and UTS), comparable ductility (%El. and local strain) and fractographic features of more uniform plasticity – that are promising for transitioning the EBW technology for industrial manufacture of thick gage section UNS S41500. Moreover, knowledge of the local mechanical response and properties for the different regions of the weldment arms engineers with a comprehensive understanding of the influence of the microstructure on the mechanical performance so that the design and manufacturing of the next generation of hydroelectric turbines can be achieved more efficiently, effectively, and sustainably.
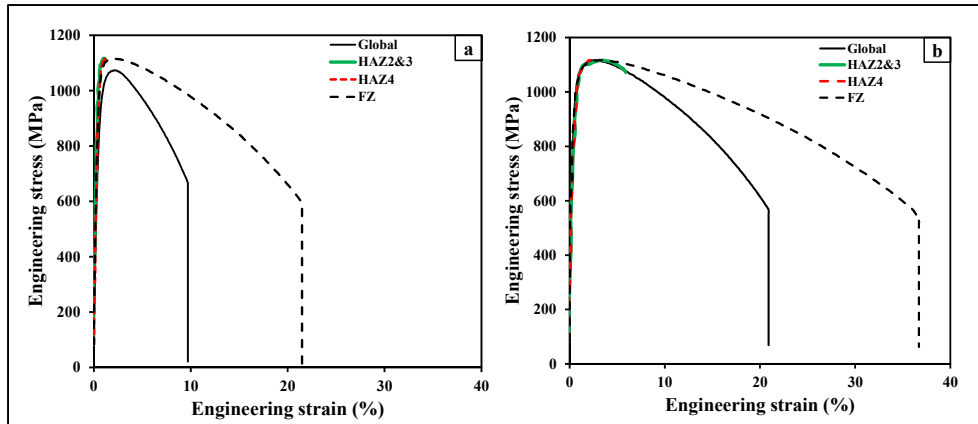
Figure 4-18 Local mechanical response of the FZ, high temperature HAZ (HAZ2 and HAZ3) and HAZ4 relative to the global stress–strain behavior measured using: (a) Type B and (b) Type C samples

Table 4-5 Local tensile properties in FZ and HAZ extracted from Type A, B, and C samples

Types	Regions	YS (MPa)	UTS (MPa)	%El. (%)
Type A	FZ	838.4	1094.1	20.5
Type B	FZ	870.5	1074.5	20.1
	HAZ2&3	1035.6	1074.5	N/A
	HAZ4	935.0	1074.5	N/A
Type C	FZ	898.7	1117.3	38.3
	HAZ2&3	1116.42	1117.3	N/A
	HAZ4	948.0	1117.3	N/A

4.5   Conclusions

Based on the results of the present research on electron beam welding of a 13%Cr–4%Ni martensitic stainless steel (UNS S41500), the following conclusions can be drawn:

• Without preheating of the 88 mm thick UNS S41500 martensitic stainless steel, an autogenous single pass EBW process was demonstrated to penetrate successfully a minimum of 72 mm without the occurrence of weld defects (e.g. porosity or cracking).

• The single pass autogenous electron beam welds revealed distinctive regions that included the UNS S41500 BM, FZ and a HAZ within which four different sub-regions were discernible. Comprehensive analysis of each region in the EB welds was undertaken by associating the microhardness evolution to the microstructural observations with an added deliberation of the sequential phase transformation possible during heating according to the ternary Fe–Cr–Ni equilibrium diagram.

• In general, for the as-welded condition, the hardness profiles revealed minimum (260 HV) and maximum (399 HV) values in the base metal and HAZ4, respectively. A progressive reduction in hardness was observed in the high temperature HAZs (HAZ2 and HAZ3) that was attributed to the formation of delta ferrite on heating.

• The application of a PWHT was observed to generate a relatively uniform microstructure and homogenize the hardness across the weldment. For instance after PWHT, the minimum and maximum hardness values in the weldment were 258 HV and 323 HV, respectively in the BM and the FZ. The reduction in the hardness in the BM was attributed to the stabilization of austenite during PWHT that resulted in a relatively high volume fraction of retained austenite (i.e. ~17 vol. %) in the microstructure. For the FZ with minimum and maximum values ranging between 338 HV and 394 HV in the as-welded condition, the hardness decreased after PWHT due to re-tempering of the martensite as well as the increased fraction (from 1% to 14%) of retained austenite.

• For both the as-welded and PWHTed conditions, the EB welds met the acceptance criteria stipulated for hydroelectric turbine applications in the ASME Section IX standard, namely a minimum requirement of 780 MPa for the ultimate tensile strength and failure location in the BM. Also, the tensile strength properties after PWHT were found to be slightly lower than in the as-welded condition, which was attributed to the reduction in the internal stresses and dislocation density due to tempering of the untempered martensite in the HAZ and FZ, as well as re-tempering of the BM.

• For the as-welded condition, evaluation of the local tensile properties and fractographic analysis indicated superior mechanical properties for the FZ microstructure relative to the tempered martensitic structure of BM.

4.6   Acknowledgments

The authors are grateful to Alstom Canada and Hydro Quebec for supporting this project and the financial contribution of the Consortium de recherche en fabrication et réparation des roues d'eau (CReFaRRE) and the Natural Sciences and Engineering Research Council of Canada (NSERC). The authors also would like to thank X. Pelletier, E. Poirier, M. Guerin and M. Banu of the National Research Council of Canada (NRC) for their technical assistance related to electron beam welding, metallographic preparation and tensile testing with digital image correlation, as well as E. Dallaire of IREQ for his assistance related to x-ray diffraction analysis. The authors are appreciative of the support from John Gavita of Olympus Canada to use the Olympus LEXT OLS4000, Olympus DSX500 and Hitachi TM3030 microscopes. The authors are also grateful for the useful advice and suggestions from L. Mathieu and M. Sabourin of Alstom and Dr. D. Thibault from IREQ.

4.7   References

ARAMIS « *User Handbook*». GOM. 2001. mbH, Braunschweig, Germany.

ASME Boiler and Pressure Vessel Code, Section IX. 2010. Section IX: « *Qualification standard for welding and brazing procedures, welders, brazers, and welding and brazing operators* ».

ASME Boiler and Pressure Vessel Code, Section VIII, Division 1. 2007. « *Rules for construction of pressure vessels* ».

ASTM-A240/A240M. 2004. « *Standard specification for chromium and chromium-nickel stainless steel plate, sheet, and strip for pressure vessels and for general applications* ». West Conshohocken, PA: American Society for Testing and Materials.

ASTM-A480/A480M. 2012. « *Standard specification for castings suitable for pressure service, corrosion resistant for general application* ». West Conshohocken, PA: American Society for Testing and Materials.

ASTM-E8/E8M-15a. 2013. « *ASTM designation E 8-00 Standard Test Methods for Tension Testing of Metallic Materials* ». West Conshohocken, PA: American Society for Testing Materials.

ASTM-E384-11E1. 2011. « *Standard test method for Knoop and Vickers hardness of materials* ». West Conshohocken, PA: American Society for Testing Materials.

Bakunov, AS; Muzhitskii, VF. 2004. « The control of the magnetisation of components prior to welding operations ». *Welding international*, vol. 18, n° 6, p. 498-500.

Bilmes, PD; Solari, M; Llorente, CL. 2001. « Characteristics and effects of austenite resulting from tempering of 13Cr–NiMo martensitic steel weld metals ». *Materials Characterization*, vol. 46, n° 4, p. 285-296.

Carrouge, D; Bhadeshia, HKDH; Woollin, P. 2004. « Effect of δ-ferrite on impact properties of supermartensitic stainless steel heat affected zones ». *Science and Technology of Welding & Joining*, vol. 9, n° 5, p. 377-389.

Côté, M. 2007. « *Étude des cinétiques de transformation de phase d'un acier inoxydable martensitique 13% Cr-4% Ni* ». École de technologie supérieure, Canada.

Enerhaug, J; Steinsmo, UM. 2001. « Factors affecting initiation of pitting corrosion in super martensitic stainless steel weldments ». *Science and Technology of Welding & Joining*, vol. 6, n° 5, p. 330-338.

Folkhard, E, Günther R. 1988. « *Welding metallurgy of stainless steels* ». Springer.

Gooch, TG. 1995. « Heat treatment of welded 13% Cr-4% Ni martensitic stainless steels for sour service ». *Welding Journal*, vol. 74, n° 7, p. 213s-223s.

Kumar, B, Ravi, S, Sharma, PM, Minz, RK. 2013. « Structure and microstructure evolution of a ternary Fe–Cr–Ni alloy akin to super martensitic stainless steel ». *Materials & Design*, vol. 50, p. 392-398.

Lippold, JC, Damian, JK. 2005. « *Welding metallurgy and weldability of stainless steels* ». ISBN 0-471-47379-0. Wiley-VCH.

Meleka, AH. 1971. « *Electron beam welding: principles and practice* ». McGraw-Hill, London.

Mirakhorli, F, Cao, X, Pham, XT, Wanjara, P, Fihey, JL. 2014. « Hybrid fiber laser-arc welding of 10-mm thick CA6NM stainless steel ». *Proceeding of Material Science and Technology,* p. 1891-1900, USA.

98

Nguyen-Duy, P, Tremblay V, Lanteigne, J. 1988. « Effects of hydrogen and tempering temperature on mechanical properties and fracture morphology of SAE 4135 Steel. (Retroactive Coverage) ». *Strength of Metals and Alloys. ICSMA 8*, vol. 3, p. 1287-1292.

Peters, WH, Ranson, WF. 1982. « Digital imaging techniques in experimental stress analysis ». *Optical engineering*, vol. 21, n° 3, p. 213427-213427.

Sanderson, A, Punshon CS, Russell, JD. 2000. « Advanced welding processes for fusion reactor fabrication ». *Fusion engineering and design*, vol. 49, p. 77-87.

Sarafan, S, Wanjara, P, Champliaud, H, Mathieu, L, Lanteigne, J. 2013. « Characteristics of electron beam welded CA6NM ». *Proceeding of Material Science and Technology*, p. 720-732, Canada.

Sarafan, S, Wanjara, P, Champliaud, H, Thibault, D. 2015. « Characteristics of an autogenous single pass electron beam weld in thick gage CA6NM steel ». *The International Journal of Advanced Manufacturing Technology*, vol. 78, n° 9-12, p. 1523-1535.

Song, YY, Li, XY, Rong, LJ, Li, YY. 2010a. « Anomalous phase transformation from martensite to austenite in Fe-13%Cr-4%Ni-Mo martensitic stainless steel ». *Journal of Materials Science & Technology*, vol. 26, n° 9, p. 823-826.

Song, YY, Li, XY, Rong, LJ, Ping, DH, Yin, FX, Li, YY. 2010b. « Formation of the reversed austenite during intercritical tempering in a Fe–13%Cr–4%Ni–Mo martensitic stainless steel ». *Materials Letters*, vol. 64, n° 13, p. 1411-1414.

Song, YY, Ping, DH, Yin, FX, Li, XY, Li, YY. 2010c. « Microstructural evolution and low temperature impact toughness of a Fe–13%Cr–4%Ni–Mo martensitic stainless steel ». *Materials Science and Engineering: A*, vol. 527, n° 3, p. 614-618.

Thibault, D; Bocher, P; Thomas, M. 2009. « Residual stress and microstructure in welds of 13%Cr–4%Ni martensitic stainless steel ». *Journal of Materials Processing Technology*, vol. 209, n° 4, p. 2195-2202.

Thibault, D; Bocher, P; Thomas, M; Lanteigne, J; Hovington, P; Robichaud, P. 2011. « Reformed austenite transformation during fatigue crack propagation of 13%Cr–4%Ni stainless steel ». *Materials Science and Engineering: A*, vol. 528, n° 21, p. 6519-6526.

Wang, P, Lu, SP, Xiao, NM, Li, DZ, Li, YY. 2010d. « Effect of delta ferrite on impact properties of low carbon 13Cr–4Ni martensitic stainless steel ». *Materials Science and Engineering: A*, vol. 527, n° 13, p. 3210-3216.

Wanjara, P, Dalgaard, E, Gholipour, J, Cao, X, Cuddy, J, Jonas, JJ. 2014. « Effect of pre-and post-weld heat treatments on linear friction welded Ti-5553 ». *Metallurgical and Materials Transactions A*, vol. 45, n° 11, p. 5138-5157.

Young, RA. 1993. « *Introduction to the Rietveld* method ». The Rietveld Method, vol. 5, p. 1-38.

Zou, D, Ying, H, Zhang, W, Fang, X. 2010. « Influence of tempering process on mechanical properties of 00Cr13Ni4Mo supermartensitic stainless steel ». *International Journal of Iron and Steel Research*, vol. 17, n° 8, p. 50-54.

CHAPITRE 5

EVALUATION OF DISTORTION AND RESIDUAL STRESSES IN ELECTRON BEAM WELDED HYDROELECTRIC TURBINE MATERIALS

S. Sarafan [a], J. B. Lévesque [b], P. Wanjara [c], J. Gholipour [c] and H. Champliaud [a]

[a] École de technologie supérieure, Montréal, Québec, Canada H3C 1K3
[b] Institut de recherche d'Hydro-Québec (IREQ), Varennes, Québec, Canada J3X 1S1
[c] National Research Council Canada, Aerospace, Montréal, Québec, Canada H3T 2B2

5.1   Abstract

Heavy-section assembly of hydroelectric turbine runner materials was demonstrated by EBW two important grades of steel − wrought UNS S41500 and cast CA6NM − using an autogenous single pass process to penetrate a 90-mm thick butt joint with and without preheating. The welding-induced distortions and residual stresses in the assemblies were characterized to understand the impact of the materials and process conditions (e.g. grade, welding, preheating and/or PWHT). Using a 3D optical measurement system the angular distortion after EBW of UNS S41500 and CA6NM steels was determined to be 0.13º and 0.38º, respectively. In the as-welded and PWHTed conditions, the longitudinal residual stresses, measured through the contour method, had a M-shaped distribution throughout the thickness due to tensile stresses (maximum of ~600 MPa) in HAZ4 and HAZ5 and compressive stresses (minimum of ~-500 MPa) in the FZ, HAZ2 and HAZ3. Application of PWHT reduced the maximum tensile and compressive stresses to ~100 MPa.

Keywords Residual stress, Distortion, Electron beam welding, Martensitic stainless steel, Contour method, 3D optical measurement system

NOMENCLATURE			
BM	Base metal	**FZ**	Fusion zone
DIC	Digital image correlation	**GMAW**	Gas metal arc welding
EB	Electron beam	**HAZ**	Heat-affected zone
EBW	Electron beam welding	M_f	Martensite finish temperature
EBZHT	Electron beam zonal heat treatment	M_s	Martensite start temperature
EDM	Electro-discharge machining	**PWHT**	Post-weld heat treatment
FCAW	Flux-cored arc welding	**2D**	2-dimensional
FE	Finite element	**3D**	3-dimensional

5.2   Introduction

As a high-energy density process, EBW has deep penetrating ability at low heat input compared to other conventional fusion welding technologies (Meleka, 1971), but, even so, the occurrence of distortion and residual stresses is inevitable due to non-uniform thermal strains induced by significant thermal gradients. Distortions and residual stresses in welds depend on the geometry, material properties, phase transformations, thermal history and external restraints (fixtures) applied during welding (Radaj, 1992). The welding-induced distortions result in dimensional inaccuracies that can be detrimental to product fit-up during assembly and the resulting tensile residual stresses promote brittle fracture, cracking and lowering of the fatigue/service life (Withers et Bhadeshia, 2001a; 2001b). Consequently, knowledge of the welding-induced distortions and residual stresses are of major interest to assess the weld integrity and performance, as well as to validate a suitable stress relief heat treatment.

Selection of a suitable destructive or non-destructive technique for residual stress measurement in heavy-section EB welds is challenging due to the presence of steep stress gradients. Amongst the different techniques, the contour method is especially attractive for obtaining a 2D map of the residual stresses through the thickness by performing an analysis of the topography on a cross-section obtained through an EDM cut (Prime, 2001; 2011; Thibault et al., 2010). This technique has been demonstrated for a variety of materials and

welding processes, of which the most relevant include measurements in 25 mm and 50 mm thick UNS S41500 joined by FCAW with 410NiMo filler metal (Thibault et al., 2010; Godin et al., 2013) and 50 mm thick Ti-6Al-4V EB welds (autogenous) in the as-welded and PWHTed conditions (Hosseinzadeh et al., 2013). The principle of the contour method is based on the release of residual stresses following the sectioning of a welded assembly. The relaxation of the residual stresses causes distortion in the newly cut plane. Using a FE model, the stress field needed to restore the distorted surface to a flat surface is calculated, which is equivalent to the original residual stresses (Prime and Dewald, 2013). Therefore, the contour method consists of three main stages: (1) using wire-EDM to cut a free surface in the weld cross-section containing residual stresses, (2) measuring the topography of the newly created surfaces and (3) filtering the displacement data and subsequently superimposing the surface contour in a FE model to create a 2D stress map (Prime and Dewald, 2013). A main concern in the contour method, however, is that the accuracy and resolution of the results is irrecoverably dependent on the quality of the wire-EDM cut.

The present work forms part of the output of a research consortium on investigating novel manufacturing technologies for next–generation hydroelectric turbines. As part of this consortium, the suitability of EBW for heavy-section assembly of two 13%Cr-4%Ni martensitic stainless steels, wrought UNS S41500 and cast CA6NM, was evaluated. Butt joints, 90-mm in thickness were assembled autogenously by EBW in a single pass with and without preheating. Of importance for the end-application was an understanding of the welding-induced distortions, which were evaluated using Argus®, an optical measurement system, and the longitudinal residual stresses in the as-welded and PWHTed assembly that were determined through the contour method.

5.3 Experimental procedure

5.3.1 Materials

Two material conditions (as given in Table 5-1) were selected in this study – ASTM A240 grade UNS S41500 and ASTM A743 grade CA6NM – in consideration of the design specifications for hydroelectric turbine manufacturing (alloy, thickness, heat treatment). It is

noteworthy that ASTM A240 and ASTM A743 recommend welding of both the as-rolled UNS S41500 and the as-cast CA6NM in the single- or double-temper heat treatment conditions.

Table 5-1 As-received materials conditions and chemical compositions used in this study

		ASTM A240 Grade UNS S41500		ASTM A743 Grade CA6NM	
As-received Condition		Hot rolled		Cast	
Thickness (mm)		90.0		90.0	
Heat Treatments Prior to Welding (Côté, 2007)	**Normalizing**	1000°C±20°C for 0.5 h followed by water-cooling to below the M_f of 90°C		1020°C±10°C for 6 h followed by air-cooling to below the M_f of 90°C	
	Tempering, Single/ Double	600°C±10°C for 4 h followed by air-cooling to room temperature		600°C±20°C for 8 h followed by air-cooling to below the M_f of 90°C	
				580°C±15°C for 8 h followed by air-cooling to room temperature	
Chemical Composition (wt-%)		C	0.018	C	0.013
		Si	0.34	Si	0.50
		Mn	0.66	Mn	0.58
		P	0.017	P	0.025
		S	0.0006	S	0.015
		Cr	12.80	Cr	11.74
		Mo	0.54	Mo	0.45
		Ni	4.10	Ni	3.64

5.3.2   Preparations for welding

The as-received UNS S41500 and CA6NM (in the normalized and tempered condition) were machined to obtain coupons with dimensions of 250 mm in length, 80 mm in width and 90-mm in thickness, as shown in Figure 5-1a. Prior to welding, the surfaces of the coupons were degreased with acetone, followed by fine grinding with a scouring pad and final cleaning with ethanol to remove any surface contamination. The two coupons were then tack welded to each other on either end and subsequently demagnetized using an enclosed demagnetizer (R.B. Annis 4.5" × 14") followed by a surface demagnetizer (Electro-Matic

model A13-1) to achieve a surface magnetic field reading between 0 and 1 gauss. The two coupons were then fixed to the worktable of the EBW system using a clamping fixture (Figure 5-1b). To maintain uniform clamping force conditions during assembly of each joint, the fasteners in the fixture were tightened using a torque meter so as to apply a fixed torque of 57.6 N·m.
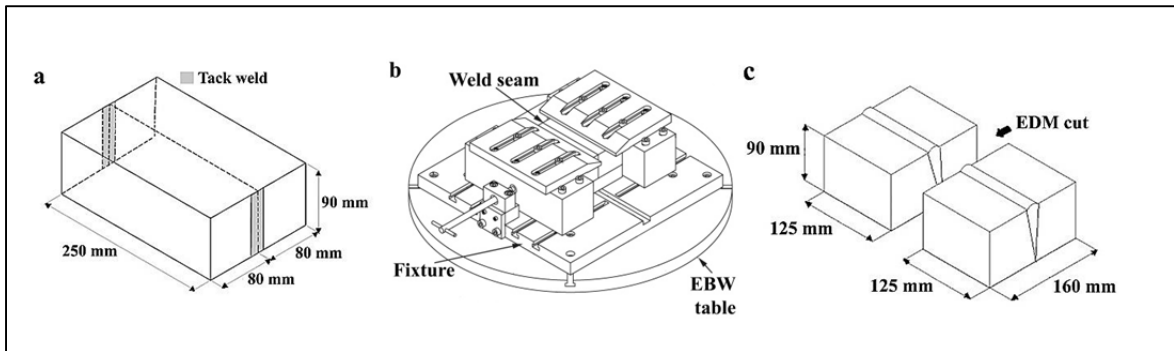
Figure 5-1 Schematics showing details related to assembly before welding and sectioning for residual stress measurement (a) the two coupons tack welded on each end, (b) the clamping fixture mounted to the worktable of the EBW system, and (c) Sectioning of the welded assembly by EDM along a transverse plane at the mid-length position

The recommended guidelines for welding 13%Cr-4%Ni include preheating, especially for heavy-sections, to temperatures of 100°C-170°C (Schoefer, 2004) so as to prevent defects such as cracking. The preheat temperature must be applied throughout the entire section thickness and must be monitored using thermocouples or a pyrometer. In the present work, preheating was carried out only for CA6NM, which exhibited susceptibility to vertical and horizontal cracking in the FZ during EBW (Sarafan et al., 2013; 2015). By contrast, EBW of UNS S41500 could be successfully undertaken (i.e. without cracking) on a heavy-section (72 mm) without preheating (Sarafan et al., 2015).

To preheat the CA6NM, an EBZHT (Chen et al., 2002) that involved oscillating a defocused beam in a circular path on the top surface of the weld seam along the longitudinal direction, was developed and validated by the authors previously (Sarafan et al., 2013; 2015). Multiple EBZHT passes were conducted to achieve the required temperature range

throughout the entire coupon. Upon reaching the required preheat temperature, the EBW program was initiated.

For both materials, EB welds were produced along the length of the coupons using a 42 kW Sciaky W2000 EBW system (60 kV/700 mA) operating with a pressure lower than 6.7×10^{-3} Pa. Specifically the EB was defocused by 10% and positioned at 63 mm below the top surface of the coupon. In total, eight EB welds were manufactured using different preheating and/or PWHT conditions, as summarised in Table 5-2. It is noteworthy that each condition was repeated in order to differentiate measurement errors in the residual stress results. After EBW, each weld was cooled to room temperature. Select welds designed for PWHT (J3, J4, J7 and J8) were tempered by heating at a rate of 50°C/h to 600±5°C, followed by holding for 12 h and then furnace-cooling; the experimental design of the PWHT conditions was performed according to the recommended guideline in ASTM A480 that stipulates cooling to a temperature of 95°C or below to ensure that the martensite phase completely transforms prior to re-tempering between 565°C to 620°C.

Table 5-2 Experimental design for the EB welds

Joint ID	Materials	Preheat (°C)	PWHT
J1*, J2*	CA6NM	100-170	N/A
J3, J4	CA6NM	100-170	600°C ±5°C, 12 h
J5*, J6*	UNS S41500	25	N/A
J7, J8	UNS S41500	25	600°C ±5°C, 12 h

5.3.3 Distortion measurement after welding

The out-of-plane distortion due to EBW was measured using Argus, a non-contact 3D optical measurement system, by electro-etching the outer surfaces of the tack welded assembly (prior to EBW) with a high contrast pattern of uniform black dots that were 1 mm in diameter and regularly spaced (centre to centre distance) 2 mm apart, as revealed by the 3D points and grid in the magnified view overlaid in Figure 5-2. Before and after EBW, the

applied dot pattern was photographed using a Nikon D300 digital camera from various directions – in a 360º rotating path – together with a set of scale bars and encoded measurement targets. Since the dot pattern deformed with the assembly during EBW, computation of the geometrical data for the 'distorted' dot pattern (i.e. the 3D coordinates) relative to the original grid, by means of photogrammetric algorithms in the software, then provided the local lateral displacements on the entire surface.
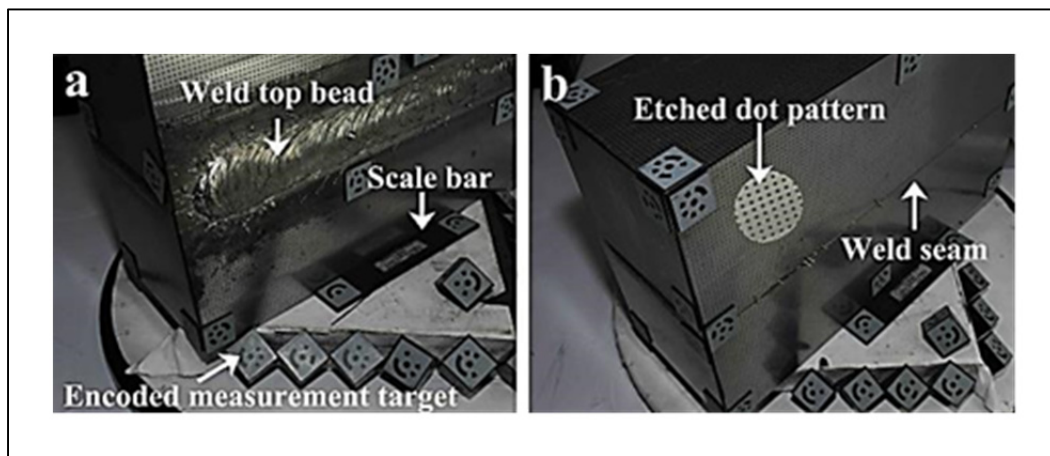
Figure 5-2 Argus set up showing the high contrast black dot pattern (grid) on the EB welded assembly with the scale bars and encoded measurement targets (a) top surface, and (b) bottom surface

5.3.4 Residual stress measurement by contour method

The 2D longitudinal residual stress maps in the as-welded (J1, J2, J5 and J6) and PWHTed (J3, J4, J7 and J8) welds were obtained through the contour method, which, as mentioned above, involves meticulous sectioning of the assembly into two halves, measuring the resulting displacement (due to residual stress redistribution) on the partitioned surfaces and computing the residual stresses through FE modelling and analysis. In this work, the welds were securely clamped to a Fanuc Robocut alpha-1iA wire EDM machine using fixtures placed immediately adjacent to the cutting path and then sectioned with a Tecfil Thermobrass 900 (63% copper and 37% zinc) wire having a diameter of 250 μm. To prevent flared edges at the entry and exit surfaces of the wire cutting path, the recommended practice by Hosseinzadeh et al. (Hosseinzadeh et al., 2013) was employed; the top and bottom

surfaces of each weld were fixed with 3 mm thick sacrificial plates placed along the wire cutting path. It is noteworthy that the sacrificial plate on the top surface of the weld was bent to the shape of the convex weld bead to ensure secure fixing. Each weld was then sectioned along a plane transverse to the weld seam at the mid-length position, as shown in Figure 5-1c. The surface topography was then measured with a non-contact profilometer using white light chromatic aberration with a sampling step size of 100 μm, as described in (Thibault et al., 2009), followed by Gaussian filtering of the data. Cubic splines with a 0.4 knot/mm grid density were used to depict the surfaces and averaged to remove any effects of the shear component of stress, as discussed by Prime (Prime, 2001). The resulting displacement data was then mapped on the FE mesh using eight-node hexahedral elements with a side length of 1 mm. A model with 205,000 elements and an aspect ratio of roughly one was sufficient to obtain a mesh-independent solution. The distributions of the residual stresses normal to the sectioned face were computed using an in-house elastic FE code that considered the bulk material behavior as isotropic and linear elastic with a Young's modulus of 200 GPa and a Poisson's ratio of 0.3.

5.4 Results and discussion

5.4.1 Distortion evolution in EB butt welds

For the 90-mm thick UNS S41500 and CA6NM, Figure 5-3 shows that the out-of-plane distortion distribution is V-shaped and symmetrical across the bottom surface after EB butt welding. For UNS S41500 (Figure 5-3a and c) and CA6NM (Figure 5-3b and c), maximum Z-displacements of 0.149 mm and 0.479 mm, respectively, were measured at the edges and minimum Z-displacements of -0.025 mm and -0.021 mm, respectively, were measured in the weld root area. Thus, the angular distortion in the as-welded UNS S41500 and CA6NM was 0.13º and 0.38º, respectively. These findings indicate that the application of EBW for heavy-section assembly of hydroelectric turbine materials has the advantage of low distortion that can be related to the low heat input of the single pass autogenous process as well as the low martensite transformation temperature of ~270°C (Côté, 2007) for UNS S41500 and CA6NM. Specifically, Ooi et al. (Ooi, Garnham et Ramjaun, 2014) reported that

ferrous grades with martensite transformation temperatures between 200°C and 300°C, such as low carbon 13%Cr-4%Ni martensitic stainless steels, had angular distortions below 0.5º, which corroborates the findings in the present work.
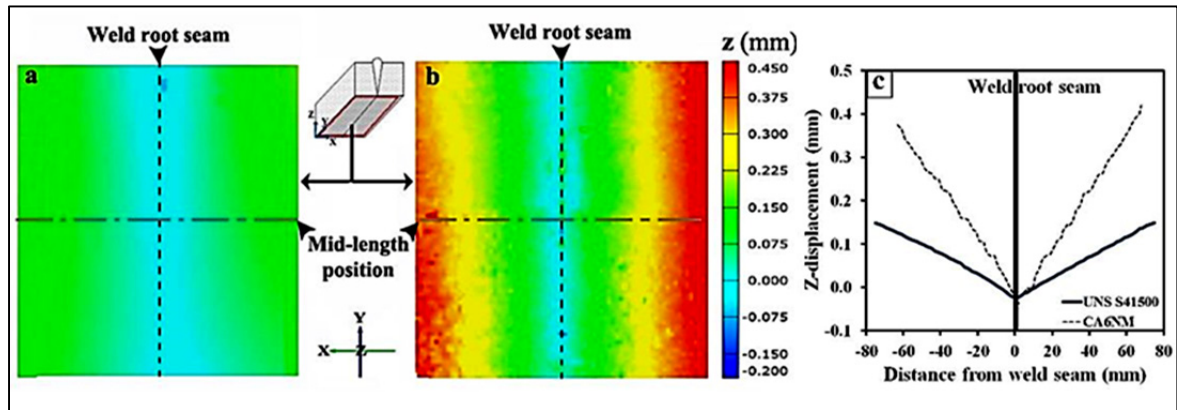
Figure 5-3 Out-of-plane displacements of the EB welds in the as-welded condition (a) map of UNS S41500, (b) map of CA6NM, and (c) profiles at the mid-length position

5.4.2 Longitudinal residual stress evolution in EB butt welds in the as-welded and PWHTed conditions

It is noteworthy that off-line characterization of the distortion distribution on the bottom surface of the EB butt welds using the Argus was facilitated by the vacuum atmosphere during welding that prevented discoloration of the grid. In addition, characterizing the distortion on the bottom (as opposed to the top) surface enabled measurements almost to the weld seam, due to the preservation of the etched pattern after welding. The present methodology provided a marked improvement in the quality and quantity of welding-induced distortion data collected, relative to the application of in-line digital image correlation with a speckle pattern on the top surface that was undertaken previously (Heinze, Schwenk et Rethmeier, 2011) to measure the distortion during GMAW of 5 mm thick plain carbon construction steel. Specifically, after welding, deterioration of the pattern in the FZ and HAZ resulted in burn-off or color changes to the grid and, thus, without experimental knowledge of the distortion distribution in the joint area, Heinze et al. (Heinze, Schwenk et Rethmeier, 2011) resorted to predicting the distortion through numerical

simulation. Thus, the present methodology for measuring the distortion distribution off-line can be useful for experimentally validating the numerical simulation typically utilized to predict distortion in welds.

Figure 5-4 shows the longitudinal residual stress distribution in the through-thickness (90-mm) of UNS S41500 and CA6NM in the as-welded and PWHTed conditions. In the as-welded condition, both materials exhibited similar M-shaped distributions with the presence of tensile and compressive residual stresses in the different regions of the weldment, i.e. FZ, HAZ2-HAZ5 and BM, which were identified based on previous work by the current authors (Sarafan et al., 2013; 2015a; 2015b) Specifically, maximum compressive stresses of ~-500 MPa were observed in the FZ and adjacent to the fusion boundary in HAZ2-HAZ3. At a further distance from the fusion boundary in HAZ4-HAZ5, the residual stresses transitioned rapidly to the maximum tensile values of ~600 MPa. For CA6NM, the peak tensile stress values were slightly lower (~100 MPa) than that measured for UNS S41500. This may be attributed to the preheating of the CA6NM before EBW, which would increase the time at peak temperatures during welding and lower the cooling rate. Thus, in the presence of lower thermal gradients, the CA6NM weldments would experience lower thermal and residual stresses relative to UNS S41500. Regardless, for both materials, these relatively high tensile residual stresses in HAZ4-HAZ5 are a risk for in-service cracking in the absence of PWHT.

The occurrence of compressive residual stresses in the FZ and HAZ2-HAZ3 of the EB welds can be related to the predominant role of the low transformation temperature of the martensite phase (Ms of 270°C and Mf of 90°C) in UNS S41500 and CA6NM (Côté, 2007) that allows the volumetric expansion originating from the austenite-to-martensite transformation to compensate for the accumulated thermal contraction strains (Eckerlid, Nilsson et Karlsson, 2003). Balancing tensile residual stresses were then apparent in HAZ4 of EB welded UNS S41500 and CA6NM. In HAZ5, heating of UNS S41500 and CA6NM during welding resulted in partial transformation of tempered martensite-to-austenite on heating; on cooling, the transformed austenite then reverted to untempered martensite with some austenite being retained (Sarafan et al., 2015a; 2015b). The presence of retained

austenite, in which compressive stresses are expected (Thibault et al., 2010), can decrease the tensile stress state in HAZ5 relative to HAZ4.

After PWHT, the longitudinal residual stresses in UNS S41500 and CA6NM (Figure 5-4c and d) were homogeneously distributed and considerably reduced (by more than 80%) compared to the as-welded condition, validating the effectiveness of the stress relief treatment. Specifically, for both materials, the maximum tensile and compressive residual stresses were ~±100 MPa in magnitude after PWHT and identified to occur in the HAZ and FZ, respectively. Previously, the current authors observed that, after PWHT, the EB welds in UNS S41500 and CA6NM exhibited a relatively homogeneous (tempered martensite) microstructure and hardness distribution across the weldment (Sarafan et al., 2015a; 2015b), which would explain the effective mitigation of the residual stresses. Feng (Feng, 2005) indicated that a decrease in the yield strength of the alloy at the PWHT temperature may also cause stress relief by the mechanism of creep relaxation. Thus, the mechanism of the stress relief after PWHT of the EB welds in UNS S41500 and CA6NM may be a combination of the creep relaxation (Feng, 2005) and low temperature phase transformation.
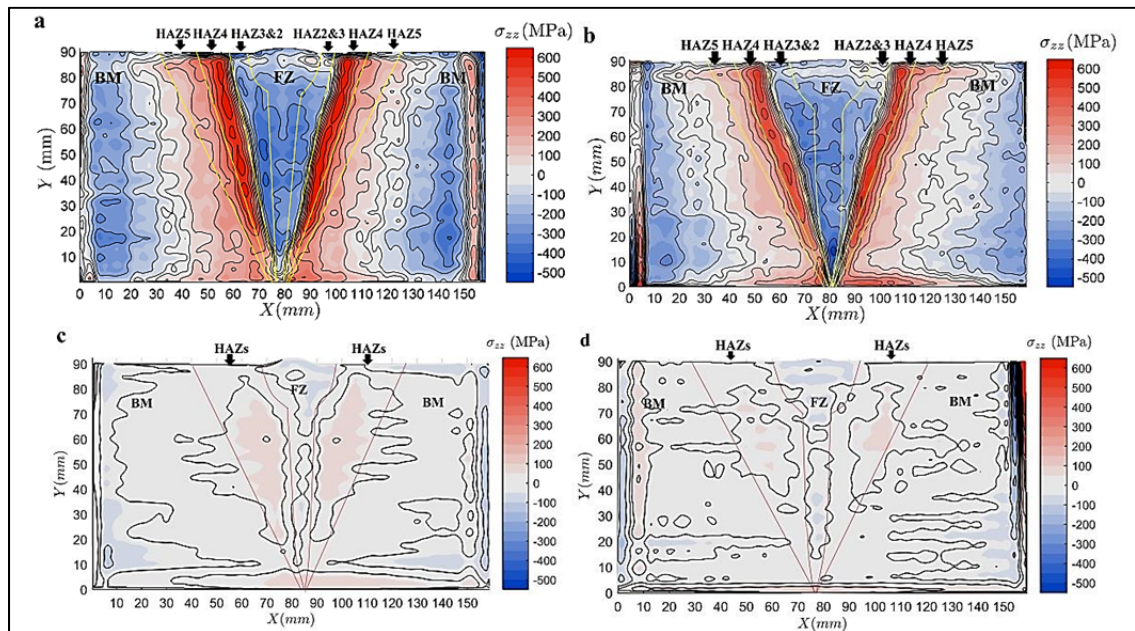

Figure 5-4 Longitudinal residual stress distributions in the EB welds (a) As-welded UNS S41500, (b) As-welded CA6NM, (c) PWHTed UNS S41500, and (d) PWHTed CA6NM

5.5   Conclusions

The following conclusions can be drawn on the distortions and longitudinal residual stresses in heavy-sections of UNS S41500 and CA6NM – two important martensitic stainless steel grades for hydroelectric turbine manufacturing – after autogenous EBW and PWHT:

• A methodology using an automated optical measurement system has been successfully demonstrated to measure welding-induced distortions. For 90-mm thick UNS S41500 and CA6NM, minimum z-displacement values of -0.025 mm and -0.021 mm, respectively, were measured at the weld root and maximum values of 0.149 mm and 0.479 mm, respectively, at the edges. The low angular distortion of 0.13º and 0.38º for UNS S415 and CA6NM, respectively, was attributed to the low transformation temperature of martensite in the two grades and the low heat input of the process.

• The longitudinal residual stresses, measured through the thickness of the UNS S41500 and CA6NM welds by the contour method, were compressive in the FZ and HAZ2-HAZ3 and tensile in HAZ4-HAZ5. The compressive stress state in the FZ and HAZ2-HAZ3 was related to the volumetric expansion resulting from the transformation of austenite to martensite that would compensate for the accumulated thermal contraction strains due to EBW. To counteract these compressive stresses (having peak values of ~-500 MPa), the adjacent zones, HAZ4-HAZ5, exhibited tensile residual stresses with maximum values of ~600 MPa, which present a relatively high risk of cracking for UNS S41500 and CA6NM in the absence of stress relieving after EBW.

• After PWHT, the magnitude of the longitudinal residual stresses was greatly reduced (~±100 MPa), but the HAZ and FZ remained in states of tension and compression, respectively. The low residual stresses and their homogeneous distribution observed in the present work suggest that similar materials, section thicknesses, welding and heat treatment practices could be used to good effect in hydroelectric turbine applications.

5.6   Acknowledgments

5.7   References

Chen, FR, Huo LX, Zhang YF, Zhang L, Liu FJ et Chen G. 2002. « Effects of electron beam local post-weld heat-treatment on the microstructure and properties of 30CrMnSiNi2A steel welded joints ». *Journal of materials processing technology,* vol. 129, n° 1, p. 412-417.

Côté, M. 2007. « *Étude des cinétiques de transformation de phase d'un acier inoxydable martensitique 13% Cr-4% Ni* ». École de technologie supérieure.

Eckerlid, J, Nilsson, T et Karlsson L. 2003. « Fatigue properties of longitudinal attachments welded using low transformation temperature filler ». *Science and Technology of Welding & Joining*, vol. 8, n° 5, p. 353-359.

Feng, Z. 2005. « *Processes and mechanisms of welding residual stress and distortion* ». Elsevier.

Godin, S, Boudreault, E, Lévesque, JB et Hazel B. 2013. « On-site post-weld heat treatment of welds made of 410NiMo steel ». *Materials Science and Technology (MS&T),* p. 754-765.

Heinze, C, Schwenk, C et Rethmeier, M. 2011. « Influences of mesh density and transformation behavior on the result quality of numerical calculation of welding induced distortion ». *Simulation Modelling Practice and Theory*, vol. 19, n° 9, p. 1847-1859.

Hosseinzadeh, F, Ledgard, P, Bouchard, PJ. 2013. « Controlling the cut in contour residual stress measurements of electron beam welded Ti-6Al-4VAlloy plates ». *Experimental Mechanics*, n° 53, p. 829–839.

Meleka, AH. 1971. « *Electron beam welding: principles and practice* ». McGraw-Hill, London.

Ooi, SW, Garnham, JE et Ramjaun, TI. 2014. « Review: low transformation temperature weld filler for tensile residual stress reduction ». *Materials & Design*, vol. 56, p. 773-781.

Prime, MB., DeWald, AT. 2013. « The contour method ». *Practical Residual Stress Measurement Methods*, p. 109-138, Wiley-Blackwell.

Prime, MB. 2001. « Cross-sectional mapping of residual stresses by measuring the surface contour after a cut ». *Journal of Engineering Materials and Technology*, vol. 123, n° 2, p. 162-168.

Prime, MB. 2011. « Contour method advanced applications: hoop stresses in cylinders and discontinuities ». *Engineering Applications of Residual Stress*, vol. 8. p. 13-28. Springer.

Radaj, D. 1992. *Heat effects of welding*. Springer-Verlag Berlin.

Sarafan, S., Wanjara, P., Champliaud, H., Mathieu, L., Lanteigne, J. 2013. « Characteristics of electron beam welded CA6NM ». *Proceeding of Material Science and Technology*, p. 720-732, Canada.

Sarafan, S., Wanjara, P., Champliaud, H., Thibault, D. 2015a. « Characteristics of an autogenous single pass electron beam weld in thick gage CA6NM steel ». *The International Journal of Advanced Manufacturing Technology*, vol. 78, n° 9-12, p. 1523-1535.

Sarafan, S., Wanjara, P., Champliaud, H., Gholipour, J. 2015b. « Global and local characteristics of an autogenous single pass electron beam weld in thick gage UNS S41500 Steel ». Submitted in *Materials Science and Engineering A*.

Schoefer, EA. 2004. « *Steel castings handbook supplement 7: welding of high alloy castings*». Steel Founders Society of America, USA.

Thibault, D., Bocher, P., Thomas, M. 2009. « Residual stress and microstructure in welds of 13%Cr–4%Ni martensitic stainless steel ». *Journal of Materials Processing Technology*, vol. 209, n° 4, p. 2195-2202.

Thibault, D., Bocher P., Thomas M., Gharghouri M.et Côté M.. 2010. « Residual stress characterization in low transformation temperature 13% Cr–4% Ni stainless steel weld by neutron diffraction and the contour method ». *Materials Science and Engineering: A,* vol. 527, n° 23, p. 6205-6210.

Withers, PJ, et Bhadeshia, HKDH. 2001b. « Residual stress. Part 1–measurement techniques ». *Materials science and Technology*, vol. 17, n° 4, p. 355-365.

Withers, PJ, et Bhadeshia, HKDH. 2001a. « Residual stress. part 2–nature and origins ». *Materials science and technology*, vol. 17, n° 4, p. 366-375.

CONCLUSIONS

The following conclusions for heavy-sections of UNS S41500 and CA6NM – two important martensitic stainless steel grades for hydroelectric turbine manufacturing – after autogenous electron beam welding by a single pass without fillet addition in both as-welded and post-weld heat treated conditions with and without preheating can be drawn:

• Autogenous EB welding can be successfully applied to penetrate up to 90 mm thick CA6NM and UNS S41500 by a single pass without filler addition. The single pass autogenous EB welds exhibited distinct regions that comprised the base metal (BM), fusion zone (FZ) and an elaborate heat affected zone (HAZ) within which four different sub-regions were distinguishable. Each region in the EB weldment could be interpreted by considering the microstructural observations in relation to the ternary Fe–Cr–Ni phase diagram and an illustrative examination of the local thermal history transpiring during EB welding.

• An electron beam zonal heat treatment (EBZHT) process can suitably preheat the CA6NM in-situ the EB welding system in range of 100-170°C to prevent cracking. The electron beam zonal heat treatment process involved oscillating a defocused beam in a circular path along the weld seam. Real-time acquisition of the thermal cycles during the EBZHT process indicated that after 3 sequential passes of the oscillated and defocused beam the preheat temperature range required for welding CA6NM could be reached. By contrast, an autogenous single pass EB welding of the 88 mm thick UNS S41500 martensitic stainless steel without preheating was demonstrated to penetrate without the occurrence of weld defects (e.g. porosity or cracking).

• The hardness profiles, for the as-welded condition, revealed maximum values in HAZ4 and a reduction in hardness in the high temperature HAZs (HAZ2 and HAZ3) that was attributed to the formation of delta ferrite on heating. Specifically, in HAZ3 the hardness decreased from near the HAZ4 to adjacent to HAZ2. EDX analysis of HAZ3 indicated that the delta ferrite formed on heating is retained due to the partitioning of ferrite-stabilizing elements, namely Cr and Mo, during transformation. Specifically the delta ferrite was enriched in Cr and Mo and depleted in Ni.

• The application of a post-weld heat treatment (PWHT) was observed to generate a relatively uniform microstructure with minimum and maximum hardness values in the base metal and the fusion zone, respectively. The reduction in the hardness in the base metal was attributed to the stabilization of austenite during PWHT that resulted in a relatively high volume fraction of retained austenite in the microstructure. The hardness in the fusion zone in the as-welded condition decreased after PWHT due to tempering of the re-transformed martensite as well as the higher (double) fraction of retained austenite.

• Evaluation of the local tensile properties and fractographic analysis in the as-welded condition indicated superior mechanical properties for the FZ microstructure –martensitic matrix with fine and uniformly distributed second phases (delta ferrite and retained austenite) – relative to the tempered martensitic structure of BM. For both the as-welded and PWHTed conditions, the EB welds met the tensile acceptance criteria stipulated for hydroelectric turbine applications in the ASME Section IX standard, namely a minimum requirement of 780 MPa for the ultimate tensile strength and failure location in the BM. Also, the tensile strength properties after PWHT were found to be slightly lower than in the as-welded condition, which was attributed to the reduction in the internal stresses and dislocation density due to tempering of the untempered martensite in the HAZ and FZ, as well as re-tempering of the BM.

• For the first time, as to the best knowledge of the author, a methodology using an automated optical measurement system was successfully demonstrated to measure the welding-induced distortions. For 90-mm thick UNS S41500 and CA6NM, minimum z-displacement values of -0.025 mm and -0.021 mm, respectively, were measured at the weld root and maximum values of 0.149 mm and 0.479 mm, respectively, at the edges. The low angular distortion of 0.13º and 0.38º for UNS S415 and CA6NM, respectively, was attributed to the low transformation temperature of martensite in the two grades and the low heat input of the process.

• The longitudinal residual stresses, measured through the thickness and across the transverse weld cross-section of the UNS S41500 and CA6NM welds by the contour method, were compressive in the FZ, HAZ2 and HAZ3 and tensile in HAZ4 and HAZ5. The compressive

stress state in the FZ, HAZ2 and HAZ3 was related to the volumetric expansion resulting from the transformation of austenite to martensite that would compensate for the accumulated thermal contraction strains due to EBW. To counteract these compressive stresses (having peak values of ~-500 MPa), the adjacent zones, HAZ4 and HAZ5, exhibited tensile residual stresses with maximum values of ~600 MPa, which present a relatively high risk of cracking for UNS S41500 and CA6NM without stress relieving after EBW.

• After PWHT, the magnitude of the longitudinal residual stresses was greatly reduced (~±100 MPa), but the HAZ and FZ remained in states of tension and compression, respectively. The low residual stresses distributed almost homogeneously in the EB welds of UNS S41500 and CA6NM after PWHT bode well for the assembly's service performance in hydroelectric turbine applications.

RECOMMENDATIONS AND FUTURE WORK

Some reported work existed on the arc welding of 13%Cr-4%Ni martensitic stainless steels, including the microstructural and microhardness evolution across the weldment, mechanical properties and residual stresses, which served as a point of reference for comparison of the present research findings. However with due consideration that many aspects of the present work represent the first reported results on an advanced welding process applied to assemble two important martensitic stainless grades for hydroelectric turbine manufacturing, the following suggestions have been formulated to continue the work to mature the technology further for industrialization.

• Although the current work adequately addressed the feasibility of applying a single pass electron beam welding to assemble heavy-sections in hydroelectric turbine materials, the joint design applied was a square-butt. The butt joint design has the advantage of minimizing/eliminating filler material addition and simplifying materials removal processes, but may pose some difficulties in regard to fit-up of the actual components. Future work on this welding process should involve the application of a single pass on a real joint design (e.g. T-joint) of the turbine runner to transition towards industrialization of this technology for hydroelectric turbine manufacturing.

• The influence of the electron beam welding on certain mechanical properties such as impact properties is pending. Specifically, the effect of electron beam welding zonal heat treatment on the impact energy of the weldment at low temperature should be assessed as well as the effect of the PWHT.

• The threshold value for the carbon content at which point preheating is needed during electron beam welding to prevent cracking is unknown. In particular, preheating in this work was only applied for CA6NM because it showed susceptibility to cracking without preheating, most probably due to the high carbon content of the alloy. By contrast, UNS S41500 could be electron beam welded without preheating. This implies the underlying role of the carbon, since the UNS S41500 had a lower carbon content than CA6NM. However, the microstructural state, i.e. wrought versus cast, may be another factor. For instance, in this

work it was apparent that the cast CA6NM base material had greater inhomogeneity and more defects (i.e. porosity) than UNS S41500. During EBW, the vacuum environment eliminates the impact of hydrogen and favors the possibility of eliminating the preheating requirement. However, at this point it is unclear if, for instance a lower carbon content in CA6NM can be electron beam welded without preheating. Also, there is probably a threshold value for the carbon content in both these materials, which will likely lead to cracking without preheating; the possibility of a threshold and its value need to be studied for electron beam welding.

• In this work, the distortions and residual stresses were measured by digital image correlation and the contour method, respectively. Additional methods such as finite element modeling and neutron diffraction, respectively, should be considered for comparison with the results.

• Certification of electron beam welded CA6NM and UNS S41500, according to the guidelines in ASME VIII and IX, also remains pending. Specifically, the transverse and longitudinal tensile properties as well as the bend properties in the through thickness direction of the joints in the as-welded and post-weld heat treated conditions need to be evaluated to understand the conformance of the assembly to the requirements for hydroelectric turbine manufacture. These evaluations will also provide statistical validation of the tensile mechanical property results reported in the present work.

STATEMENT OF ORIGINALITY AND CONTRIBUTION TO KNOWLEDGE

1. To prevent cracking in the CA6NM material during electron beam welding, an electron beam zonal heat treatment in-situ was successfully developed to enable preheating under a vacuum environment with a defocused beam.

2. A comprehensive examination of the microstructure and microhardness was performed for electron beam welds in heavy-sections (up to 90 mm) of 13%Cr-4%Ni low carbon martensitic stainless steels without filler addition using a single pass process. The electron beam welds exhibited 5 distinct regions that comprised fusion zone and four different sub-region heat affected zones.

3. By means of a digital image correlation system, the local tensile properties in FZ and HAZs of the EB welds were measured. The strain distribution and the region of strain localization in tensile samples before rupture were determined.

4. An automated optical measurement system was utilized to measure the out-of-plane displacements in the 90 mm thick electron beam welds and the angular distortion was determined to be relatively low due to the low transformation temperature of martensite in the CA6NM and UNS S41500 and the low heat input of the welding process.

5. The longitudinal residual stress maps in 90 mm thick EB welds of two important low carbon martensitic stainless steel grades were evaluated by the contour method.

LIST OF REFERENCES

Ackermann, F. 1984. « Digital image correlation: performance and potential application in photogrammetry ». *Photogrammetric record,* vol. 11, n° 64, p. 429-439.

Adams, MJ. 1968. « Low voltage electron beam welding effect of process parameters ». *British Welding Journal,* vol. 15, n° 3, p. 134-&.

Arata, Y; Tomie, M;Terai, K; Nagai, H et Hattori, T. 1973. « Shape decision of high energy density beam ». *Transactions of Joining and Welding Research Institute Osaka University,* vol. 2, n° 2, p. 130-146.

Arivazhagan, N, Singh, S, Prakash, S et Reddy, GM. 2011. « Investigation on AISI 304 austenitic stainless steel to AISI 4140 low alloy steel dissimilar joints by gas tungsten arc, electron beam and friction welding ». *Materials & Design,* vol. 32, n° 5, p. 3036-3050.

Atkins, M. 1980. « Atlas of continuous cooling transformation diagrams for engineering steels ». *American Society for Metals,* p. 260.

Barreda, JL, Santamarıa, F, Azpiroz, X, Irisarri, AM et Varona, JM. 2001. « Electron beam welded high thickness Ti6Al4V plates using filler metal of similar and different composition to the base plate ». *Vacuum,* vol. 62, n° 2, p. 143-150.

Bhadeshia, HKDH. 2004. « Developments in martensitic and bainitic steels: role of the shape deformation ». *Materials Science and Engineering: A,* vol. 378, n° 1, p. 34-39.

Bornert, M, Brémand, F, Doumalin, P, Dupré, JC, Fazzini, M, Grédiac, M, Hild, F, Mistou, S, Molimard, J et Orteu JJ. 2009. « Assessment of digital image correlation measurement errors: methodology and results ». *Experimental mechanics,* vol. 49, n° 3, p. 353-370.

Boudreault, E, Hazel, B, Côté, J et Godin, S. 2014. « In situ post-weld heat treatment on martensitic stainless steel turbine runners using a robotic induction heating process to control temperature distribution ». In *IOP Conference Series: Earth and Environmental Science.* vol. 22, p. 1-11.

Cam, G, Erim, S, Yeni, C et Kocak, M. 1999. « Determination of mechanical and fracture properties of laser beam welded steel joints ». *Welding Journal,* vol. 78, p. 193s-201s.

Carrouge, D; Bhadeshia, HKDH et Woollin, P. 2004. « Effect of δ-ferrite on impact properties of supermartensitic stainless steel heat affected zones ». *Science and Technology of Welding & Joining,* vol. 9, n° 5, p. 377-389.

126

Chen, FR, Huo, LX, Zhang, YF, Zhang, L, Liu, FJ et Chen, G. 2002. « Effects of electron beam local post-weld heat-treatment on the microstructure and properties of 30CrMnSiNi2A steel welded joints ». *Journal of materials processing technology,* vol. 129, n° 1, p. 412-417.

Chi, CT, et Chao, CG. 2007. « Characterization on electron beam welds and parameters for AZ31B-F extrusive plates ». *Journal of materials processing technology,* vol. 182, n° 1, p. 369-373.

Dalgaard, E, Wanjara, P, Gholipour, J, Cao, X et Jonas, JJ. 2012. « Linear friction welding of a near-β titanium alloy ». *Acta Materialia,* vol. 60, n° 2, p. 770-780.

Dugdale, RA. 1975. « Soft vacuum processing of materials with electron beams ». *Journal of materials science,* vol. 10, n° 5, p. 896-904.

Elmer, JW, Giedt, WH et Eagar, TW. 1990. « The transition from shallow to deep penetration during electron beam welding ». *Welding Journal,* vol. 69, n° 5, p. 167s-175s.

Enerhaug, J et Steinsmo, UM. 2001. « Factors affecting initiation of pitting corrosion in super martensitic stainless steel weldments ». *Science and Technology of Welding & Joining,* vol. 6, n° 5, p. 330-338.

Ferro, P, Zambon, A et Bonollo, F. 2005. « Investigation of electron beam welding in wrought Inconel 706—experimental and numerical analysis ». *Materials Science and Engineering: A,* vol. 392, n° 1, p. 94-105.

Folkhard, E et Rabensteiner, G. 1988. *Welding metallurgy of stainless steels*. Springer.

Giedt, WH, et Tallerico, LN. 1988. « Prediction of electron beam depth of penetration ». *Welding journal,* vol. 67, n° 12, p. 299-305.

Grytten, F, Daiyan, H, Polanco-Loria, M et Dumoulin, S. 2009. « Use of digital image correlation to measure large-strain tensile properties of ductile thermoplastics ». *Polymer Testing,* vol. 28, n° 6, p. 653-660.

Hablanian, MH. 1963. « A correlation of welding variables ». In *Proceeding of 5th Electron and Ion Beam Symposium*, edited by J. R. Morely, Alloyed electronis, Cambridge, p. 262-268.

Handbook. 2004. « *Steel Castings Handbook Supplement 8: High Alloys Data Sheets, Corrosion Series* ». USA: Steel Founders' Society of America.

Handbook, Metals. 1993. *Vol. 6: « Welding, Brazing and Soldering* ». ASM International, Materials Park, OH, p. 117-118.

Hemmer, H. 1999. « Prediction of penetration depths during electron beam welding ». *Science and Technology of Welding & Joining,* vol. 4, n° 4, p. 219-225.

Hild, F et Roux, S. 2006. « Digital image correlation: from displacement measurement to identification of elastic properties–a review ». *Strain,* vol. 42, n° 2, p. 69-80.

Ho, CY. 2005. « Fusion zone during focused electron beam welding ». *Journal of materials processing technology,* vol. 167, n° 2, p. 265-272.

Hu, MJ et Liu, JH. 2009. « Effects of zonal heat treatment on residual stresses and mechanical properties of electron beam welded TC4 alloy plates ». *Transactions of Nonferrous Metals Society of China,* vol. 19, n° 2, p. 324-329.

Hydro-Québec. 2011. « http://www.hydroquebec.com/innovation/fr/infolettre.html ».

Kabir, ASH, Cao, X, Gholipour, J, Wanjara, P, Cuddy, J, Birur, A et Medraj, M. 2012. « Effect of post-weld heat treatment on microstructure, hardness, and tensile properties of laser-welded Ti-6Al-4V ». *Metallurgical and Materials Transactions A,* vol. 43, n° 11, p. 4171-4184.

Kabir, ASH, Cao, X, Gholipour, J, Wanjara, P, Cuddy, J, Birur, A et Medraj, M. 2012. « Determination of global and local tensile behaviours of laser welded Ti-6Al-4V alloy ». In *Advanced Materials Research*. vol. 409, p. 859-864.

Kohyama, A, Arata, Y, Tomie, M et Igata, N. 1984. « Electron beam welding of titanium and Ti-6AL-4V thick plates ». *Journal of Nuclear Materials,* vol. 122, n° 1, p. 772-776.

Konkol, PJ. 1971. « Parameter study of electron-beam welding ». *Welding Journal American Welding Society*, vol. 50, n° 11, p. 765-776.

Kumar, A. 2011. « *IPCC special report on renewable energy sources and climate change mitigation »*. United Kingdom and New York, USA.

Lachmann, C, Nitschke-Pagel, T et Wohlfahrt, H. 1999. « Non-destructive characterization of fatigue processes in cyclically loaded welded joints by the Barkhausen noise method ». In *Proceedings of the International Workshop on Structural Health Monitoring, Stanford, CA*. p. 327-336.

Leclerc, H, Périé, JN, Roux, S et Hild, F. 2009. « Integrated digital image correlation for the identification of mechanical properties ». In *Computer Vision/Computer Graphics CollaborationTechniques*. p. 161-171. Springer-Verlag Berlin Heidelberg.

Lee, JY, Ko, SH, Farson, DF et Yoo, CD. 2002. « Mechanism of keyhole formation and stability in stationary laser welding ». *Journal of Physics D: Applied Physics,* vol. 35, n° 13, p. 1570-1576.

Leitão, C, Galvão, I, Leal, RM et Rodrigues, DM. 2012. « Determination of local constitutive properties of aluminium friction stir welds using digital image correlation ». *Materials & Design,* vol. 33, p. 69-74.

Lippold, JC, Kotecki, DJ. 2005. « Welding metallurgy and weldability of stainless steels ». ISBN 0-471-47379-0, Wiley-VCH.

Lockwood, WD, et Reynolds, AP. 2003. « Simulation of the global response of a friction stir weld using local constitutive behavior ». *Materials Science and Engineering: A,* vol. 339, n° 1, p. 35-42.

LY, PI, Smith, L, Gothekar, A et Chen, X. 2010. « Measure strain distribution using digital image correlation (DIC) for tensile tests ».

Macherauch, E, et Hauk, V. 1987. « *Residual stresses in science and technology* ». International Conference on Residual Stresses, Garnisch, Partenkirchen.

Meleka, AH. 1971. « *Electron beam welding: principles and practice* ». McGraw-Hill, London.

Metzbower, EA. 1993. « Keyhole formation ». *Metallurgical Transactions B,* vol. 24, n° 5, p. 875-880.

Mladenov, G, Vutova, K et Wojcicki, S. 1998. « Experimental investigation of the weld depth and thermal efficiency during electron beam welding ». *Vacuum,* vol. 51, n° 2, p. 231-233.

Moser, R, et Lightner JG. 2007. « using three-dimensional digital imaging correlation techniques to validate tire finite-element model ». *Experimental Techniques,* vol. 31, n° 4, p. 29-36.

Niederau, HJ. 1982. « A new low-carbon 16Cr-5Ni stainless martensitic cast steel ». In *Stainless Steel Castings: A Symposium Sponsored by ASTM Committee A-1 on Steel, Stainless Steel, and Related Alloys, Bal Harbour, Fla., 12-13 Nov. 1980*. Vol. 756, p. 382. ASTM International.

Ohta, A, Suzuki, N, Maeda, Y, Hiraoka, K et Nakamura, T. 1999. « Superior fatigue crack growth properties in newly developed weld metal ». *International Journal of Fatigue,* vol. 21, p. S113-S118.

Orteu, JJ, Bugarin, F, Harvent, J, Robert, L et Velay, V. 2011. « Multiple-camera instrumentation of a single point incremental forming process pilot for shape and 3D displacement measurements: methodology and results ». *Experimental mechanics,* vol. 51, n° 4, p. 625-639.

Pan, B, Qian, K, Xie, H et Asundi, A. 2009. « Two-dimensional digital image correlation for in-plane displacement and strain measurement: a review ». *Measurement science and technology,* vol. 20, n° 6, p. 1-18.

Peters, WH, et Ranson, WF. 1982. « Digital imaging techniques in experimental stress analysis ». *Optical engineering,* vol. 21, n° 3, p. 213427-213427.

Petrov, P, Georgiev, C et Petrov, G. 1998. « Experimental investigation of weld pool formation in electron beam welding ». *Vacuum,* vol. 51, n° 3, p. 339-343.

Pitrou, J. 1975. « Electron Beam Welding ». *Materials and Technology*, n° 11, p. 419-424.

Prime, MB, et DeWald, AT. 2013. « The contour method ». *Practical Residual Stress Measurement Methods*, p. 109-138.

Radtke, EW. 1964. « *Means for electron beam welding without a vacuum chamber* ». US Patent 3,136,882.

Reynolds, AP, et Duvall, F. 1999. « Digital image correlation for determination of weld and base metal constitutive behavior ». *Welding Journal,* vol. 78, p. 355-s.

Saeed, RA, Galybin, AN et Popov, V. 2010. « Modelling of flow-induced stresses in a Francis turbine runner ». *Advances in Engineering Software,* vol. 41, n° 12, p. 1245-1255.

Sarafan, S, Wanjara, P, Champliaud, H, Mathieu, L, Lanteigne, J. 2013. « Characteristics of electron beam welded CA6NM ». *Proceeding of Material Science and Technology*, p. 720-732, Canada.

Sarafan, S, Wanjara, P, Champliaud, H et Thibault, D. 2015. « Characteristics of an autogenous single pass electron beam weld in thick gage CA6NM steel ». *The International Journal of Advanced Manufacturing Technology,* vol. 78, n° 9-12, p. 1523-1535.

Saresh, N, Pillai, GM et Mathew, J. 2007. « Investigations into the effects of electron beam welding on thick Ti–6Al–4V titanium alloy ». *Journal of Materials Processing Technology,* vol. 192, p. 83-88.

Schultz, H. 1993. « *Electron Beam Welding* ». Woodhead Publishing.

Shiga, C, Yasuda, HY, Hiraoka, K et Suzuki, EH. 2010. « Effect of M_s temperature on residual stress in welded joints of high-strength steels ». *Welding in the World,* vol. 54, n° 3-4, p. R71-R79.

Simoneau, R, Thibault, D et Fihey, JL. 2009. « A comparison of residual stress in hammer-peened, multi-pass steel welds–A514 (S690Q) and S41500 ». *Welding in the World,* vol. 53, n° 5-6, p. R124-R134.

Srinivasan, PB, Sharkawy, SW et Dietzel, W. 2004. « Hydrogen assisted stress-cracking behaviour of electron beam welded supermartensitic stainless steel weldments ». *Materials Science and Engineering: A,* vol. 385, n° 1, p. 6-12.

Su, SF, Lin, HK, Huang, JC et Ho, NJ. 2002. « Electron-beam welding behavior in Mg-Al-based alloys ». *Metallurgical and Materials Transactions A,* vol. 33, n° 5, p. 1461-1473.

Sun, Z et Karppi, R. 1996. « The application of electron beam welding for the joining of dissimilar metals: an overview ». *Journal of Materials Processing Technology,* vol. 59, n° 3, p. 257-267.

Tang, Z, Liang, J., Xiao, Z et Guo, C. 2012. « Large deformation measurement scheme for 3D digital image correlation method ». *Optics and Lasers in Engineering,* vol. 50, n° 2, p. 122-130.

Thibault, D, Bocher, P, Thomas, M, Gharghouri, M et Côté, M. 2010. « Residual stress characterization in low transformation temperature 13%Cr–4%Ni stainless steel weld by neutron diffraction and the contour method ». *Materials Science and Engineering: A,* vol. 527, n° 23, p. 6205-6210.

Thibault, D; Bocher, P et Thomas, M. 2009. « Residual stress and microstructure in welds of 13%Cr–4%Ni martensitic stainless steel ». *Journal of Materials Processing Technology,* vol. 209, n° 4, p. 2195-2202.

Totten, G. 2005. « Handbook on residual stress, vol. 1 ». *SEM, Bethel, ISBN*, p. 978-0871707291.

Wanjara, P et Jahazi, M. 2008. « Characterization of electron beam welded 17-4PH stainless steel ». *Canadian Metallurgical Quarterly,* vol. 47, n° 4, p. 413-435.

Wanjara, P, Dalgaard, E, Gholipour, J, Cao, X, Cuddy, J et Jonas, JJ. 2014. « Effect of pre- and post-weld heat treatments on linear friction welded Ti-5553 ». *Metallurgical and Materials Transactions A,* vol. 45, n° 11, p. 5138-5157.

Wu, SH, Huang, JC et Wang, YN. 2004. « Evolution of microstructure and texture in Mg-Al-Zn alloys during electron-beam and gas tungsten arc welding ». *Metallurgical and Materials Transactions A,* vol. 35, n⁰ 8, p. 2455-2469.